

**STRUCTURE-FUNCTION OF MEMBRANE PROTEIN COMPLEXES  
INVOLVED IN OXYGENIC PHOTOSYNTHESIS**

by

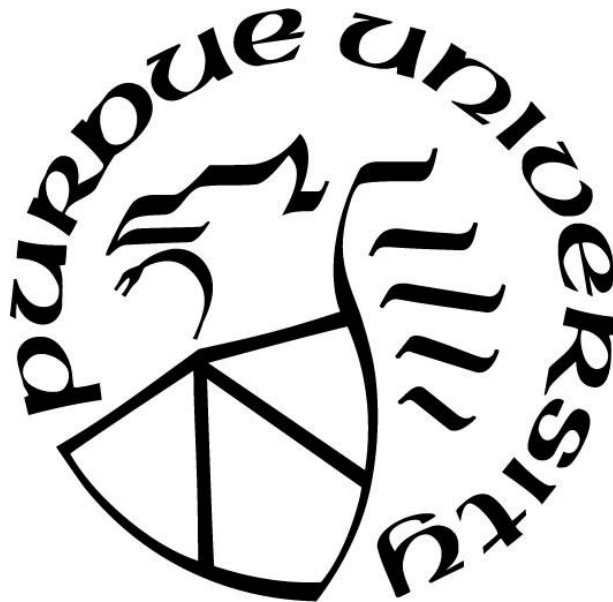
**Satarupa Bhaduri**

**A Dissertation**

*Submitted to the Faculty of Purdue University*

*In Partial Fulfillment of the Requirements for the degree of*

**Doctor of Philosophy**



Department of Biological Sciences

West Lafayette, Indiana

August 2019

**THE PURDUE UNIVERSITY GRADUATE SCHOOL**  
**STATEMENT OF COMMITTEE APPROVAL**

Dr. William A. Cramer, Chair

Department of Biological Sciences

Dr. Nicholas Noinaj

Department of Biological Sciences

Dr. Carol B. Post

Department of Medicinal Chemistry and Molecular Pharmacology

Dr. Sergei Savikhin

Department of Physics and Astronomy

**Approved by:**

Dr. Janice P. Evans

Head of the Graduate Program

**To Ma, Baba, Dada, Ishita Di and Adrish**

## ACKNOWLEDGMENTS

Firstly, I would like to thank my advisor, Prof. William A. Cramer, who supported me and helped me in every way to reach the finish line. The training I received in this lab will be my asset for my life, undoubtedly. My PhD journey wouldn't have been possible without my lab mates, former and present, who went on to become my friends. I will always remember the times spent in the lab with Stas, Sejuti, Sandeep, Tanya, Katherine and Jillian. All of them made my long hours in the lab so much fun even when my experiments refused to be my friends. I was very fortunate to have Nick, Carol and Sergei in my committee, who made every annual meeting so much productive and gave me a direction every time. My social circle had a huge presence in my PhD life. My friends Somrita, KK, Amartya, Sreyansh, Arindam, Indrani, Sayantan and DM have given me times which I will cherish all my life. They made life so much easier when everything refused to go in the right way. I would like to thank everyone who believed in me and everyone who did not, which kept me going. My last one year became filled with so much love and support from Bob, who kept on pushing me to get some work done, even when at times it seemed impossible to get up. He helped me so much in the final days leading to the defense, for which I will always be grateful. And lastly, my family who never gave up on me. Their love and faith in my abilities, their blessings and well-wishes are instrumental in my completion of this long journey. Finally, I would like to end by giving a pat on my back, and just say, "I did it! I am proud of myself"!!

## TABLE OF CONTENTS

LIST OF TABLES .....	9
LIST OF FIGURES .....	11
LIST OF SYMBOLS, ABBREVIATIONS AND NOMENCLATURE .....	15
ABSTRACT.....	17
CHAPTER 1. INTRODUCTION .....	19
1.1 Photosynthetic Electron Transfer Chain .....	19
1.2 Cytochrome <i>bc</i> Complexes .....	21
1.3 Cytochrome <i>b<sub>6</sub>f</i> complex: .....	21
1.3.1 Structural Similarities .....	23
1.3.2 Functional Similarities.....	24
1.4 Interactions of Lipids with Membrane Proteins.....	26
1.4.1 Effects of Internal Lipids on Cytochrome <i>bc</i> Complexes .....	26
1.5 Formation of Supercomplexes in Photosynthetic Electron Transport Chain.....	27
1.6 Photosystem I Reaction Center Complex .....	28
1.7 ATP-synthase .....	29
CHAPTER 2. STRUCTURE-FUNCTION OF THE CYTOCHROME <i>b<sub>6</sub>f</i> COMPLEX; LIPID DEPENDENCE. ....	31
2.1 Summary .....	31
2.2 Introduction.....	31
2.3 Materials and Methods.....	34
2.3.1 Purification of cytochrome <i>b<sub>6</sub>f</i> complex from spinach.....	34
2.3.2 Differential Scanning Calorimetry (DSC). ....	34
2.3.3 Circular Dichroism (CD). ....	34
2.3.4 Secondary structure calculation. ....	34
2.3.5 Thermal denaturation and Native-PAGE.....	35
2.3.6 Encapsulation of cytochrome <i>b<sub>6</sub>f</i> complex into nanodiscs. ....	35
2.3.7 Generation of synthetic antibodies (sAbs/Fabs) against the cytochrome <i>b<sub>6</sub>f</i> complex in nanodiscs by competitive and subtractive phage display selection (In collaboration with S. Erramilli, T. Kossiakkoff, University of Chicago). ....	35

2.3.8	Validation by Single-Point ELISA (enzyme-linked immunosorbent assay).....	37
2.3.9	Encapsulation of cytochrome <i>b<sub>6</sub>f</i> complex into bicelles.....	37
2.3.10	Removal of phospholipids by phospholipase <i>A<sub>2</sub></i> .....	37
2.3.11	Electron transfer activity assay. ....	38
2.3.12	Superoxide production: .....	38
2.4	Results.....	38
2.4.1	Differential scanning calorimetry (DSC): .....	38
2.4.2	Thermal denaturation / far-UV circular dichroism.....	41
2.4.3	Thermal denaturation/native PAGE .....	46
2.4.4	Electron transfer activity.....	47
2.4.5	Superoxide Production.....	48
2.5	Discussion.....	49
CHAPTER 3. PATHWAYS OF TRANSMEMBRANE ELECTRON TRANSFER IN CYTOCHROME <i>bc</i> COMPLEXES: DIELECTRIC HETEROGENEITY AND INTER-HEME COULOMBIC INTERACTIONS .....		
		56
3.1	Summary.....	56
3.2	Introduction.....	56
3.3	Materials and Methods.....	58
3.3.1	Isolation/Purification of Cytochrome <i>bc<sub>1</sub></i> Complex .....	58
3.3.2	Absorbance Difference Spectra .....	59
3.3.3	Electron Transport Activity .....	59
3.3.4	Simultaneous Measurement of Absorbance and Circular Dichroism Spectra of Hemes <i>b<sub>n</sub></i> and <i>b<sub>p</sub></i> .....	59
3.3.5	Simulation of CD Spectra: Interaction Between Different Heme Pairs .....	59
3.3.6	Simulation of kinetics of absorbance and circular dichroism changes resulting from addition of reductant (By Prof. Sergei Savikhin, Department of Physics and Astronomy, Purdue University).....	60
3.3.7	Model for Kinetics of Reductant-Induced Amplitude Changes of Exciton Circular Dichroism and Absorbance.....	61
3.4	Results.....	62
3.4.1	Characterization of Purified Cytochrome <i>bc<sub>1</sub></i> Complex: Heme Difference Spectra .	62

3.4.2	Chemical Reduction of Hemes in the bc <sub>1</sub> Complex .....	62
3.4.3	Simultaneous Measurement of Circular Dichroism and Heme Absorbance .....	65
3.4.4	Identity of the Interacting Heme Pair (s) Responsible for the Excitonic Interaction .....	66
3.5	Discussion .....	68
3.5.1	Origin of Split Excitonic Circular Dichroism Spectra in Dimeric Heme Complex ..	68
3.5.2	Comparison of Heme b Reduction in Cytochrome b <sub>6</sub> f and bc <sub>1</sub> Complexes: Inter-Heme Dielectric Constants.....	70
3.5.3	Calculation of Dielectric Heterogeneity for the cytochrome bc <sub>1</sub> .....	71
3.5.4	Summary of formulae that describe the energy of the different reduced states in the cytochrome bc <sub>1</sub> complex.....	71
3.5.5	n-side and inter-heme ε values.....	72
3.5.6	Structure Differences between b <sub>6</sub> f and bc <sub>1</sub> Complexes: Inter-Heme Orientation .....	73
3.6	Conclusion .....	75
CHAPTER 4. ISOLATION AND CHARACTERIZATION OF NOVEL PHOTOSYSTEM I-ATP SYNTHASE SUPERCOMPLEX FROM SPINACH .....		76
4.1	Summary .....	76
4.2	Introduction.....	76
4.3	Materials and Methods.....	78
4.3.1	Purification of Super-Complex.....	78
4.3.2	Electrophoretic Analysis.....	79
4.3.3	Western Blotting .....	79
4.3.4	Mass Spectroscopy (Done in the laboratory of Prof. Julian P. Whitelegge, UCLA) .....	79
4.3.5	Assay of ATPase Activity. ....	80
4.3.6	Negative Stain Electron Microscopy. ....	80
4.3.7	Fluorescence Spectroscopy.....	80
4.4	Results.....	81
4.4.1	A unique super-complex from thylakoid membranes that functions in oxygenic photosynthesis; electrophoretic and immuno-blot analysis. ....	81
4.4.2	Mass Spectrometry. ....	82
4.4.3	Presence of FNR in Super-Complex.....	83
4.4.4	ATPase Activity.....	84

4.4.5 Negative Stain Microscopy of the Super-Complex .....	85
4.5 Discussion .....	86
4.6 Conclusion .....	87
REFERENCES .....	88
VITA.....	103
PUBLICATIONS.....	104

## LIST OF TABLES

Table 1.1: Subunits and their corresponding molecular weights of the cytochrome <i>b<sub>6</sub>f</i> complex ( <i>Spinacea sp.</i> ).....	23
Table 2.1: List of subunits and their molecular weights; and prosthetic groups, present in the cytochrome <i>b<sub>6</sub>f</i> complex, purified from <i>Spinacea</i> (62).....	32
Table 2.2.: Comparison of the enthalpy and melting temperature ( $T_m$ ) of the delipidated cytochrome <i>b<sub>6</sub>f</i> complex and in the presence of DOPG, DOPC, and SQDG. ....	39
Table 2.3: Comparison of the $T_m$ of the three transitions (1, 2 and 3) obtained from deconvolution of the DSC thermograms for the cytochrome <i>b<sub>6</sub>f</i> complex in the presence of DOPG, DOPC, and SQDG. Note: the enthalpies of the individual transitions add up to the final $\Delta H$ values (Table 2.2). .....	41
Table 2.4: Secondary structure content of the <i>b<sub>6</sub>f</i> complex from <i>Nostoc sp.</i> (PDB 4OGQ).....	41
Table 2.5: Comparison of the melting temperatures ( $T_m$ ) of the cytochrome <i>b<sub>6</sub>f</i> complex solubilized in UDM, in the absence and presence of DOPG, DOPC, and SQDG, as measured by far-UV circular dichroism at 222 nm. Standard deviation determined from 3 trials. ....	43
Table 2.6: Comparison of the melting temperatures ( $T_m$ ) of the delipidated cytochrome <i>b<sub>6</sub>f</i> complex before and after addition of phospholipase A <sub>2</sub> , measured by far-UV CD. Standard deviation determined from 3 trials. ....	43
Table 2.7: Comparison of the melting temperatures ( $T_m$ ) of the cytochrome <i>b<sub>6</sub>f</i> complex in UDM and in the presence of nanodiscs and bicelles, measured by far UV-CD. Standard deviation determined from 3 trials. ....	44
Table 2.8: Amino acid sequences of Fab/sAb heavy chain (HC) and light chains (LC) of binders selected based on their highest binding strength with the cytochrome <i>b<sub>6</sub>f</i> complex in nanodiscs, obtained by ELISA. ....	46
Table 2.9: Amount of H <sub>2</sub> O <sub>2</sub> produced by the cytochrome <i>b<sub>6</sub>f</i> complex (explained in <i>Methods</i> ), in the presence and absence of lipids. * $p < 0.05$ (defined in <i>Methods</i> ) .....	49
Table 3.1: Geometric Relations of Hemes in the <i>Rb. capsulatus bc<sub>1</sub></i> Complex: (A) Heme center-center (Fe-Fe) distances; (B) interplanar angles between the four <i>b</i> -type hemes in <i>Rb. capsulatus</i> dimeric cytochrome <i>bc<sub>1</sub></i> complex (PDB 1ZRT); For comparison, inter interheme geometric parameters of the cytochrome <i>b<sub>6</sub>f</i> complex (PDB 4OGQ) are shown in parentheses; (C) individual pair-wise contributions (in percent) to excitonic CD spectrum determined from the crystal structure relative to fully reduced CD amplitudes (100%), assuming contributions from all components in a fully reduced complex.....	67
Table 3.2: Threshold Inter-Heme Dielectric Constants ( $\epsilon_{np}$ ) in Cytochrome <i>bc<sub>1</sub></i> Complex (assuming $\epsilon_{n1, n2} = 2.0$ ). ....	72

Table 4.1: Relative abundance (Mascot Search Algorithm) of polypeptide components identified in the trypsin in-gel digest of the ATPase-PSI-FNR super-complex spinach thylakoids of approximately 1 MDa as shown on clear native PAGE (**Figure 4.2 B**)..... 82

## LIST OF FIGURES

Figure 1.1: The electron transport chain in chloroplasts [3].....	19
Figure 1.2: Cytochrome <i>bc</i> complexes involved in oxygenic photosynthesis: (A) Cytochrome <i>b<sub>6</sub>f</i> complex from the cyanobacterium <i>Nostoc</i> sp. (PDB 4OGQ) and (B) Cytochrome <i>bc<sub>1</sub></i> complex from the photosynthetic bacterium <i>Rhodobacter spheroides</i> (PDB 2QJP). Both complexes catalyze quinone reduction on the electropositive p-side or luminal side of the membrane, and quinone oxidation on the electronegative n-side or stromal side. The electron transport is coupled with pumping of protons from the n to p-side which generates an electrochemical potential across the membrane [19, 20].....	21
Figure 1.3: Membrane view of the structure of the cytochrome <i>b<sub>6</sub>f</i> complex, purified from the cyanobacterium <i>Nostoc</i> sp. (PDB 4OGQ).....	22
Figure 1.4: Schematic diagram of the transmembrane electron transport pathway between the hetero-oligomeric membrane protein complexes, PSII, cyt <i>b<sub>6</sub>f</i> and PSI, involved in photosynthesis [44]......	25
Figure 1.5: Stromal side view of PSI- LHCI supercomplex, depicting 15 protein subunits and 4 Lhca proteins [69]. .....	28
Figure 1.6.: Structure of the chloroplast ATP synthase, purified from pea plant, solved by cryo-EM to a resolution of 2.9Å (CF <sub>1</sub> ) to 3.4 Å (CF <sub>0</sub> ). [82].....	29
Figure 2.1: Sequence of generating sABs against the cytochrome <i>b<sub>6</sub>f</i> complex: (1) Binding of membrane protein in nanodiscs with phage library displaying non-specific Fab fragments. (2) Washing to remove Fabs which show weak or non-specific binding to the membrane protein. (3) Detergent solubilization of membrane protein and bound Fab particles. (4) Amplification of the specific Fab binders. [101].....	36
Figure 2.2: DSC spectra of cytochrome <i>b<sub>6</sub>f</i> complex solubilized in UDM, in the (i) absence of lipids (red), and (ii) in the presence of DOPC (Magenta), DOPG (Cyan) and SQDG (green). ...	39
Figure 2.3: DSC thermograms of the deconvoluted cytochrome <i>b<sub>6</sub>f</i> complex, in the presence of (A) UDM, (B) DOPG, (C) DOPC and (D) SQDG reveal three distinct transitions, labelled 1 (magenta), 2 (blue) and 3 (green)......	40
Figure 2.4: Lipid dependence of the thermal stability of the cytochrome <i>b<sub>6</sub>f</i> complex helical content (A) Representative $\alpha$ - helical far-UV CD spectrum of cytochrome <i>b<sub>6</sub>f</i> complex. (B) Helical secondary structure of cytochrome <i>b<sub>6</sub>f</i> complex, in the absence of lipids (red), and in the presence of DOPG (blue), DOPC (green) and SQDG (pink), as a function of temperature, measured at 222 nm by far-UV circular dichroism. (Inset) First derivative of the CD spectra, as a function of temperature, in the absence and presence of lipids. ....	42
Figure 2.5: Thermal stability of the helical content of the cytochrome <i>b<sub>6</sub>f</i> complex. First derivative of far-UV CD spectra measured at 222 nm, as a function of temperature, indicating thermal denaturation of UDM solubilized cytochrome <i>b<sub>6</sub>f</i> complex (red) in nanodiscs (blue) and bicelles (green). Thermal denaturation profile of the empty nanodiscs is shown in brown. ....	44

Figure 2.6: Single point protein ELISA of the binding of synthetic antibodies (sAbs) against cytochrome *b<sub>6</sub>f* complex eluted after 4<sup>th</sup> and 5<sup>th</sup> rounds of selection, represented by absorbance reading of quenched TMB ((3,3',5,5'-Tetramethylbenzidine) at 450 nm. .... 45

Figure 2.7: Monomerization of the cytochrome *b<sub>6</sub>f* complex as a function of temperature (38 - 44<sup>o</sup>C). (A) Representative clear native gel image showing (i) dimer (~240 kDa) and (ii) monomer bands (~120 kDa) of cytochrome *b<sub>6</sub>f* complex. (B) Rate of monomerization of the cytochrome complex measured in the absence of lipids (red) and in the presence of (i) SQDG, (ii) DOPG and (iii) DOPC. (iv) Overlay of the monomer: dimer ratio curves in the presence and absence of lipids. .... 47

Figure 2.8: Kinetics of the electron transfer activity measured through reduction of plastocyanin at 597 nm, of the cytochrome *b<sub>6</sub>f* complex, after incubation with phospholipase A<sub>2</sub> (dotted line), and after addition of DOPG (green), SQDG (pink) and DOPC (blue) to the deactivated complex. .... 48

Figure 2.9: Hydrogen peroxide produced as a by-product of the formation of low potential plasto-semiquinone by cytochrome *b<sub>6</sub>f* complex in the presence of DOPC, DOPG and SQDG, and upon treatment with phospholipase A<sub>2</sub> (PLP). Reaction conditions and statistical analyses specified in *Methods*. .... 49

Figure 2.10.: View along the membrane plane of the cytochrome *b<sub>6</sub>f* complex (PDB: 4OGQ). Highlighted in red is the anionic lipid SQDG interacting with residue K275 of the Rieske (yellow) and N20 of the cyt *f* subunit (pink). .... 52

Figure 2.11: Structural basis for the stabilization of activity of *b<sub>6</sub>f* by phosphatidyl-glycerol. (A) View along the membrane plane of the cytochrome *b<sub>6</sub>f* complex (PDB: 4OGQ). (B) Magnified view of the phospholipid binding sites (PG1 and PG2, red) lining the quinone portal connecting the intermonomer cavity and heme *b<sub>p</sub>*, lined by C (blue) and F (green) helices. (C) Magnified view of a phospholipid binding site ( PG 3, red) near the hinge region of the Rieske iron-sulfur protein (ISP, yellow). .... 54

Figure 3.1: Description of crystal structure of the trans-membrane cytochrome *bc<sub>1</sub>* complex from *Rb. capsulatus* (PDB 1ZRT), showing the protein subunits, redox prosthetic groups, and trans-membrane helices. .... 57

Figure 3.2: Gel analyses of cytochrome *bc<sub>1</sub>* complex purified from *Rhodobacter capsulatus*. (A) SDS PAGE showing the presence of three distinct subunits and (B) clear- native-PAGE showing the presence of the intact dimeric complex. .... 62

Figure 3.3: Reduced minus oxidized absorbance difference spectra of the *Rb. capsulatus* cytochrome *bc<sub>1</sub>* complex in 30 mM Tris-HCl, pH 7.5, 50 mM NaCl, 0.1mM EDTA, 0.04% DDM;  $\alpha$ -band absorbance difference spectra, with maxima at 551 nm and 560 nm, respectively, initially oxidized by ferricyanide (FeCN, 30  $\mu$ M), and subsequently reduced by sodium ascorbate (0.5 mM), yielding an absorbance difference spectrum (in red) with a peak at 551 nm. Subsequently, the sample was reduced with sodium dithionite (ca. 2 mM) yielding an absorbance maximum in the difference spectrum at 559 - 560 nm (green). Concentration of cytochrome complex, 30  $\mu$ M. The difference spectra were taken at time points 12s (cyan), 48s (dark blue), 96s (light green), 132s

(dark green), 168s (orange), 216 s (pink), 276 s (purple), and 324s (black), after addition of dithionite. .... 63

Figure 3.4.: Soret band absorbance and CD spectra; kinetics of absorbance and CD changes. Simultaneous measurement of the kinetics of reduction (dithionite concentration, 5 mM) and formation of the Soret band excitonically split CD spectrum of hemes,  $b_p$  and  $b_n$ , on the electrochemically positive, p, and negative, n, sides of the complex. Difference (Dith-Asc) absorbance (OD) (**A**) and CD (**B**) spectra are shown, which were measured 12 s (blue), 48 s (green), 96 s (pink), 168 s (gold), 264 s (cyan), 408 s (red), and 588 s (brown) after the addition of dithionite. (**C**) Kinetics of increase of OD and split CD (negative lobe) signals associated with dithionite reduction of the  $bc_1$  complex; absolute values of areas of absorbance peak in spectral range 424-436 nm (circles) and split CD peaks in range 432-440 nm (triangles) are shown. OD was fit using a double exponential function with the parameters:  $t_1$ ,  $0.13 \pm 0.02 \text{ s}^{-1}$  ( $A_1$ ,  $0.60 \pm 0.02$ ) and  $t_2$ ,  $5.0 \times 10^{-3} \pm 0.4 \times 10^{-3} \text{ s}^{-1}$  ( $A_2$ ,  $0.42 \pm 0.01$ ) for the change in optical density (OD, red line). Prediction of the kinetics of the split CD signal, with given OD signal, change according to “nn” (blue line) and “np” (green line) models is described in Figure 3.6. (**D**) Kinetics of the increase of OD and split CD signals associated with dithionite reduction of  $b_{cf}$  complex<sup>2</sup> were obtained as described for the  $bc_1$  complex (panel C). Data were fit using a double exponential formula:  $t_1$ ,  $0.14 \pm 0.02 \text{ s}^{-1}$  ( $A_1$ ,  $0.25 \pm 0.01$ ) and  $t_2$ ,  $6.6 \times 10^{-3} \pm 0.1 \times 10^{-3} \text{ s}^{-1}$  ( $A_2$ ,  $0.75 \pm 0.01$ ) for OD (red line); the simulation predicting the kinetics profile with give OD kinetics for CD (blue line). .... 65

Figure 3.5: (**A**) Inter-heme (Fe-Fe) distances between the two trans-membrane  $b$  hemes,  $b_p$  and  $b_n$ , in the *Rb. capsulatus* cytochrome  $bc_1$  complex (PDB 1ZRT). (**B**) Calculated relative amplitudes for the excitonically split CD spectra, based on heme distances and orientations in the crystal structure (PDB 1ZRT), for all reduced heme pairs: (i) p1-n1/p2-n2 (red), the dominant interaction; (ii) p1-n2 and p2-n1 (black and dark yellow); (iii) p1-p2 (blue), and (iv) n1-n2 (green)..... 67

Figure 3.6: Pathways for reduction of b-hemes in cytochrome  $bc$  complexes. State  $N_0$  in panels A, B describes fully oxidized hemes in the dimeric complex.  $N_i$  represent states of the complex in which subscript “i” represents the number of reduced (red) hemes. (**A**) n-n model: doubly reduced state of lowest energy of the dimer corresponding to reduction of the two  $b_n$  hemes on different subunits, which would generate a weak negative CD signal (Figure 3.5 B). (**B**) n-p model: the lowest doubly reduced state of dimer corresponding to reduction of  $b_n$  and  $b_p$  hemes in the same monomer. Sequence of 4 reduction-electron transfer events corresponding to complete reduction of the 4 hemes in the dimeric complex is shown. States  $N_1$ ,  $N_3$  would be bypassed if dithionite would act as a  $2 e^-$  donor..... 68

Figure 3.7: Distribution of the populations corresponding to the transfer of 0,1,2,3,4 electrons to each monomer of the dimeric complex and a sum of all 4 states (purple). .... 69

Figure 3.8: Structural alignment of hemes  $b_p$ ,  $b_n$  and  $c_n$  from the cyanobacterial  $b_{cf}$  complex (yellow; PDB 4OGQ) and bacterial  $bc_1$  (green, PDB 1ZRT). Residues R87 and R207 (yellow) are conserved in the  $b_{cf}$  complex, whereas they are replaced by A98 and H217 (green) in the  $bc_1$  complex. Glycine residue (G115) in the  $bc_1$  complex is replaced by a bulkier valine residue (V104) in  $b_{cf}$ . .... 74

Figure 3.9: (**A**) Structural alignment of D-helices lining the inter-monomer cavity in cyt  $bc_1$  (cyan, PDB 1ZRT) and  $b_{cf}$  complex (green, 4OGQ). The distance between F189 and L200 in the corresponding turn of the D-helix of the  $b_{cf}$  and  $bc_1$  complexes respectively, differ by  $2.4 \text{ \AA}$ , which

indicates the extent by which the distance between the two monomers is diminished in *b<sub>6</sub>f* compared to *b<sub>c1</sub>*. **(B)** Cartoon structures show that the N-terminal n-side surface helix of *b<sub>6</sub>f* (green), is displaced further from the n-side surface than the corresponding helix in *b<sub>c1</sub>* (cyan) by a distance of 5 Å, as indicated by the dotted line that bridges the two helices. .... 75

Figure 4.1: Distribution in thylakoid membranes between appressed (grana) and non-appressed (stroma) membranes of the major intra-membrane energy transducing complexes associated with oxygenic photosynthesis: photosystem II (PSII), photosystem I (PSI), cytochrome *b<sub>6</sub>f* complex, and ATP synthase, with molecular weights, respectively, of approximately 350, 530, 270 (with FNR), and 560 kDa. The possibility of localized reduction of CO<sub>2</sub>, suggested by the ATPase-PSI-FNR super-complex, is indicated. Light-harvesting chlorophyll complexes are not shown. .... 78

Figure 4.2: Purification and characterization of the PSI-ATPase-FNR super-complex. **(A)** 4-40 % sucrose density gradient of spinach thylakoid membrane extract. Super-complex (SC), marked by the arrow, is separated for further characterization. **(B)** 4-12 % Clear Native PAGE of the super-complex fraction isolated from the sucrose gradient and stained with Coomassie Brilliant Blue R-250. Bands marked I and II are the PSI-ATPase-FNR super-complex migrating at approximately 1.0 and 0.7 MDa. **(C)** Silver stained 2-D gel of the super-complex. **(D, E, F)** Western blots of super-complex fraction 1 using 12 % SDS-PAGE probed with antibodies raised against **(D)** α-subunit (55kDa) of *Arabidopsis* ATP synthase, **(E)** PsaA subunit (60 kDa) of PSI, and **(F)** FNR (36 kDa). .... 81

Figure 4.3: Difference fluorescence emission (top) and excitation (bottom) spectra of the ‘super-complex,’ measured with a FluoroMax 3 Fluorimeter (Horiba-Yvon Inc.). **(A)** Emission spectra measured between 500 – 600 nm. Stepping increment, 1 nm; Integration time, 0.1 sec; Excitation, 466 nm; the bandwidth was 5 nm for excitation and emission. **(B)** Excitation spectra measured in 400–500 nm range, measuring the emission at its 530 nm peak. Spectra of undiluted sample were measured in a quartz microcell, 3 x 3 mm, volume, 0.3 ml (Starna Cells) before and after addition of dithionite grains. Difference spectra were obtained by subtraction of spectra, i. e., ‘oxidized–reduced,’ measured before and after addition of dithionite. .... 84

Figure 4.4: ATPase Activity of the Super-Complex. As described in *Methods*, kinase activity was measured qualitatively through luciferase emission when the reaction mix was added: to lane 1 containing buffer and 0.4 mM ATP (negative control); to lane 2 containing purified super-complex and ATP (0.4 mM) in which the ATPase activity of the super-complex is assayed; to lane 3 with buffer and 0.4 mM ADP (positive control). Signal detected in lanes 1, 2, and 3 was  $2.3 \times 10^5$ ,  $1.9 \times 10^6$ , and  $4.7 \times 10^6$  cpm, respectively. Luminescence in lane 2 arises from hydrolysis of ATP to ADP and inorganic phosphate by the F1-ATPase. .... 85

Figure 4.5: Negative stain EM analysis of the PSI-ATPase Super-Complex. **(A)** Negative stain image of PSI-ATP synthase particle. The EM particle density is shown in white, while the stain and background are in black. **(B)** Crystal structures of PSI and ATP synthase re- Lipid bilayer drawn in yellow. n, p: electrochemically negative (stroma) and positive (lumen) sides of the membrane. **(C)** Overlay of crystal structures of PSI (blue, PDB ID 5L8R) and ATP synthase (red-green, PDB 5DN6) on the negative stain envelope of the PSI-ATP synthase super-complex particle. 47 trans-membrane helices of PSI, and 14 C- subunits of the F<sub>o</sub> ATPase overlay the EM image of the super-complex. .... 86

## LIST OF SYMBOLS, ABBREVIATIONS AND NOMENCLATURE

ATP	Adenosine triphosphate
$\beta$ -OG	n-octyl- $\beta$ -D-galactopyranoside
$b_p$ ,	<i>b</i> type heme bound on the electropositive side ( <i>p</i> -side) of the cytochrome <i>b<sub>6f</sub></i> complex
$b_n$ ,	<i>b</i> type heme bound on the electronegative side ( <i>n</i> -side) of the cytochrome <i>b<sub>6f</sub></i> complex
$c_6$	cytochrome 6
CD	circular dichroism
Chl	chlorophyll
Cyt	cytochrome
DDM	dodecyl- $\beta$ -D-maltoside
DGDG	digalactosyl-diacylglycerol
DOPC	Di-oleoyl phosphocholine
DOPG	Di-oleoyl phosphatidylglycerol
DSC	differential scanning calorimetry
$e^-$	electron
$\epsilon$	dielectric constant
EDTA	(ethylenedinitrilo) tetraacetic acid
ELISA	enzyme-linked immunosorbent assay
$E_m$	midpoint potential
$E_{m7}$	midpoint potential at pH 7
$\Delta\epsilon$	molar extinction coefficient
$\Delta A$	absorbance change
Fd	Ferredoxin
FNR	Ferredoxin-NADP <sup>+</sup> Reductase
$\Delta H$	change in enthalpy
ISP	iron-sulfur protein
Lhca	light-harvesting complex subunits
MGDG	monogalactosyl-diacyl glycerol

MSP	Membrane scaffold protein
<i>n</i> - and <i>p</i> - sides	electrochemically negative and positive sides of the membrane, respectively
NADP <sup>+</sup>	nicotinamide adenine dinucleotide phosphate
NADPH	reduced form of NADP <sup>+</sup>
PSI	Photosystem I
PSII	Photosystem II
Psa	subunits of PSI
PC	Plastocyanin
PLP	phospholipase A <sub>2</sub>
POPG	palmitoyl-oleoyl-phosphatidylglycerol
POPC	palmitoyl-oleoyl-phosphocholine
PQ	plastoquinone
PQH <sub>2</sub>	plastoquinol
Qp and Qn sites	quinone binding sites on the electrochemically positive and negative sides of the membrane-bound cytochromes <i>b<sub>6</sub>f</i> and <i>bc<sub>1</sub></i> complexes
sAb	synthetic antibody
SDS-PAGE	sodium dodecyl sulfate- polyacrylamide gel electrophoresis
SubIV	subunit IV of the <i>b<sub>6</sub>f</i> complex
SQDG	Sulfoquinovosyl-diacyl glycerol
TNES	buffer containing Tris-HCl, NaCl, EDTA and sucrose.
UDM	undecylmaltoside

## ABSTRACT

Author: Bhaduri, Satarupa. PhD

Institution: Purdue University

Degree Received: August 2019

Title: Structure-Function of Membrane Protein Complexes Involved in Oxygenic Photosynthesis

Committee Chair: William A. Cramer

The electron transport chain of oxygenic photosynthesis involves four major hetero-oligomeric membrane protein complexes: the photosystem II and photosystem I reaction center complexes, the cytochrome *b<sub>6</sub>f* complex, and the ATP synthase. Three aspects of the electron transport chain have been investigated in the present studies: (i) structure-function studies of the central proton-electron conducting cytochrome *b<sub>6</sub>f* complex, focusing on the effect of lipids in structural stabilization and electron transfer function; (ii) transmembrane electron transfer pathways in the cytochrome *b<sub>6</sub>f* and mitochondrial cytochrome *bc<sub>1</sub>* complexes, determined by heterogeneity in the internal polarity of the membrane protein complexes; and (iii) purification and characterization of a novel ~1 MDa supercomplex, dominated by the presence of photosystem I (PSI), ATP-synthase and ferredoxin-NADP<sup>+</sup> reductase (FNR) from higher plant system *Spinacea*.

Conclusions drawn from these studies are: (a) Addition of individual lipids, as well as incorporation into nanodiscs and bicelles, impart significant structural stabilization to a “delipidated” cytochrome *b<sub>6</sub>f* complex. Functions of individual lipids present in native thylakoid membrane have been determined. While the anionic sulfolipid, SQDG is critical for the stability of the dimeric complex, an anionic phospholipid, phosphatidyl-glycerol, restores the activity of an inactivated, delipidated dimeric cytochrome complex, hence emphasizing the role of lipids in the electron transfer function of the cytochrome complex; (b) The presence of internally bound lipids, along with water molecules, make the internal environment of membrane protein complexes, like the cytochrome complex, heterogeneous with respect to polarity or dielectric constant. The dielectric heterogeneity in turn influences the directionality of electron transfer through the cytochrome complexes, which was found to be different in the *b<sub>6</sub>f* complex, and its homologous counterpart in photosynthetic bacteria, the cytochrome *bc<sub>1</sub>* complex; (c) The novel super complex formed by PSI, ATP synthase and FNR, acts as a localized domain to facilitate and expedite the

shuttling of the two cofactors formed as byproducts of this complex, ATP and NADPH, to the CO<sub>2</sub> fixation cycle.

These studies provide an insight on the dynamic properties of the hetero-oligomeric membrane protein complexes in the chloroplast thylakoid membrane, and also show that both the internal and external membrane lipid environments, defined by the membrane lipid bilayer, affect the structure and function of the cytochrome *b<sub>6</sub>f* complex.

## CHAPTER 1. INTRODUCTION

### 1.1 Photosynthetic Electron Transfer Chain

Cyanobacteria, algae and higher plants utilize solar energy to assimilate carbon dioxide and produce molecular oxygen, in a process called oxygenic photosynthesis. In the first stage of photosynthesis, or the light dependent reactions, ATP and the reduced electron carrier, NADPH are formed, which are the major cofactors required for the next stage where the fixed carbon dioxide is converted into sugars [1]. In higher plants, the light dependent reactions take place in the thylakoid membranes, present inside specialized organelles called chloroplasts [2]. **Figure 1.1** shows the schematic process of non-cyclic photophosphorylation in which the captured light energy is harvested to form ATP and NADPH.

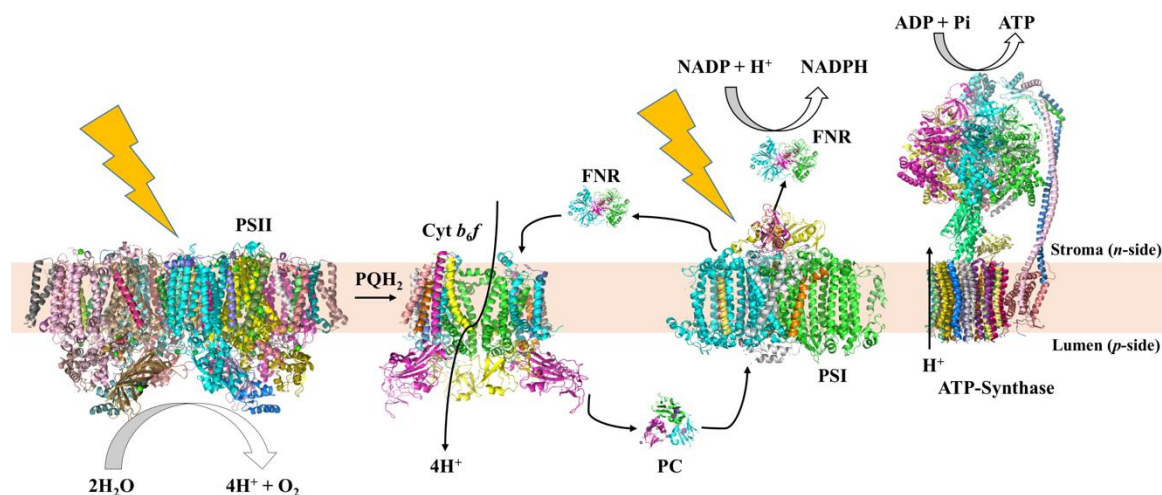


Figure 1.1: The electron transport chain in chloroplasts [3]

A description of the linear electron transport chain is given below [4-6].

Two hetero-oligomeric membrane protein complexes, photosystems I and II harvest light energy by the help of light harvesting complexes (LHC) comprised of protein subunits and photosynthetic pigments like chlorophyll a, chlorophyll b and carotenoids [7]. The excitation energy of the pigments is passed inward to the chlorophyll a special pair present in both the photosystems [4]. In PSII, the special pair absorbs light at a wavelength of 680 nm, so it is also called P680, while in PSI, optimum light energy is absorbed at 700 nm, hence the name P700 [8]. Excited P680 donates an electron to the primary electron acceptor in PSII, the pheophytin, which

is taken up by special lipophilic molecules called plastoquinones ( $\text{PQH}_2$ ) that diffuse through the thylakoid lipid bilayer to transfer the electron to the dimeric cytochrome  $b_6f$  complex [9]. The oxidized P680 is reduced by electrons generated by the splitting of water molecules with the help of the oxygen evolving complex (OEC) or the water splitting complex [10, 11]. The OEC binds and splits two molecules of water to form  $4 \text{H}^+$  and a molecule of oxygen [12].

The cytochrome  $b_6f$  complex passes the electron through heme moieties (discussed in section 1.3) to the soluble protein, plastocyanin (PC), as well as pumps  $4 \text{H}^+$  into the luminal side of the thylakoid membrane [13]. The electrochemical potential gradient formed due to (a) pumping of protons by the  $b_6f$  complex into the lumen, and (b) formation of  $\text{H}^+$  as an end product of splitting of water molecules by the PSII, is utilized by ATP synthase to form ATP from ADP and inorganic phosphate [14]. In the meantime, the electron taken up by PC is transferred to PSI. The low-energy electron which has passed along the downhill process is re-energized when the core of PSI, P700 absorbs photons, and the excited state electron is passed along a ferredoxin molecule to the enzyme,  $\text{NADP}^+$  reductase [4]. This enzyme catalyzes the conversion of  $\text{NADP}^+$  to NADPH, which along with ATP formed by ATP synthase, is passed to the second stage of photosynthesis, the Calvin cycle, where carbon dioxide is fixed to form sugars [4, 15]. This scheme of electron transfer is also called linear electron flow (LEF).

An additional pathway operates in oxygenic photosynthetic organisms, which transfer electrons from PSI to cytochrome  $b_6f$  on the electrochemically negative stromal side. This is the pathway of cyclic electron flow (CEF) [16]. CEF acts as a response mechanism to restore the balance of redox poise in the thylakoid membrane. An enzyme, ferredoxin- $\text{NADP}^+$ -reductase (FNR), found in association with the n-side surface of cytochrome  $b_6f$  [17] has been proposed to mediate the transfer of electrons from PSI to cytochrome  $b_6f$  through the oxidation of NADPH. Hence, the cytochrome  $b_6f$  complex lies at the center of both the LEF and CEF pathways of photosynthetic electron transfer [18].

## 1.2 Cytochrome *bc* Complexes

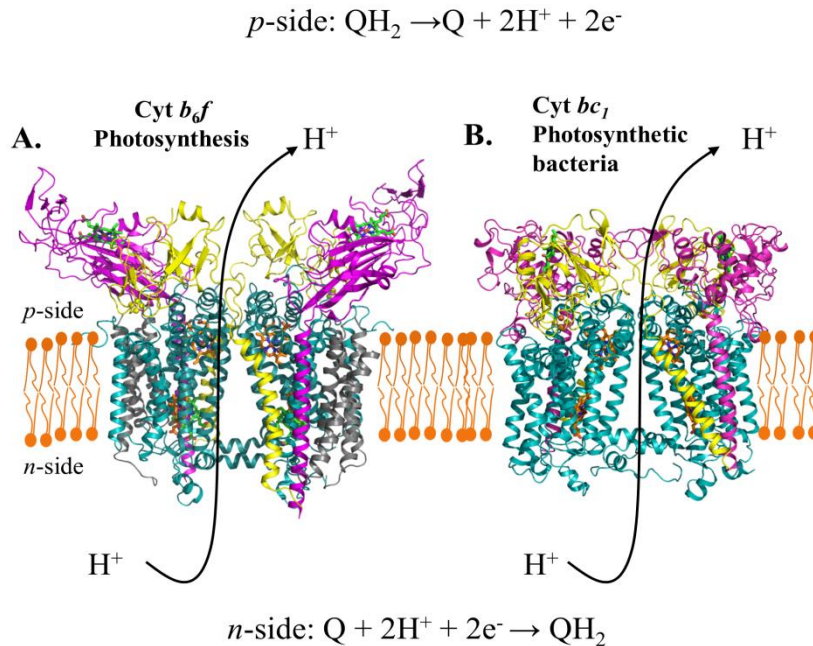


Figure 1.2: Cytochrome *bc* complexes involved in oxygenic photosynthesis: (A) Cytochrome *b<sub>6</sub>f* complex from the cyanobacterium *Nostoc* sp. (PDB 4OGQ) and (B) Cytochrome *bc<sub>1</sub>* complex from the photosynthetic bacterium *Rhodospirillum rubrum* (PDB 2QJP). Both complexes catalyze quinone reduction on the electropositive p-side or luminal side of the membrane, and quinone oxidation on the electronegative n-side or stromal side. The electron transport is coupled with pumping of protons from the n to p-side which generates an electrochemical potential across the membrane [19, 20]

Cytochrome *bc* complexes, comprised of cytochrome *b<sub>6</sub>f* (cyanobacteria, algae, plants) and homologous cytochrome *bc<sub>1</sub>* complex (photosynthetic and denitrifying bacteria, mitochondria) are the central electron-proton conducting hetero-oligomeric membrane protein complexes in the photosynthetic and respiratory electron transport chains (**Figure 1.2.**) [21, 22].

### 1.3 Cytochrome *b<sub>6</sub>f* complex:

The cytochrome *b<sub>6</sub>f* complex of oxygenic photosynthesis is an integral, hetero-oligomeric membrane lipoprotein that is a plastoquinol/plastocyanin cytochrome *c<sub>6</sub>* oxidoreductase belonging to the large family of *bc* protein complexes, present in photosynthetic organisms and mitochondria [13, 23, 24]. Structural information about the complex has been obtained from one algal source [25] and two cyanobacterial [26-28], the latest crystal structure being solved to 2.5 Å (**Figure 1.3**)

[28] (PDB 4OGQ). Each monomer consists of 8 distinct trans-membrane subunits- cyt  $b_6$  and Subunit IV consisting of 4 ("A-D") and 3 ("E-G") helices respectively, and single transmembrane helix subunits of cyt  $f$ , an iron-sulfur protein (ISP) and the small "Pet" subunits, Pet G, Pet L, Pet M and Pet N, the latter four forming a hydrophobic "picket fence" around the core subunits, and shows conservation with other  $bc$  complexes in both sequence and structure [27, 29]. The cytochrome  $b$  subunit is linked non-covalently to the transmembrane hemes,  $b_p$  and  $b_n$ , on the electrochemically positive (p) and negative (n) sides, and covalently to heme  $c_n$  [30] The recent 2.5 Å resolution structure of cytochrome  $b_6f$  from the cyanobacterium *Nostoc* PCC 7120 (**Figure 1.3**) has shown the presence of 23 unique lipid binding sites per monomer [31].

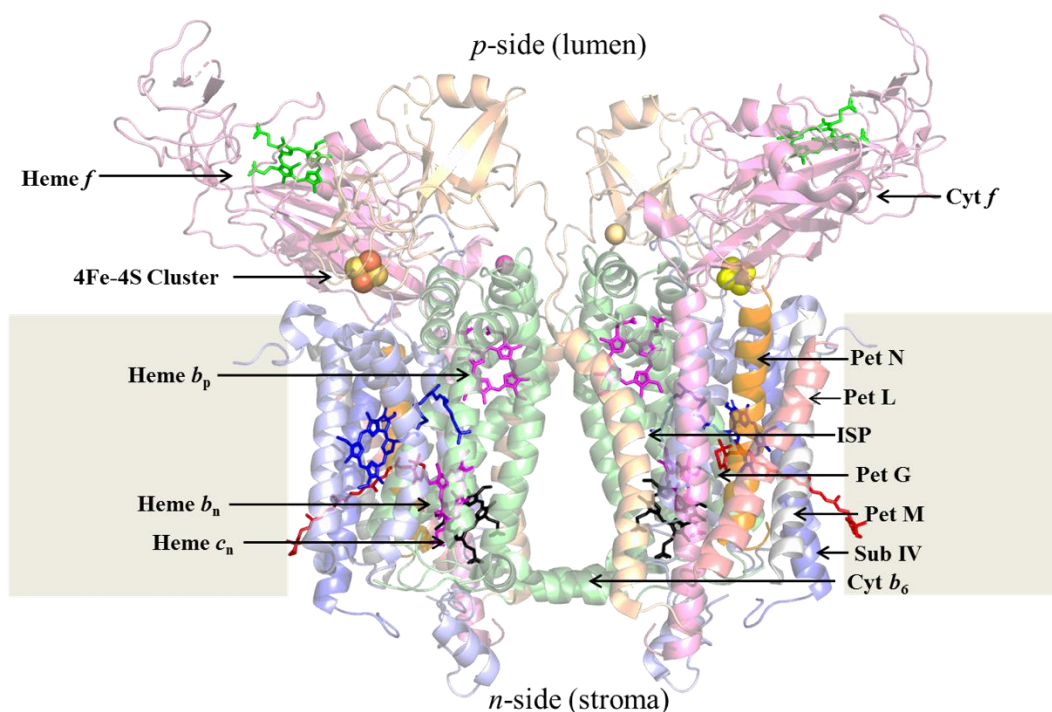


Figure 1.3: Membrane view of the structure of the cytochrome  $b_6f$  complex, purified from the cyanobacterium *Nostoc* sp. (PDB 4OGQ)

Table 1.1: Subunits and their corresponding molecular weights of the cytochrome  $b_6f$  complex (*Spinacea sp.*)

Subunits	Molecular weight (kDa)
Cytochrome $f$	32.035
Cytochrome $b$	24.782
PetC	18.938
PetD	17.313
PetG	4.198
PetL	3.972
PetM	3.478
PetN	3.197

### 1.3.1 Structural Similarities

The cytochrome  $b_6f$  and  $bc_1$  complexes share several common structural features. The subunit compositions of cytochromes  $b_6f$  and  $bc_1$  are listed in **Table 1.1**. The subunits  $b_6$  and subunit IV (SubIV) of the cytochrome  $b_6f$  complex are homologous with respect to sequence and hydrophobicity with the N and C-terminal domains of the cytochrome  $b$  (cyt  $b$ ) polypeptide of cyt  $bc_1$  [32].

However, there are some major structural differences between the cytochrome  $b_6f$  and  $bc_1$  complexes:

- 1) Although the cytochrome  $b_6$  subunit shares a similar structural arrangement with the N-terminal cyt  $b$  domain in cytochrome  $bc_1$ , SubIV is different from the C-terminal domain of cytochrome  $b$  subunit in  $bc_1$  complex due to (a) the presence of a unique chlorophyll (chl-a) a molecule between the F and G TMHs and (b) absence of helix H in subIV [27].

- 2) The single transmembrane helical subunit, cyt *f*, shares no conservation in sequence and structure with its counterpart in the cytochrome *bc*<sub>1</sub> complex, the cyt *c*<sub>1</sub> subunit. The soluble domain in the cytochrome *f* subunit is elongated and consists of  $\beta$ -sheets, while that in the cytochrome *c*<sub>1</sub> subunit is globular with an  $\alpha$ -helical arrangement [3, 33].
- 3) The Rieske ISP subunits share 47-61% sequence homology only in the [4Fe-4S] cluster binding regions [34, 35].
- 4) The small single transmembrane helical “picket fence” subunits, Pet G, L, M and N, present in the cytochrome *b*<sub>6</sub>*f* complex, do not have any homologous counterparts in the prokaryotic and photosynthetic cytochrome *bc*<sub>1</sub> complexes [20, 28].
- 5) There are three unique prosthetic groups which are present in the cytochrome *b*<sub>6</sub>*f* complex, but not in the *bc*<sub>1</sub> complex: (a) a covalently bound heme *c*<sub>n</sub> [27, 29] which is electronically coupled to the heme *b*<sub>n</sub> [36]; (b) a chlorophyll *a* molecule bound between the F and G helices of Sub IV; and (c) a  $\beta$ - carotene molecule [27, 37] separated by 14 Å from the chlorophyll-*a* molecule [38, 39]

### 1.3.2 Functional Similarities

Cytochromes *b*<sub>6</sub>*f* and *bc*<sub>1</sub> complexes facilitate transfer of electrons from plastoquinol to plastocyanin and ubiquinone to cytochrome *c*, respectively, and drive the electron transport chain [20]. The cytochrome complexes deprotonate and oxidize a QH<sub>2</sub> (reduced plastoquinol or ubiquinol) on the *p*-side of the membrane, first to a semi-quinone, QH<sup>•</sup>, and then to quinone Q [21, 40]. As an end product of both the steps, an electron and a proton are released. The protons are released to the aqueous phase of the *p*-side, which leads to the generation of a proton electrochemical gradient across the membrane [41]. The first electron is transferred from the deprotonated quinol to the [2Fe-2S] cluster of the Rieske ISP soluble domain. The cluster then donates the electron to heme *f* (cytochrome *b*<sub>6</sub>*f*) or *c*<sub>1</sub> (cytochrome *bc*<sub>1</sub>) through a mechanism that involves a large-scale motion of the ISP soluble domain in *bc*<sub>1</sub> [21, 41, 42]. Such a large-scale movement of the soluble domain has not been documented yet for the cytochrome *b*<sub>6</sub>*f* complex [34]. This pathway of electron transfer from a Q<sub>p</sub>-side bound plastoquinol molecule, to heme *f* or *c*<sub>1</sub> and then subsequently to plastocyanin /cytochrome *c*, constitutes the high potential chain of electron transfer [43] (**Figure 1.4**).

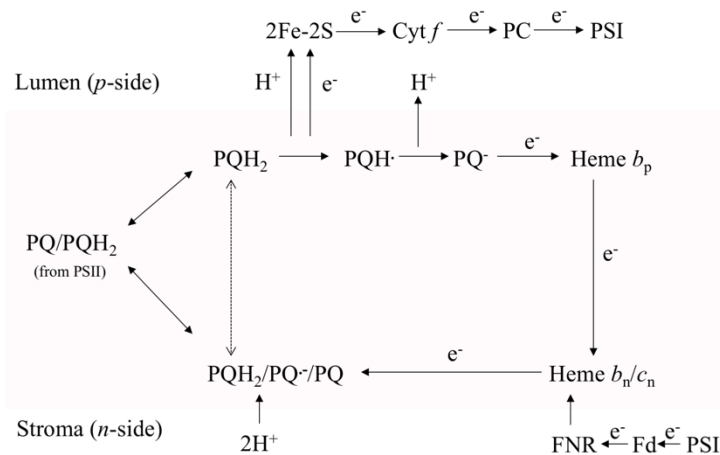


Figure 1.4: Schematic diagram of the transmembrane electron transport pathway between the hetero-oligomeric membrane protein complexes, PSII, cyt *b*<sub>6</sub>*f* and PSI, involved in photosynthesis [44].

Following the first round of deprotonation and oxidation, the partially oxidized  $\text{QH}^\bullet$  molecule undergoes deprotonation and further oxidation to form the fully oxidized Q. The proton is released to the aqueous phase of the *p*-side of the membrane, while the electron is transferred to an oxidized Q molecule bound at the  $\text{Q}_n$ -site on the *n*-side. Two electron transfer events are needed to reduce the *n*-side bound quinone to  $\text{QH}_2$ . However, for the *b*<sub>6</sub>*f* complex, this may not be an obligatory requirement depending on physiological conditions [43]. It was also not supported by measurements of the slow electrochromic phase proposed to be associated with the transmembrane electron transfer between *b*-hemes [45] nor by flash kinetic measurements [46]. The enzyme ferredoxin-NADP<sup>+</sup> reductase (FNR), which interacts with the *b*<sub>6</sub>*f* complex on the *n*-side, can donate an electron from NADPH to the  $\text{Q}_n$ -site to completely reduce the plastoquinone, hence bypassing some of the steps of the *p*-side  $\text{PQH}_2$  oxidation events required for the *n*-side reduction of PQ [17]. Such a cyclic transport pathway for electrons back to the cytochrome complex is absent in the cytochrome *bc*<sub>1</sub> complex [40]. The architecture of the  $\text{Q}_p$  and  $\text{Q}_n$  sites differ between the *b*<sub>6</sub>*f* and *bc*<sub>1</sub> complexes due to the unique presence of (a) heme *c*<sub>n</sub> electronically coupled to heme *b*<sub>n</sub> and (b) chlorophyll *a* molecule, bound to the *b*<sub>6</sub>*f* complex [27].

## 1.4 Interactions of Lipids with Membrane Proteins

Membrane proteins interact with lipids which contribute towards the structural stability and biological activity. There are three types of binding interactions between membrane proteins and lipids: (i) annular lipids surround the protein in the membrane and separate them from bulk membrane lipids; (ii) non-annular lipids, which are found attached in cavities and clefts, and often are responsible for interactions between adjacent subunits in oligomeric membrane proteins; and (iii) internal lipids, bound between transmembrane helices and near internal ligand binding sites [47, 48].

Lipids consist of a polar amphipathic head group and two hydrophobic alkyl tail groups. They interact with membrane protein complexes, either through specific interactions with the head groups or non-specific Van der Waal's interactions with the tail groups [49]. Due to such non-specific interactions, the native lipids can be substituted with synthetic lipids or detergents during purification [50, 51]. Specific lipid-protein interactions have been detected in many membrane protein complexes by high resolution structures solved by x-ray crystallography [52-54], cryo-EM microscopy [55, 56] and mass spectrometry [57-59]. High resolution structural information in hetero-oligomeric membrane protein complexes, like the cytochrome complexes, consisting of distinct polypeptide subunits have displayed the largest number of ordered lipid binding sites [28, 60].

### 1.4.1 Effects of Internal Lipids on Cytochrome *bc* Complexes

The 2.5 Å structure of the cytochrome *b<sub>6</sub>f* complex, purified from cyanobacterium *Nostoc sp.* has revealed the presence of 23 lipid binding sites per monomer of the complex [28]. The core of the cytochrome complex, comprised of *b<sub>6</sub>* subunit and Sub IV, is connected to the outer layer of “picket fence” single transmembrane helices by a layer of lipids [28]. The addition of the picket fence subunits to the core of the *b<sub>6</sub>f* complex is hypothesized to facilitate macromolecular interactions and supercomplex formation with other protein complexes in the electron-transport chain [43, 61]. The unique molecule of β-carotene has been proposed to be responsible for a supercomplex formation between the cytochrome *b<sub>6</sub>f* complex and PSI reaction center complexes [19]. Four major lipid constituents of the cytochrome complex are mono- and diacyl-galactosides (MGDG and DGDG), and the anionic dioleoyl-phosphatidyl glycerol (DOPG) and

sulphoquinovosyl-diacylgalactoside (SQDG) [61]. In respiratory supercomplexes, the anionic lipid, cardiolipin has been assigned as an assembly factor for respiratory supercomplexes [62-64]. The anionic lipids present in the photosynthetic complexes have however have not been studied for a major role in promotion of a supercomplex formation. It has been proposed that the internal lipids and chlorin ring of a chlorophyll molecule has substituted a transmembrane helix in Sub IV of the *b<sub>6</sub>f* complex, which is otherwise present in the homologous *bc<sub>1</sub>* complex [61]. The presence of internal lipids has also been implicated in structural stabilization of the iron-sulfur protein (ISP) subunit of the cytochrome *b<sub>6</sub>f* complex as well as n-side charge and polarity stabilization [61, 65].

### 1.5 Formation of Supercomplexes in Photosynthetic Electron Transport Chain

The membrane protein complexes involved in photosynthetic processes form macromolecular associations to facilitate:

- 1) **State transitions:** Reorganization of the PSII and PSI supercomplexes take place to dissipate any imbalance in light energy absorption by the two photosystems and their associated mobile antennas in the natural environments [66, 67]. Structures of photosynthetic supercomplexes studied thus far, associated with state transitions are: PSI-LHCI [68, 69], PSII-LHCII [70, 71] and PSI-LHCI-LHCII [72].
- 2) **Thermal dissipation of excess absorbed energy:** Vascular plants and algae have a developed non-photochemical quenching (NPQ) mechanism to dissipate excess absorbed light energy by the photosystems, which result in the formation of harmful reactive oxidative species. A process called qE quenching is well studied in which the light harvesting capability of PSII is downregulated upon excess absorption of light. A supercomplex, PSII-LHCII-LHCSR3, associated with qE quenching has been well characterized [73, 74].
- 3) **Cyclic electron flow (CEF).** To achieve the proper ratio of 3:2 for the ATP and NADPH formed, in order to facilitate CO<sub>2</sub> fixation, electron flow is directed in two pathways, linear electron transfer (LEF) and cyclic electron transfer (CEF) (as described previously). Several supercomplexes engaged in CEF have been studied such as (i) PSI-LHCI-cyt *b<sub>6</sub>f* [75] (ii) PSI-LHCI-LHCII-FNR-cytb<sub>6</sub>f-PGRL1[76] and (iii) cyt b<sub>6</sub>f-PSI—LHCII- NDH complex [77] and (iv) PSI-NDH1 supercomplex [78].

In the present studies, we have purified and characterized a novel supercomplex formed by PSI-ATP-synthase-FNR from higher plant system, *Spinacea*. It is hypothesized that this unique supercomplex is involved in efficient shuttling of ATP and NADPH to the CO<sub>2</sub> fixation cycle. The structural and functional aspects of PSI and ATP synthase are briefly described.

## 1.6 Photosystem I Reaction Center Complex

Photosystem I reaction center complex is a chlorophyll containing membrane protein complex which catalyzes light-driven electron transfer from plastocyanin on the *p*-side to the ferredoxin-NADP<sup>+</sup> reductase (FNR) on the *n*-side. FNR in turn reduces NADP<sup>+</sup> to form NADPH, which is shuttled to the CO<sub>2</sub> fixation cycle. High resolution crystal structures of plant photosystem I (PSI) revealed the presence of 15 subunits (Psa A-L and Psa N-P) and form supercomplexes with at least four light harvesting complexes (Lhca1-4) (**Figure 1.5**). The massive ~525 kDa complex harbors approximately 167 chlorophylls, 45 transmembrane helices, 2 phylloquinones and 3 [Fe-S] clusters [79, 80].

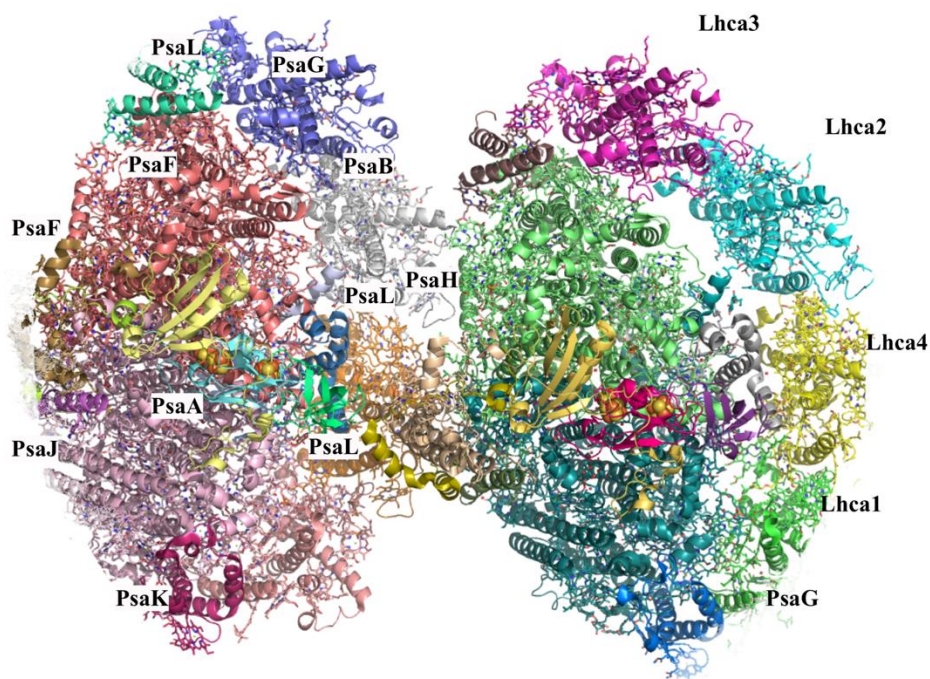


Figure 1.5: Stromal side view of PSI- LHCI supercomplex, depicting 15 protein subunits and 4 Lhca proteins [69].

## 1.7 ATP-synthase

ATP, the second cofactor required for CO<sub>2</sub> fixation besides NADPH, is formed by the F<sub>0</sub>-F<sub>1</sub> ATP synthase protein complex. In plants, the ATP synthase consists of 26 subunits, out of which 17 are integral or peripheral membrane subunits (**Figure 1.6**). The soluble cF<sub>1</sub> head consisting of the  $\alpha\beta$  subunits catalyze ATP synthesis which is powered by the CF<sub>0</sub> membrane bound rotary motor, which comprises 14 c subunits, each containing protonable glutamate residues. The membrane anchored a subunit is responsible for the conduction of H<sup>+</sup> to and from the glutamate residues in c subunits. Subunits  $\gamma$  and  $\epsilon$  transmits the torque from the membrane bound rotor to the catalytic cF<sub>1</sub> head, which synthesizes 3 ATP molecules per revolution of c-subunits. Subunits b, b' and  $\delta$  act as stators to prevent unproductive CF<sub>0</sub> rotation (Figure 1.6) [81, 82].

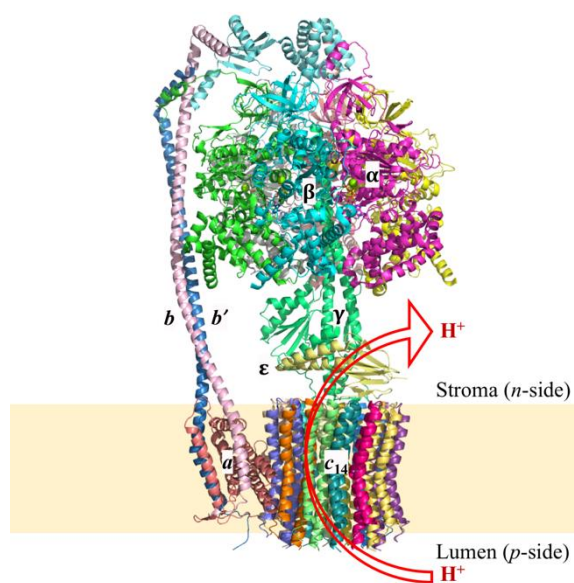


Figure 1.6.: Structure of the chloroplast ATP synthase, purified from pea plant, solved by cryo-EM to a resolution of 2.9 Å (CF<sub>1</sub>) to 3.4 Å (CF<sub>0</sub>). [82]

In the present study, three aspects of the electron transport chain are addressed:

- Lipid-protein interactions leading to structural and functional stabilization in the cytochrome *b<sub>6</sub>f* complex, purified from higher plant *Spinacea*. Roles of individual lipids in the structure-function of the cytochrome complex are determined by differential scanning calorimetry (DSC), far-UV circular dichroism (CD), native PAGE and electron transfer activity assays of function.

- The electron transport pathway and its dependence on internal polarity of the photosynthetic hetero-oligomeric cytochrome *bc* complexes, in bacteria and plants. It is established that the preferred path of heme reduction in the cytochrome *bc* complexes is dependent on the dielectric heterogeneity inside the complexes, defined by the presence of internal lipids and water molecules.
- Isolation and structural characterization of a novel super-complex formed by Photosystem I, ATP Synthase and FNR, purified from *Spinacea*.

## CHAPTER 2. STRUCTURE-FUNCTION OF THE CYTOCHROME $B_6F$ COMPLEX; LIPID DEPENDENCE.

### 2.1 Summary

The photosynthetic cytochrome  $b_6f$  complex, a homo-dimer consisting of eight distinct subunits and 26 transmembrane helices per monomer, catalyzes proton-coupled electron transfer across the thylakoid membranes for energy storage. The 2.5 Å resolution atomic structure of the complex from the cyanobacterium *Nostoc* sp. reveals the presence of 23 lipid binding sites per monomer. Although the crystal structure of the cytochrome  $b_6f$  from a plant source has not yet been solved, the identity of internal lipids present in a plant  $b_6f$  complex has been determined. The predominant lipid species are MGDG, DGDG, PG and SQDG. Despite the extensive structural analyses of  $b_6f$ -lipid interactions, the basis of the stabilization by lipids remains poorly understood. In the present study the effect of individual lipids on the structural and functional integrity of the  $b_6f$  complex, purified from *Spinacea*, is reported: (i) hydrophobic tail groups of provide structural stabilization to the complex; (ii) SQDG has a major role in stabilizing the dimeric complex; (iii)  $b_6f$  complex is stabilized by incorporation into nanodiscs or bicelles; (iv) removal of bound phospholipid by phospholipase A<sub>2</sub> inactivates the cytochrome complex; (v) activity can be restored significantly by the addition of the anionic lipid, phosphatidyl-glycerol, due to stabilization of the quinone portal and the hinge region of the iron sulfur protein.

### 2.2 Introduction

Four lipids dominate the lipid composition of the plant thylakoid membrane: phosphatidylglycerol (PG) (ca. 13%), di-galactosyl-diacylglycerol (DGDG) (32%), mono-galactosyl-diacylglycerol (MGDG) (40%) and sulfo-quinovosyl-diacylglycerol (SQDG) (15%) [83, 84]. The thylakoid lipids provide a bilayer matrix to support the proteo-lipid hetero-oligomeric complexes and, as a result of their hydrophobicity and low dielectric constant, facilitate generation of a trans-membrane proton electrochemical gradient coupled electron transport [31]. In addition, the lipids function as essential structural components in the photosynthetic complexes, as evident from high resolution crystal structures [28, 85-87] and mass spectrometry analyses [24, 57-59]. All four classes of lipids have been implicated in the biogenesis of the thylakoid membrane [31].

While MGDG deficiency has been shown to impair membrane energization and photo-protection [88], lack of DGDG causes dissociation of extrinsic proteins of PSII [84]. DGDG is also important for the function and stability of PSI [89]. The anionic lipid, PG, is critical for electron transport activity, as well as the structural integrity of PS II [90, 91]. The requirement of SQDG for proper photosynthetic functioning is, however, shown to be variable in different photosynthetic environments [92]. In *Arabidopsis*, it is dispensable under nutrient rich conditions [31]. However, in the *Chlamydomonas* green alga and cyanobacterium *Synechocystis*, SQDG is required for maintaining PSII activity [92, 93], although not in the cyanobacterium *Synechococcus* [93]. The present study is focused on the effect of the specific lipids on the structural stability and activity of the cytochrome *b<sub>6</sub>f* complex.

The *b<sub>6</sub>f* complex from cyanobacteria, algal and higher plant systems, like Spinacea, including prosthetic groups, is a ~ 240 kDa integral, membrane-embedded lipoprotein complex which mediates electron transfer between the photosystems I and II involved in oxygenic photosynthesis [28] consisting of eight subunits and seven prosthetic groups (**Table 2.1**).

Table 2.1: List of subunits and their molecular weights; and prosthetic groups, present in the cytochrome *b<sub>6</sub>f* complex, purified from *Spinacea* (62).

Subunits	Mol. Wt. (kDa)
Cyt f	31.9
Cyt b <sub>6</sub>	24.8
ISP	18.9
Subunit IV	17.3
PetG	4.1
Pet L	3.9
Pet M	3.4
Pet N	3.1

Prosthetic Groups	Number per monomer
Heme b	2
Heme c <sub>n</sub>	1
Heme f	1
2Fe-2S	1
Chlorophyll a	1
β-carotene	1

The best resolved crystal structure of the *b<sub>6</sub>f* complex, solved to 2.5Å, has been obtained from the cyanobacterium *Nostoc sp.* [28]. A distinguishing feature of this structure, compared to previously solved *b<sub>6</sub>f* structures, is the documentation of 23 lipid binding sites per monomer in the

dimeric complex [28]. Lipids associated with the *b<sub>6</sub>f* complex are responsible for regulation of conformation changes associated with the Rieske iron-sulfur protein subunit [94], tethering of the core and peripheral subunits [61] and with other hetero-oligomeric photosynthetic membrane protein complexes like Photosystem I [61]. It is significant to note that a majority of membrane protein structures show evidence of well-ordered lipid head-groups [95, 96]. In contrast, the cytochrome *b<sub>6</sub>f* crystal structure (PDB ID 4OGQ) shows electron density mainly for the hydrophobic fatty acid tails [28]. Moreover, the high-resolution crystallographic data (i.e., better than 3.0 Å resolution) of cytochrome *b<sub>6</sub>f* complex was achieved by augmentation of delipidated cytochrome *b<sub>6</sub>f* with pure, synthetic lipid DOPC or DOPG, whose 18:1 fatty acyl groups mimic the major fatty acid component in the thylakoid membrane [97]. The fact that high resolution structural data on the cytochrome *b<sub>6</sub>f* complex was obtained in an artificial lipid environment that mimicked the predominant fatty acid composition of the thylakoid lipid bilayer might imply that structural stability and function of the cytochrome *b<sub>6</sub>f* complex is dependent on the lipid environment of the multi-subunit membrane protein complex.

It is shown in the present study that lipid hydrophobic tail groups contribute significantly to the structural stability of the complex. The synthetic lipids, DOPC and DOPG are approximately equivalent in their ability to stabilize the secondary and tertiary structure of the cytochrome complex. Incorporation of the complex in **(a)** nanodiscs, composed of DOPC and DOPG (3:1), and **(b)** bicelles (DMPC: CHAPSO = 0.5) stabilized the secondary structure of the *b<sub>6</sub>f* complex, purified from *Spinacea*. Even though phosphatidyl-choline (PC) is not present in the native plant thylakoid membrane, synthetic PC containing fatty acyl chains mimicking the native hydrophobic environment, stabilize the structure of the complex. Conformationally selective synthetic antibodies (sAbs) or Fab binders against nanodisc-reconstituted cytochrome *b<sub>6</sub>f* complex, did not bind to detergent solubilized cytochrome complex, indicating different adopted conformations in the two hydrophobic environments. The native thylakoid membrane sulfolipid SQDG plays a significant role in the dimer stabilization of the complex. It is shown that while significant removal of bound phospholipids substantially inactivates the cytochrome complex, subsequent addition of DOPG to the deactivated complex can restore the activity of the complex by a factor as large as 1.6-fold, thus implicating the anionic phospholipid as essential for the native activity of the *b<sub>6</sub>f* complex.

## 2.3 Materials and Methods

### 2.3.1 Purification of cytochrome *b<sub>6</sub>f* complex from spinach.

The cytochrome *b<sub>6</sub>f* complex was isolated from leaves of commercially purchased spinach as described previously [98]. Dimeric *b<sub>6</sub>f* complex was separated from monomer fractions by sucrose density gradient and size exclusion chromatography. All further analysis was performed in 30 mM Tris-HCl (pH 8.0), 50 mM NaCl, 0.1 mM EDTA, 10% sucrose (TNES) and 0.04% UDM. For experiments with the cytochrome complex supplemented with additional lipids, 1 mM solutions of individual lipids were prepared from stock solutions of 25 mg/ml concentration.

### 2.3.2 Differential Scanning Calorimetry (DSC).

DSC analyses were carried out on a Nano-DSC instrument (TA Instruments) in collaboration with Dr. Huamin Zhang (SSCI, West Lafayette), equipped with two 0.3 mL platinum capillary cells. Sample solutions, at a concentration of 3  $\mu$ M, were degassed for 10 min at 20 °C before loading in the capillary cells. DSC scans were conducted from 25 °C to 90 °C at a scan rate of 1°C/min. Experiments were initiated using the DSCRun software, and data analyses performed using NanoAnalyze software. A two-state model was used to determine whether the transition is two-state or multi-state based on the values of  $\Delta H$  (enthalpy change) measured by DSC.

### 2.3.3 Circular Dichroism (CD).

Far-UV CD spectra were measured in the wavelength range of 200-250 nm by employing a spectropolarimeter [“Chirascan” (Applied Photophysics Ltd. UK)] with a cell path length of 1 cm and protein concentration of 0.5  $\mu$ M. For thermal denaturation studies, the wavelength was fixed at 222 nm and simultaneous OD and CD scans were measured from 30°C to 70°C at a scan rate of 1°C/min. Data fitting and analyses were performed using SigmaPlot software.

### 2.3.4 Secondary structure calculation.

The content of secondary structure in the cytochrome *b<sub>6</sub>f* complex was measured using the crystal structure data (PDB ID 4OGQ) using the software STRIDE.

### 2.3.5 *Thermal denaturation and Native-PAGE.*

Cytochrome *b<sub>6</sub>f* complex (5 $\mu$ M) in TNES-UDM buffer (pH 8.0), in the presence and absence of lipids, was heated at the indicated temperatures for 5 min and immediately transferred to ice. The samples were run on 4-12% gradient native gels to study the dependence of the monomerization process on temperature. Densitometry analyses were done using ImageJ software [99, 100].

### 2.3.6 *Encapsulation of cytochrome b<sub>6</sub>f complex into nanodiscs.*

Cytochrome *b<sub>6</sub>f* (5  $\mu$ M) was incubated overnight with mixed micelles of DOPC/DOPC at a molar ratio of 1:1000, buffer (30 mM Tris, pH 8.0, 150 mM NaCl, 1mM EDTA, 0.03% UDM), membrane scaffold protein, MSP2N2, (provided by A. Kossiakkoff) with the *b<sub>6</sub>f* complex, at a molar ratio of 1:10, and biobeads for the removal of detergents (Sigma). The biobeads were removed from the nanodisc complex, which was concentrated and checked for successful reconstitution by size-exclusion chromatography and SDS-polyacrylamide gel electrophoresis (SDS-PAGE).

### 2.3.7 *Generation of synthetic antibodies (sAbs/Fabs) against the cytochrome b<sub>6</sub>f complex in nanodiscs by competitive and subtractive phage display selection (In collaboration with S. Erramilli, T. Kossiakkoff, University of Chicago).*

A schematic of the overall process of generation of synthetic antibody generation by phage display technique is shown in **Figure 2.1**[101].

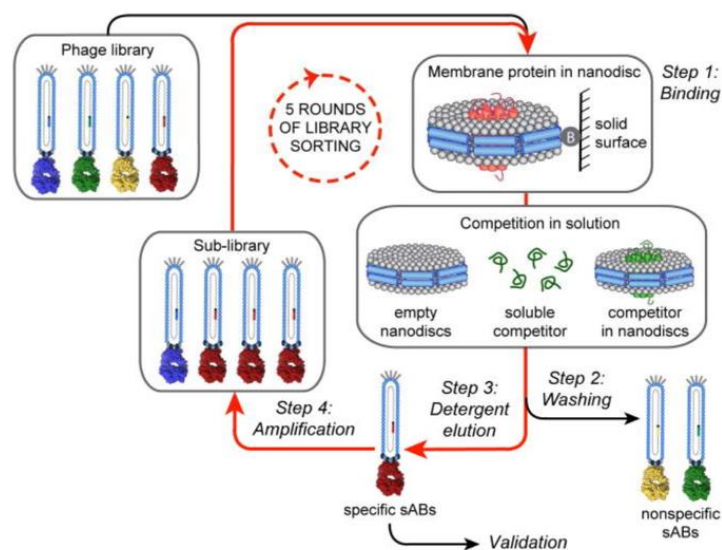


Figure 2.1: Sequence of generating sABs against the cytochrome *b<sub>6</sub>f* complex: (1) Binding of membrane protein in nanodiscs with phage library displaying non-specific Fab fragments. (2) Washing to remove Fabs which show weak or non-specific binding to the membrane protein. (3) Detergent solubilization of membrane protein and bound Fab particles. (4) Amplification of the specific Fab binders. [101]

Experimentally, 20 mL of 2YT media was inoculated with 100  $\mu$ L *E.coli* XL1 cells, in the presence of tetracycline, as antibiotic resistance. As control, 2 mL of 2YT media was inoculated with XL1 cells in the presence of Ampicillin and Kanamycin. In parallel, 4 mL of TBS buffer was incubated with 1 mL of PEG 8000 and 225  $\mu$ L phage library, on ice for 1 hr. 70  $\mu$ L *b<sub>6</sub>f* complex in biotinylated 2N2 nanodiscs was mixed with 90  $\mu$ L selection buffer (30 mM Tris, pH 7.5, 150 mM NaCl, 1 mM EDTA and 1% BSA). The phage was spun down at 8000 rpm for 1 hr and resuspended in 250  $\mu$ L selection buffer. To immobilize the *b<sub>6</sub>f* - nanodiscs complex, 250  $\mu$ L streptavidin tagged beads were washed and mixed with 160  $\mu$ L protein and incubated for 30 min, washed with buffer and incubated with phage for 1 hr. For selection of protein specific binders, empty nanodiscs were added to the mixture, which was finally mixed with 5 mL log phase XL-1 cells and 30 mL 2YT/ Ampicillin/ Helper phage and incubated for 20 hr. Phage culture was spun down at 8000 g for 10 min and mixed with PEG 8000/ 2.5 M NaCl solution and set up for a second round of selection and further amplification. 5 rounds of selection and amplification of the clones for Fab binders, were done.

### 2.3.8 Validation by Single-Point ELISA (enzyme-linked immunosorbent assay).

Single colonies of XL-1 cells infected with phage elution after 4<sup>th</sup> and 5<sup>th</sup> rounds of selection (48 colonies each) were inoculated into 96-well plates containing 2YT media, ampicillin and helper phage KO7. Plates were sealed and incubated at 37°C shaking overnight. The plates were centrifuged and supernatant containing phage particles were transferred into fresh plate.

ELISA plates were coated with neutravidin in solution and incubated for 2 hrs under shaking at room temperature, and then blocked with ELISA buffer. In a separate tube 20nM solution of biotinylated nanodiscs containing cytochrome *b<sub>6f</sub>* was prepared in ELISA buffer.

For each phage screen, three ELISA wells were prepared (i) buffer alone, (ii) biotinylated empty nanodiscs and (iii) biotinylated nanodiscs with cytochrome *b<sub>6f</sub>* embedded. To each well assayed, overnight incubated and diluted phage was added and incubated under shaking. For visualization, HRP (Horse Radish Peroxidase)-conjugated anti-M13 antibody was added followed by addition of H<sub>2</sub>O<sub>2</sub> and TMB (3,3',5,5'-Tetramethylbenzidine) substrate. Signals from wells quenched with 1M HCl and absorbance measured for each well at 450nm.

Note: ELISA Buffer used: 30 mM Tris pH 7.5, 150 mM NaCl, 1 mM EDTA, 2% BSA

Cyt. *b<sub>6f</sub>* in 2N2 nanodisc made of DOPC/ DOPG (3:1) = 20nM; Empty biotinylated nanodisc concentration = 50 nM

### 2.3.9 Encapsulation of cytochrome *b<sub>6f</sub>* complex into bicelles

A mixture of DMPC:CHAPSO at a molar ratio of 0.5 was prepared by measuring the appropriate amounts and dissolving in deionized water. The final bicelle concentration was kept at 12% (%v/v). 5 μM cytochrome *b<sub>6f</sub>* was added to bicelle suspension, mixed by pipetting, and incubated for 1 hr on ice.

### 2.3.10 Removal of phospholipids by phospholipase A<sub>2</sub>

15 μM bee venom Phospholipase A<sub>2</sub> (PLP, Sigma), was mixed with 15 μM cytochrome *b<sub>6f</sub>* complex, in 20 mM MOPS, pH 7.2, 20% glycerol, 50 mM CaCl<sub>2</sub> and 0.04% UDM, and incubated at room temperature for 2 hr. The reaction was stopped by addition of 50 mM EDTA.

### 2.3.11 *Electron transfer activity assay.*

Cytochrome *b<sub>6</sub>f* complex in spinach thylakoid membranes, conduct electrons from donor decyl-plastoquinol (dPQH<sub>2</sub>) to acceptor plastocyanin (PC). dPQH<sub>2</sub> at a concentration of 10 μM was added to the assay buffer (Tris-HCl, pH 6.0, 0.04% UDM) and a baseline was recorded. To initiate the electron transfer reaction, 5 μM of cytochrome *b<sub>6</sub>f* and PC were added to the reaction mixture and absorbance kinetics was studied by the absorbance change at 597 nm [17].

### 2.3.12 *Superoxide production:*

Superoxide production by the cytochrome *b<sub>6</sub>f* complex was measured fluorometrically, as a function of hydrogen peroxide formed, using the Amplex Red Hydrogen Peroxide/ Peroxidase Assay Kit (Invitrogen). In the presence of saturating amounts of superoxide dismutase (SOD), superoxide released from the cytochrome complex, is converted into H<sub>2</sub>O<sub>2</sub> [102]. ADHP (10-Acetyl-3,7-dihydroxyphenoxazine), also known as Amplex Red, reacts with H<sub>2</sub>O<sub>2</sub> in a 1:1 ratio, with horseradish peroxidase (HRP) acting as a catalyst, to form fluorescent resofurin [103]. A working reaction buffer, containing 100 μM ADHP and 0.2 U/ml HRP, was mixed with 50 μM horse cytochrome *c*, 300 U/ml SOD, and 20 μM decyl-plastoquinone, and 0.04% UDM. The reaction was started by addition of a final concentration of 1 μM *b<sub>6</sub>f* complex at room temperature. The resofurin produced was measured by excitation and emission at 530 nm and 590 nm, respectively, using a Spectramax M5 Multimode Microplate Reader (Molecular Devices). Statistical analyses were done with Sigmaplot software, using two-tailed unpaired t-test (one variable). In all tests a 95% confidence interval was used for which  $p < 0.05$  was considered statistically significant.

## 2.4 Results

### 2.4.1 *Differential scanning calorimetry (DSC):*

(In collaboration with Dr. Huamin Zhang, SSCI)

Thermal denaturation of the cytochrome *b<sub>6</sub>f* complex, purified from spinach, was monitored by DSC at a scan rate of 1<sup>o</sup>C/min. An overlay of the DSC thermograms for the complex in the presence and absence of lipids is shown (**Figure 2.2**). The enthalpies of heat-induced

unfolding ( $\Delta H$ ) and the melting temperatures ( $T_m$ ) of the cytochrome complex in the absence and presence of lipids are summarized (**Table 2.2**).

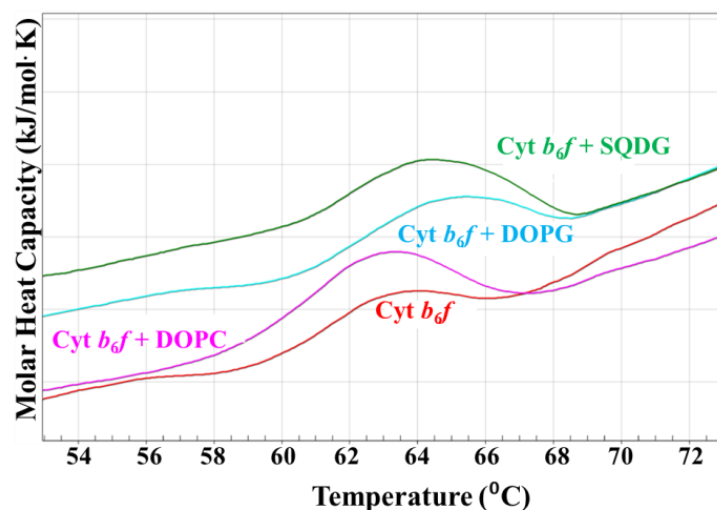


Figure 2.2: DSC spectra of cytochrome  $b_6f$  complex solubilized in UDM, in the (i) absence of lipids (red), and (ii) in the presence of DOPC (Magenta), DOPG (Cyan) and SQDG (green).

Table 2.2.: Comparison of the enthalpy and melting temperature ( $T_m$ ) of the delipidated cytochrome  $b_6f$  complex and in the presence of DOPG, DOPC, and SQDG.

Cyt $b_6f$	$T_m$ ( $^{\circ}\text{C}$ )	Enthalpy, $\Delta H$ (kJ/mol)
UDM	62.8	115.3
UDM + DOPG	64.5	170.6
UDM + DOPC	63.1	220.0
UDM + SQDG	64.6	218.2

Addition of the anionic lipids, DOPG and SQDG, to the cytochrome complex caused an increase in the mean  $T_m$ , by 1.8  $^{\circ}\text{C}$  and 1.9  $^{\circ}\text{C}$ , respectively (**Figure 2.2**, **Table 2.2**). DOPC, however, when added at the same molar concentration, did not increase the  $T_m$  of the complex significantly. Addition of each of the three lipids significantly increased the enthalpy associated with the unfolding of the cytochrome complex. Although the increase in  $T_m$  in the presence of DOPC is not significant, a large increase in the enthalpy change, associated with the unfolding of

the protein complex, might indicate a mechanism of stabilization that is different from that caused by the anionic lipids, DOPG and SQDG.

Deconvoluted DSC thermograms showed three distinct transition peaks (**Figure 2.3**), suggesting that the thermal denaturation of the cytochrome complex occurs via three distinct domain unfolding events whose molecular basis is currently not understood. It is evident that the  $T_m$  for the three transitions is shifted to higher temperatures in the presence of lipid (**Table 2.3**). Thus, all three lipids, DOPG, DOPC and SQDG confer a significant degree of structural stability to the cytochrome complex.

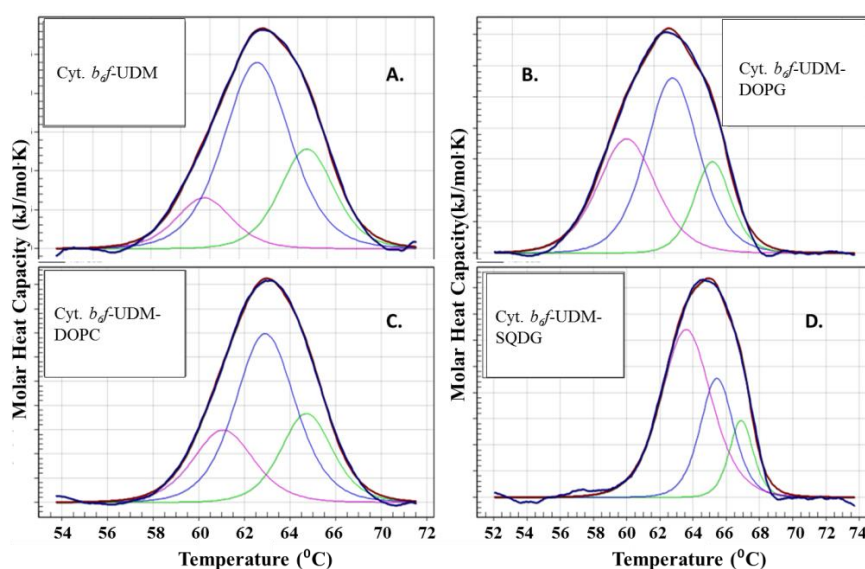


Figure 2.3: DSC thermograms of the deconvoluted cytochrome  $b_6f$  complex, in the presence of (A) UDM, (B) DOPG, (C) DOPC and (D) SQDG reveal three distinct transitions, labelled 1 (magenta), 2 (blue) and 3 (green).

Table 2.3: Comparison of the  $T_m$  of the three transitions (1, 2 and 3) obtained from deconvolution of the DSC thermograms for the cytochrome *b<sub>6</sub>f* complex in the presence of DOPG, DOPC, and SQDG. Note: the enthalpies of the individual transitions add up to the final  $\Delta H$  values (Table 2.2).

Cyt <i>b<sub>6</sub>f</i>	Delipidated		Delipidated+DOP G		Delipidated+ DOPC		Delipidated+ SQDG	
	$T_m$ (°C)	Enthalpy (kJ/mol)	$T_m$ (°C)	Enthalpy (kJ/mol)	$T_m$ (°C)	Enthalpy (kJ/mol)	$T_m$ (°C)	Enthalpy (kJ/mol)
Transition 1 (magenta)	60.8	16	62.9	60	61.1	53	63.6	129
Transition 2 (blue)	62.6	73	64.8	84	62.9	121	65.4	61
Transition 3 (green)	64.3	32	66.5	31	64.7	56	66.9	28

#### 2.4.2 Thermal denaturation / far-UV circular dichroism.

(a) Effect of lipid in the thermal denaturation of *b<sub>6</sub>f* complex.

The secondary structure content of the *b<sub>6</sub>f* complex from *Nostoc* (PDB 4OGQ) is 45.1%  $\alpha$ -helix and 12.6%  $\beta$ -strand (**Table 2.4**).

Table 2.4: Secondary structure content of the *b<sub>6</sub>f* complex from *Nostoc* sp. (PDB 4OGQ).

Secondary structure	Content (%)
$\alpha$ - helix	45.2
$\beta$ - strand	12.6
310-helix	2.9
Turn	18.7
Coil	18.2
Bridge	2.4

The unfolding of the cytochrome complex, as a function of temperature in the presence and absence of lipid, was studied by monitoring the change in molar ellipticity, at a wavelength of 222 nm, the peak for  $\alpha$ -helical secondary structure (**Figure 2.4 A**) [104]. At this wavelength the extinction coefficient of the  $\beta$ -strand structure is approximately a third of that for  $\alpha$ -helix [105].

An overlay of the thermal denaturation spectra of the cytochrome-detergent complex in the presence of DOPG, DOPC and SQDG (**Figure 2.4 B**) reveals an increase in thermal stability of the complex in the presence of lipid. The mid-point of the transition,  $T_m$ , was determined more precisely from the first derivative of the ‘melting curve’ as a function of temperature (**Figure 2.4B, inset**).

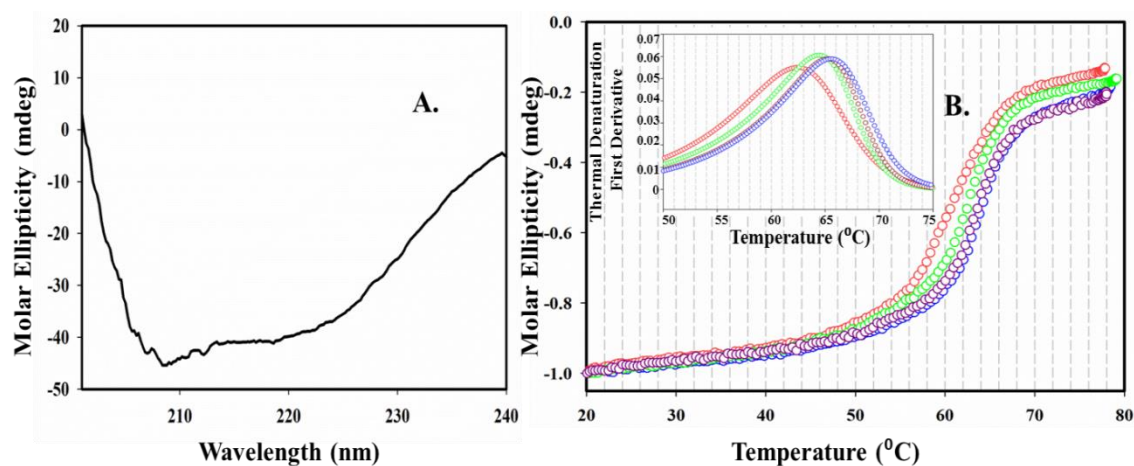


Figure 2.4: Lipid dependence of the thermal stability of the cytochrome  $b_6f$  complex helical content (A) Representative  $\alpha$ - helical far-UV CD spectrum of cytochrome  $b_6f$  complex. (B) Helical secondary structure of cytochrome  $b_6f$  complex, in the absence of lipids (red), and in the presence of DOPG (blue), DOPC (green) and SQDG (pink), as a function of temperature, measured at 222 nm by far-UV circular dichroism. (Inset) First derivative of the CD spectra, as a function of temperature, in the absence and presence of lipids.

The addition of each of the three lipids, DOPC, DOPG and SQDG, stabilized the structure as indicated by the shift of the  $T_m$  to higher temperatures (**Table 2.5**). SQDG and DOPG cause a stabilization effect similar to that found by DSC (**Table 2.2**). However, DOPC confers a greater degree of secondary structure stabilization, than its effect on the tertiary structure as measured by DSC (**Table 2.5**).

To determine the effects of different hydrophobic tail groups of PC and PG, the effect of dioleoyl and palmitoyl groups on the  $T_m$  of the cytochrome complex was compared. Both POPG and DOPG increased the  $T_m$  of the complex comparably (64.4 and 63.8 °C, respectively) (**Table 2.5**). However, POPC displayed a larger stabilizing effect on the cytochrome complex than DOPC (**Table 2.5**). The increase in structure stabilization by PC, which is not present in the thylakoid membrane, is attributed to its hydrophobic fatty acid acyl chains.

Table 2.5: Comparison of the melting temperatures ( $T_m$ ) of the cytochrome  $b_6f$  complex solubilized in UDM, in the absence and presence of DOPG, DOPC, and SQDG, as measured by far-UV circular dichroism at 222 nm. Standard deviation determined from 3 trials.

Cyt $b_6f$ complex	$T_m$ (°C)
UDM solubilized	$62.1 \pm 0.25$
UDM +DOPG	$64.4 \pm 0.3$
UDM + POPG	$63.8 \pm 2.6$
UDM +DOPC	$65.4 \pm 1.04$
UDM + POPC	$68.4 \pm 0.56$
UDM +SQDG	$65.3 \pm 0.96$

Removal of internally bound phospholipid which co-purify with the cytochrome  $b_6f$  complex by phospholipase  $A_2$  (cleaves the *sn*-2 bond of phospholipids) did not affect the  $T_m$  of the complex significantly, as determined by the temperature dependence of the amplitude of CD spectrum at 222 nm (**Table 2.6**).

Table 2.6: Comparison of the melting temperatures ( $T_m$ ) of the delipidated cytochrome  $b_6f$  complex before and after addition of phospholipase  $A_2$ , measured by far-UV CD. Standard deviation determined from 3 trials.

Cyt $b_6f$ complex	$T_m$ (°C)
UDM solubilized	$62.1 \pm 0.25$
phospholipase $A_2$	$61.6 \pm 0.4$

**(b) Thermal denaturation of  $b_6f$  complex in nanodiscs and bicelles**

Stabilization of the  $b_6f$  complex by the hydrophobicity of the lipid bilayer was observed when the cytochrome complex was incorporated into more native environments associated with nanodiscs and bicelles. Successful reconstitution of the  $b_6f$  complex in nanodiscs was confirmed by size-exclusion chromatography in which the cytochrome complex in nanodiscs elutes earlier as a consequence of its larger molecular weight (data not shown).

A comparison was made of the thermal melting stability of the cytochrome complex, studied by far-UV CD at 222 nm, in the presence of nanodiscs and phospholipid bicelles. The denaturation profiles of the  $b_6f$  complex in nanodiscs and bicelles reveal a larger increase in the

$T_m$  of the *b<sub>6</sub>f* complex (by 7.3<sup>0</sup>C and 5.9<sup>0</sup>C, respectively (**Figure 2.5, Table 2.7**)), when compared to the complex in lipids, implying significant stabilization. The first derivative of the thermal denaturation curve for *b<sub>6</sub>f* in nanodiscs (blue, **Figure 2. 5**) shows a residual signal between 20<sup>0</sup>C and 50<sup>0</sup>C, caused by the presence of the  $\alpha$ - helical MSP belt around the nanodisc, which has a broad melting profile in that temperature range (brown function, **Figure 2.5**).

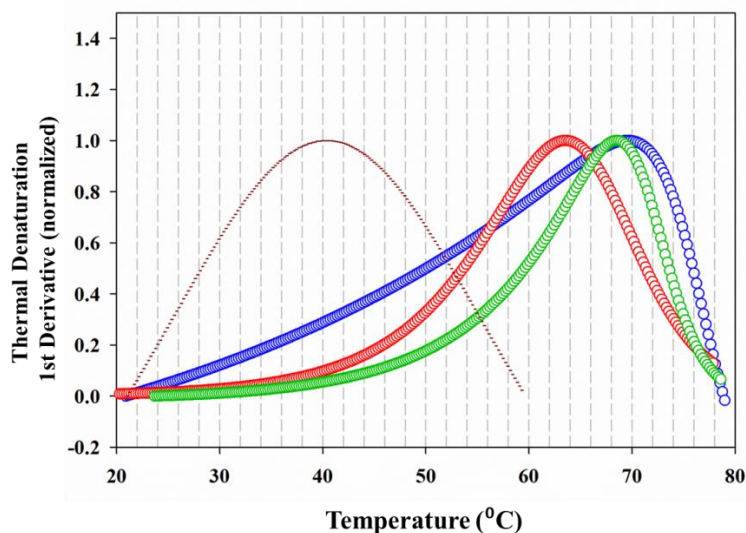


Figure 2.5: Thermal stability of the helical content of the cytochrome *b<sub>6</sub>f* complex. First derivative of far-UV CD spectra measured at 222 nm, as a function of temperature, indicating thermal denaturation of UDM solubilized cytochrome *b<sub>6</sub>f* complex (red) in nanodiscs (blue) and bicelles (green). Thermal denaturation profile of the empty nanodiscs is shown in brown.

Table 2.7: Comparison of the melting temperatures ( $T_m$ ) of the cytochrome *b<sub>6</sub>f* complex in UDM and in the presence of nanodiscs and bicelles, measured by far UV-CD. Standard deviation determined from 3 trials.

Cyt <i>b<sub>6</sub>f</i> complex	$T_m$ (°C)
UDM solubilized	$62.1 \pm 0.25$
In Bicelle	$68.2 \pm 0.7$
In Nanodisc	$69.6 \pm 0.34$

These results suggest that the hydrophobic environment of the membrane systems, defined mainly by the non-native PC lipids, with tail groups closely mimicking those of the thylakoid lipids in terms of length and degree of unsaturation, is sufficient to increase the structural stability of the *b<sub>6</sub>f* complex.

### (C)sAbs generation against cytochrome *b<sub>6f</sub>* reconstituted in nanodiscs

Synthetic antibodies (sAbs) or Fabs were generated against the nanodisc-reconstituted *b<sub>6f</sub>* complex, whose affinity and specificity of binding were tested. After 5 rounds of subtractive selection with empty nanodiscs, to remove non-specific binders and amplification in *E. coli*, initial binding strengths were determined by single point phage ELISA. Clones with an ELISA signal higher than four times the average background level was sequenced.

As we see from bar graphs representing binding strengths of antibody fragments with target *b<sub>6f</sub>* complex, obtained from ELISA (**Figure 2.6.**), there are distinct groups of antibodies showing differential binding strengths for target membrane protein complex. All the clones infected with phages were sent for sequencing and 43 unique Fab particles with differential binding capability were found to bind to cytochrome *b<sub>6f</sub>* complex. Depending on the binding strength between the Fabs and nanodisc- *b<sub>6f</sub>* complex, 6 Fab binders were selected for further rounds of expression and purification (**Table 2.8**).

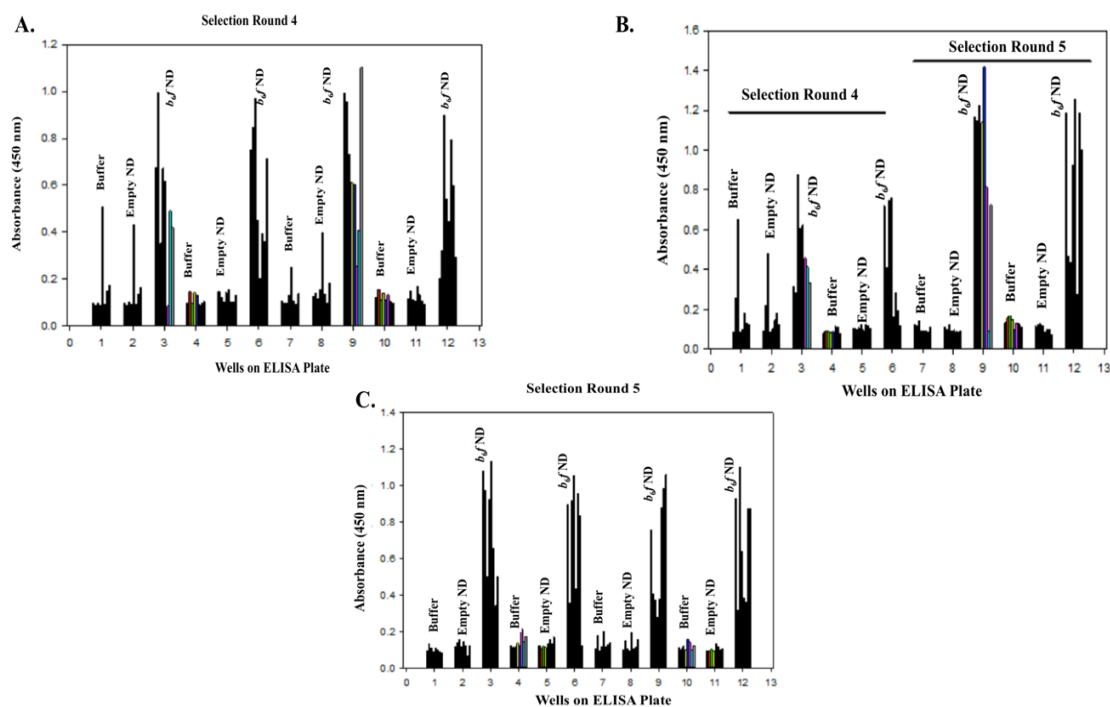


Figure 2.6: Single point protein ELISA of the binding of synthetic antibodies (sAbs) against cytochrome *b<sub>6f</sub>* complex eluted after 4<sup>th</sup> and 5<sup>th</sup> rounds of selection, represented by absorbance reading of quenched TMB ((3,3',5,5'-Tetramethylbenzidine) at 450 nm.

Table 2.8: Amino acid sequences of Fab/sAb heavy chain (HC) and light chains (LC) of binders selected based on their highest binding strength with the cytochrome *b<sub>6f</sub>* complex in nanodiscs, obtained by ELISA.

Fab	HC1 aa	HC2 aa	HC3 aa	LC1 aa
1	ISSSSI	YIYSSSGYTS	SYLWENSWWYVSNGGGL	NYWPGFLI
2	VSYSSI	SISPYSGYTY	QYDFSLWYFTSSDGF	GYYYLI
3	FSSYSI	SISPYSSTTS	QQDDGWERYWRAYWHAAM	SSYYEPI
4	FSSSSI	SISPSSGYTY	YYGYRSHYYEWVWYHGGF	MSVYGLV
5	VYYSSI	SIYSYSGSTY	GSFYTAYLYWWASQSYPAL	TYGSSLV
6	FSYYYYI	SIYSSYSSTTS	GYRDYFWSYKPYGYGSGL	SQYGSTLV

The Fabs were cloned into plasmids PSFV4, expressed in BL21 *E.coli* cells and purified by protein A purification. Complex formation between the cytochrome *b<sub>6f</sub>* complex purified from spinach was attempted with each of the Fabs individually, by incubation at molar ratios of 1:1, 1:2 and 1:4 for 15 min. The cytochrome *b<sub>6f</sub>* complex was subsequently passed through Superdex 200 column and tested for complex formation, based on molecular weight difference. However, no complex formation with the cytochrome complex could be determined for any of the sAbs.

#### 2.4.3 Thermal denaturation/native PAGE

The effect of different lipids on the thermal stability of the *b<sub>6f</sub>* dimeric complex was determined by heating the protein complex in the presence and absence of lipids as described earlier, and subsequently displaying the complex on 4-12% clear native PAGE (**Figure 2.7A**).

The monomer to dimer ratio for each sample on the native gel, was calculated using densitometry analyses in ImageJ software [99, 100]. The monomer to dimer ratio was plotted against temperature for the *b<sub>6f</sub>* complex in UDM, and in the presence of DOPC, DOPG and SQDG (**Figure 2.7B**). All three lipids stabilize the dimeric form, relative to the complex without lipids. SQDG shows a three-fold stabilization of the dimeric complex, which is greater than the effects seen in the presence of DOPG or DOPC.

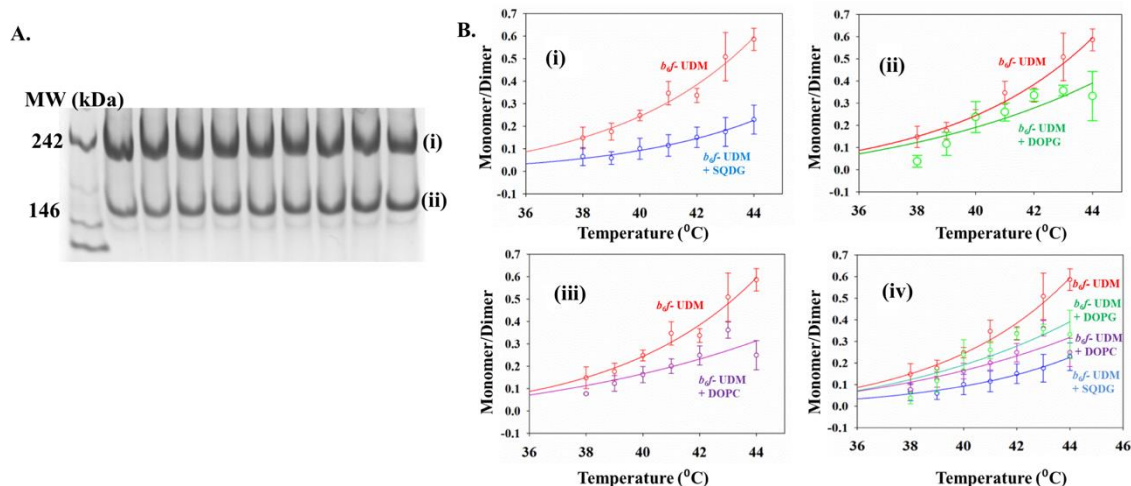


Figure 2.7: Monomerization of the cytochrome *b<sub>6</sub>f* complex as a function of temperature (38 - 44°C). (A) Representative clear native gel image showing (i) dimer (~240 kDa) and (ii) monomer bands (~120 kDa) of cytochrome *b<sub>6</sub>f* complex. (B) Rate of monomerization of the cytochrome complex measured in the absence of lipids (red) and in the presence of (i) SQDG, (ii) DOPG and (iii) DOPC. (iv) Overlay of the monomer: dimer ratio curves in the presence and absence of lipids.

#### 2.4.4 Electron transfer activity

Removal of phospholipids by phospholipase A<sub>2</sub> (PLP) totally inactivated the cytochrome complex (measured as the rate of electron transfer between plastoquinone (PQH<sub>2</sub>) and plastocyanin (PC), within an hour of incubation at room temperature. However, ~65% of the activity could be restored by the addition of phosphatidyl-glycerol (PG) (Figure 2.8) while DOPC and SQDG were unable to restore the activity to the complex.

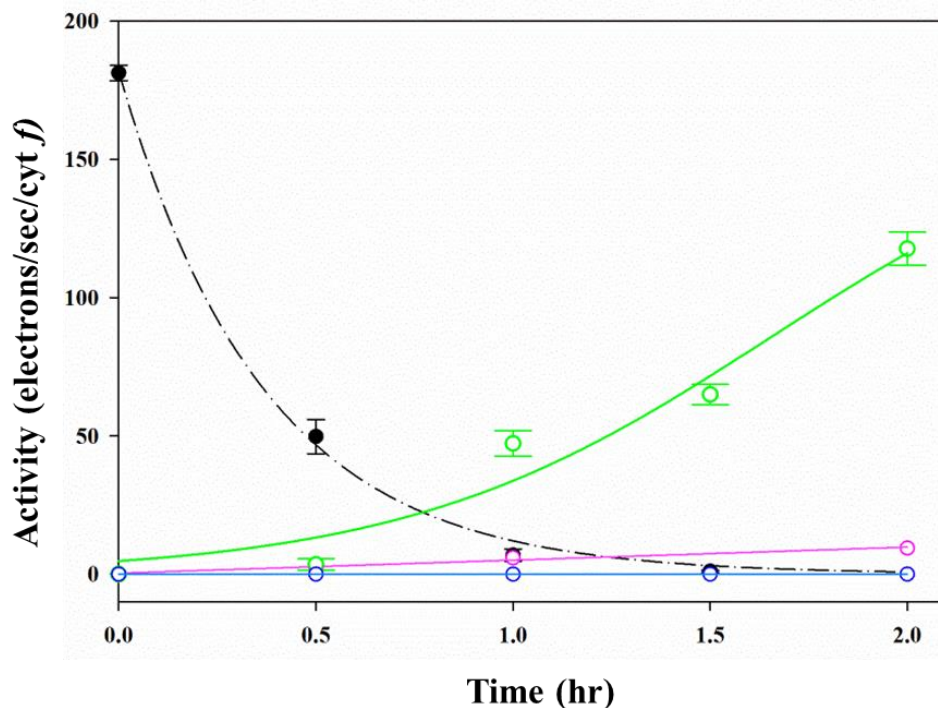


Figure 2.8: Kinetics of the electron transfer activity measured through reduction of plastocyanin at 597 nm, of the cytochrome  $b_6f$  complex, after incubation with phospholipase A<sub>2</sub> (dotted line), and after addition of DOPG (green), SQDG (pink) and DOPC (blue) to the deactivated complex.

#### 2.4.5 Superoxide Production

The  $b_6f$  complex, as a participant in electron transfer which generates low potential redox species, generates reactive oxidative species (ROS), to an extent approximately twice as that of its mitochondrial counterpart, the cytochrome  $bc_1$  complex [102]. The lipid dependence of the generation of ROS by the cytochrome complex is shown (Figure 2.9). Removal of bound phospholipid from the cytochrome complex by phospholipase A<sub>2</sub> leads to a decreased superoxide production, most likely due to loss of electron transport function and thereby decreased formation of plasto-semiquinone [102]. However supplementation of the PLP treated complex with all three lipids individually, restores superoxide formation to a level, comparable to the control (Figure 2.9., Table 2.8).

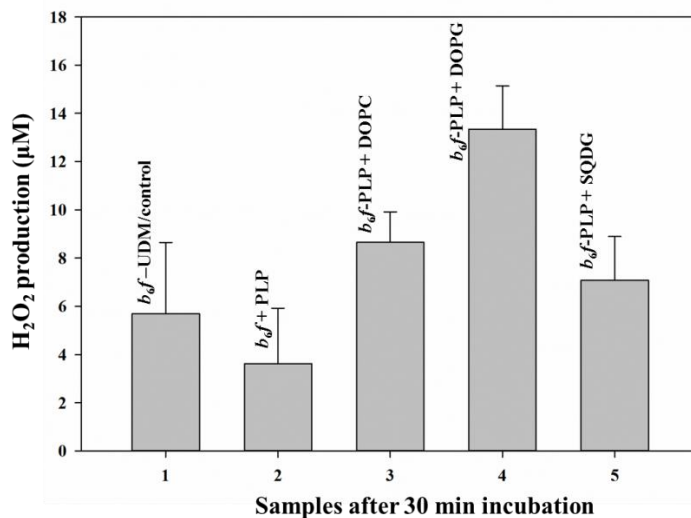


Figure 2.9: Hydrogen peroxide produced as a by-product of the formation of low potential plasto-semiquinone by cytochrome *b<sub>6</sub>f* complex in the presence of DOPC, DOPG and SQDG, and upon treatment with phospholipase A<sub>2</sub> (PLP). Reaction conditions and statistical analyses specified in *Methods*.

Table 2.9: Amount of H<sub>2</sub>O<sub>2</sub> produced by the cytochrome *b<sub>6</sub>f* complex (explained in *Methods*), in the presence and absence of lipids. \**p* < 0.05 (defined in *Methods*)

Cyt <i>b<sub>6</sub>f</i> complex	Mean [H <sub>2</sub> O <sub>2</sub> ] produced (µM)
UDM solubilized	5.7
PLP treated	3.6 ( <i>p</i> =0.041)
PLP treated + DOPC	8.6 ( <i>p</i> =0.011)
PLP treated + DOPG	13.3( <i>p</i> <0.001)
PLP treated + SQDG	7.0 ( <i>p</i> =0.001)

## 2.5 Discussion

The effect of lipids on the structural integrity and the function of the photosynthetic cytochrome *b<sub>6</sub>f* lipoprotein complex is investigated in the present study. DSC was used to study the effect of synthetic lipids (DOPG, DOPC) and the native thylakoid lipid, SQDG, on the thermal stability of the detergent-solubilized cytochrome *b<sub>6</sub>f* complex. Addition of these lipids increases the tertiary structure stability of the complex (**Figure 2.2, Table 2.2**). Deconvolution of the DSC data reveals three distinct domain transitions, which are shifted to higher temperatures in the presence

of lipids (**Figure 2.3**), but whose structural basis is not known. The enthalpy change,  $\Delta H$ , and the melting temperature of the protein ( $T_m$ ) are increased by incorporated lipids (**Table 2.3, Table 2.3**).

All three lipids, DOPG, DOPC and SQDG, stabilize the secondary structure of the protein as well, as shown by the change in molar ellipticity at 222 nm monitored by far-UV CD (**Figure 2.4B, Table 2.5**). However, upon removal of bound phospholipids by phospholipase A<sub>2</sub>, there is no significant decrease in the  $T_m$  of the complex ( **Table 2.6** ). This is in contrast to the effect of phospholipase on other membrane protein complexes like the cytochrome c oxidase [49]. Varying the lipid hydrophobic tails keeping the head groups constant as either PC or PG (**Table 2.5**), differentially stabilized the complex. This result suggests that for the phosphocholines, the stabilization is provided by both the head and tail groups, whereas in case of the anionic lipids phosphatidyl-glycerol, stabilization is provided by an electrostatic interaction arising from the head group.

Nanodiscs are model, detergent-free membrane systems, which enable biophysical and biochemical characterization of membrane proteins in a physiological lipid bilayer environment [106, 107]. Incorporation of integral membrane proteins into nanodiscs formed by various combinations of lipids has been shown to provide a more native membrane environment than detergent micelles [107]. Similarly, phospholipid bicelles can preserve the integrity of integral membrane proteins by providing a native-like membrane environment [108-110]. The nanodiscs and bicelles comprised of synthetic lipids stabilize the secondary structure of the complex significantly (**Figure 2.5, Table 2.7**) which implies that the hydrophobic environment, irrespective of the polar head groups, is sufficient to stabilize the integrity of the cytochrome complex.

In the present studies, an attempt was made in these studies to encapsulate the *b<sub>6f</sub>* complex in nanodiscs and generate selective sAbs, for stabilization of different conformations. Nanodisc based phage sorting offers some key advantages [101]: (i) nanodiscs in general provide structural stabilization in membrane protein complexes (ii) the reconstitution of membrane proteins in nanodiscs makes the phage display sorting process modular, that is they can be tailored for different conditions and systems [101].

6 distinct conformationally selective Fabs or sAbs were generated from the phage library, against the cytochrome *b<sub>6f</sub>* complex encapsulated in nanodiscs (DOPG: DOPC=1:3, MSP2N2) was successful. However, the purified Fabs showed no binding to the cytochrome *b<sub>6f</sub>* complex, purified from spinach and solubilized in 0.04% UDM. An explanation for the lack of binding of

any of the Fab particles can be made based on structural stabilization studies on nanodisc reconstituted cytochrome *b<sub>6</sub>f* complex (**Figure 2.5, Table 2.7**). Such a significant structural stabilization in nanodiscs implies that the conformational states that were selected for by the sAbs or Fab particles, were absent in the detergent solubilized state. Detergent sensitivity of Fab binding is attributed to two major factors [101]: (i) availability of the epitopes for the Fabs maybe are modulated by the micelle size or chemical makeup of the detergent used for solubilization, and (ii) the hydrophobic environment around the membrane protein affects the local structural epitope conformations [58].

From our results, it can thus be inferred that UDM provides a hydrophobic environment to the cytochrome complex, which is far from native conditions preferred for the cytochrome complex. Decrease or loss of affinity of the sAbs for the cytochrome complex in going from the nanodisc to detergent solubilized state, implies that the epitope assumed a non-native conformation in the UDM-provided hydrophobic environment since conformations taken up in nanodisc environment mimics native states [101].

For future studies, different detergents like  $\beta$ -DDM and digitonin will be used for solubilization of the *b<sub>6</sub>f* complex, and subsequent binding studies will be done with the purified Fab particles. In addition, lipids DOPG, DOPC and SQDG will be added to detergent solubilized *b<sub>6</sub>f* sample, to provide stabilization (**Figure 2.4**). Previous studies have shown that addition of small amounts of lipid can restore sAb affinity for the membrane protein complexes solubilized in detergents [101]. DOPC and DOPG are of particular interest since ordered crystal packing were obtained for the *b<sub>6</sub>f* complex purified from cyanobacteria [26-28], only when the lipids were added back to the protein complex. If the above strategies fail, the selection step for sAbs against *b<sub>6</sub>f* encapsulated in nanodiscs should be repeated with detergent solubilized complex.

The rate of monomerization of the cytochrome *b<sub>6</sub>f* complex with increasing temperature, was studied by clear-native gel electrophoresis, followed by densitometry analyses of the ratio of monomer to dimer bands.

SQDG reduces the rate of monomerization of the cytochrome complex three-fold, when compared to the delipidated complex (**Figure 2.7B**). A structural basis for the involvement of SQDG in dimer stabilization of the complex, based on the 2.5 Å structure [28], may be due to its unique, conserved binding site (**Figure 2.10**).

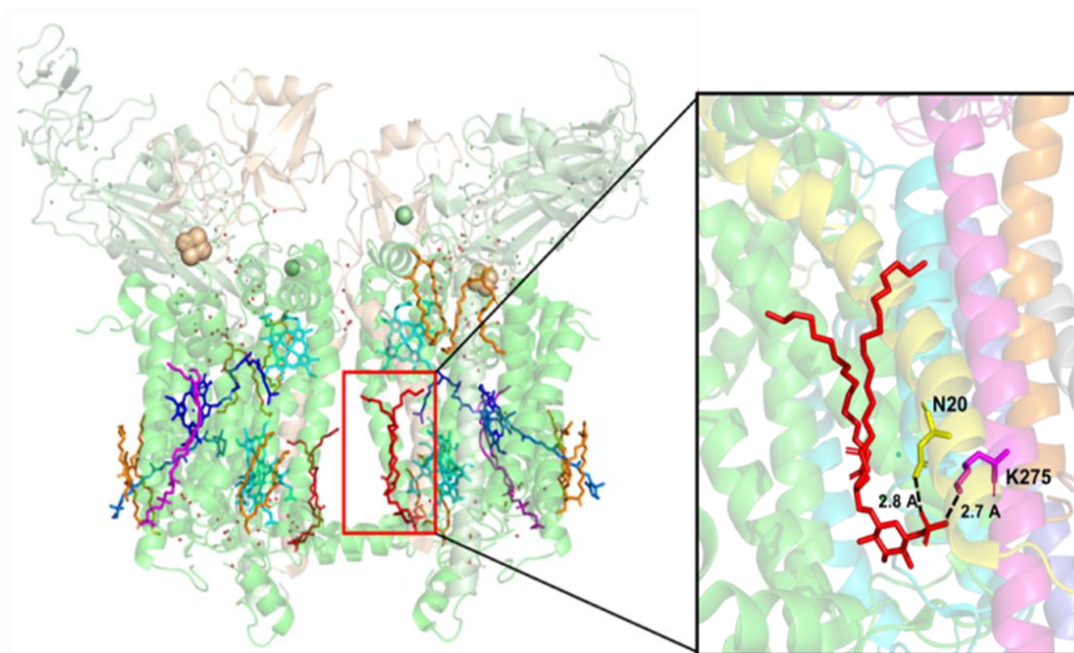


Figure 2.10.:View along the membrane plane of the cytochrome *b<sub>6</sub>f* complex (PDB: 4OGQ). Highlighted in red is the anionic lipid SQDG interacting with residue K275 of the Rieske (yellow) and N20 of the cyt *f* subunit (pink).

The SQDG bonds with a highly conserved arginine residue (N20) on the Rieske iron-sulfur subunit and a lysine residue (K275) on the cytochrome *f* subunit [28, 111]. Deletion of the conserved arginine, N20 residue has been shown to be deleterious for the assembly of the cytochrome *b<sub>6</sub>f* complex [111]. The unique domain-swapped Rieske subunit of the cytochrome complex, is considered essential for dimerization of the *b<sub>6</sub>f* [112]. Thus, by stabilizing the essential domain-swapped Rieske subunit, SQDG contributes to the dimeric stability of the complex.

The presence of the phospholipids, DOPG and DOPC, in the complex shows an approximately 2-fold reduction in the rate of monomerization of the cytochrome *b<sub>6</sub>f* complex as a function of temperature (**Figure 2.7B**).

Anionic lipids like PG and cardiolipin have been found to be essential for the activity of many membrane protein complexes such as photosystem II [113-115], respiratory complex I [115] and the respiratory complex III [116]. PG has been shown to be required for the photosynthetic activity of the photosystem II (PSII) complex in cyanobacteria [113, 114] and plants [115].

In the present study it is shown that the removal of bound phospholipids completely deactivates the cytochrome *b<sub>6</sub>f* complex (**Figure 2.8**). Subsequent addition of the anionic lipid

DOPG restores approximately 2/3 of the activity within 2 hours of incubation at room temperature. The native anionic lipid, SQDG, in comparison, is unable to reactivate the cytochrome complex, as is the neutral lipid DOPC (Figure 2.8). From this observation, it is inferred that the anionic phospholipid head group is essential for the activity of the *b<sub>6</sub>f* complex. This result is consistent with the observation that in the homologous cytochrome *bc<sub>1</sub>* complex, the anionic lipid cardiolipin restored most of the activity in phospholipase treated complex [66, 116]. Furthermore, (i) the oxygen-evolving photosynthetic activity of the cyanobacterium *Synechocystis sp.* PCC 6803 has been found to be dependent on the hydrophobic chain length of the PG lipid moieties [117]; (ii) the unsaturated di-oleoyl PG restored the photosynthetic activity in photo-inhibited cyanobacterium much more efficiently than the saturated counterparts (dimyristoyl-PG, dipalmitoyl-PG and distearoyl-PG) [117]. In this study, it was found that palmitoyl-oleoyl-PG (POPG) could not restore the activity of the *b<sub>6</sub>f* complex (data not shown).

A structure-based explanation for the effect of PG on the activity of the *b<sub>6</sub>f* complex can be inferred based on putative PG- binding sites, as obtained from the 2.5Å crystal structure [28] (**Figure 2.11A**, PDB 4OGQ): (i) There are two phospholipid binding sites, PG1 and PG2 (**Figure 2.11B**), near the quinone portal lined by the C and F- helices, which connect the intermonomer cavity and the heme *b<sub>p</sub>* [3]. By stabilizing the portal, the PG facilitates the passage of plastoquinone efficiently for reduction of the heme *b<sub>p</sub>*. (ii) A third PG binding site, PG 3 (**Figure 2.11C**) stabilizes the hinge-region of the Rieske iron-sulfur protein (ISP).

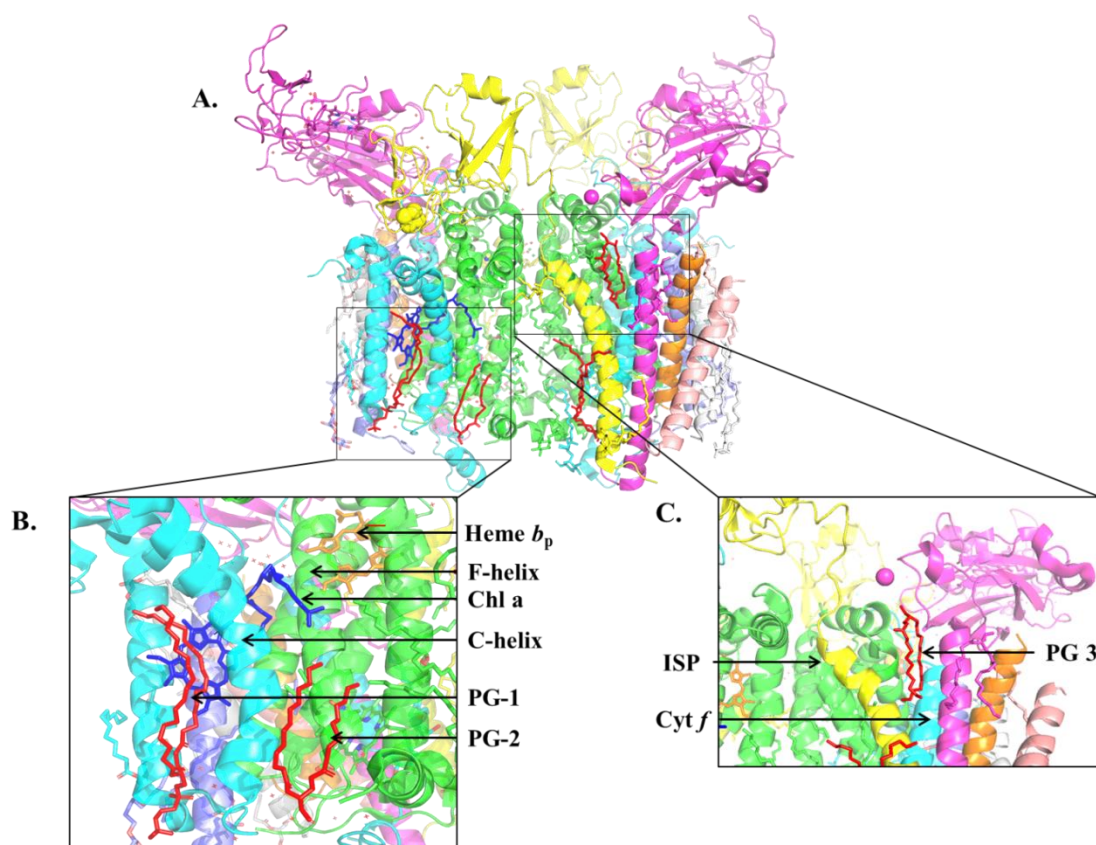


Figure 2.11: Structural basis for the stabilization of activity of  $b_6f$  by phosphatidyl-glycerol. (A) View along the membrane plane of the cytochrome  $b_6f$  complex (PDB: 4OGQ). (B) Magnified view of the phospholipid binding sites (PG1 and PG2, red) lining the quinone portal connecting the intermonomer cavity and heme  $b_p$ , lined by C (blue) and F (green) helices. (C) Magnified view of a phospholipid binding site (PG 3, red) near the hinge region of the Rieske iron-sulfur protein (ISP, yellow).

In the homologous cytochrome  $bc_1$  complex, the presence of a similar phospholipid binding niche to support the large-scale movement of the soluble domain of ISP for electron transport [42, 118] has been documented. Although any significant movement of the ISP soluble domain, has not been observed in the  $b_6f$  complex [34], the presence of the conserved phospholipid binding site, serves as an interesting candidate for future investigation.

The presence of the phospholipids, DOPC and DOPG, results in an increased production of superoxide by the cytochrome complex (**Figure 2.9, Table 2.9**). The effect of a hydrophobic lipid bilayer, and effect of negatively charged detergents on the superoxide production by cytochrome  $bc_1$  complex, has been noted previously [119] where negatively charged detergents, like sodium cholate and deoxycholate promoted superoxide production more than the neutral and

cationic counterparts. The negative charge of the detergents was implicated in facilitating deprotonation of the 1-hydroxy group of quinols. Similarly, the anionic phospholipid DOPG increases the superoxide production by the cytochrome *b<sub>6</sub>f* complex.

In conclusion, the presence of hydrophobic acyl chains of lipids increases the structural stability of the *b<sub>6</sub>f* complex. Individual functions of the native, thylakoid anionic lipids have been identified. While the sulfolipid, SQDG, increases the dimeric stability of the *b<sub>6</sub>f* complex, PG is required for activity. The consequences of endogenous lipid on the directionality of electron transfer through the low potential hemes in the *b<sub>6</sub>f* complex have been discussed previously [65, 120]. Thus, the relation between the structure and function of a hetero-oligomeric lipoprotein complex such as the cytochrome *b<sub>6</sub>f* complex, must consider not only the protein, but also the internal lipid environment.

## CHAPTER 3. PATHWAYS OF TRANSMEMBRANE ELECTRON TRANSFER IN CYTOCHROME *bc* COMPLEXES: DIELECTRIC HETEROGENEITY AND INTER-HEME COULOMBIC INTERACTIONS

(This chapter was published as Bhaduri et.al, *J Phys Chem B*, 2017)

### 3.1 Summary

The intra-membrane cytochrome *bc<sub>1</sub>* complex of the photosynthetic bacterium, *Rhodobacter capsulatus*, and the cytochrome *b<sub>6</sub>f* complex which functions in oxygenic photosynthesis, utilize two pairs of b-hemes in a symmetric dimer to accomplish proton-coupled electron transfer. The trans-membrane electron transfer pathway in each complex was identified through novel use of heme Soret band excitonic circular dichroism spectra, for which the responsible heme-heme interactions were determined from crystal structures. Kinetics of heme reduction and circular dichroism amplitude change were measured simultaneously. For *bc<sub>1</sub>*, in which the redox potentials of the trans-membrane heme pair are separated by 160 mV, heme reduction occurs preferentially to the higher potential inter-monomer heme pair on the electro-negative (n) side of the complex. This contrasts with the *b<sub>6</sub>f* complex where the redox potential difference between trans-membrane intra-monomer p- and n-side hemes is substantially smaller, and the n-p pair is preferentially reduced. Limits on the dielectric constant between intra-monomer hemes were calculated from the inter-heme distance and the redox potential difference,  $\Delta E_m$ . The difference in preferred reduction pathway is a consequence of the larger  $\Delta E_m$  between n- and p-side hemes in *bc<sub>1</sub>*, which favors reduction of n-side hemes, and cannot be offset by decreased repulsive Coulomb interactions between intra-monomer hemes.

### 3.2 Introduction

An understanding of the forces that guide the assembly and function of an intra-membrane protein complexes requires knowledge of the internal distribution of chemical polarity, which, for charge-transfer proteins, is expressed in the dielectric constant [65, 121-125]. The intra-membrane domain of integral membrane proteins has been traditionally described as a uniformly hydrophobic, non-polar, low dielectric medium. However, it is inferred that the interior polarity of membrane

proteins can be heterogeneous based on the presence of intra-protein lipids,[28, 60] and water chains[126],[127] or pockets in solute transport[128] or membrane proteins [58], including the bacterial, mitochondrial cytochrome  $bc_1$  [129],[130],[130],[48],[131] and photosynthetic  $b_{6f}$  [28] electron transfer complexes. An initial analysis of this problem in the intra-membrane cytochrome system was carried out previously with the cytochrome  $b_{6f}$  complex, for which a heterogeneous distribution of dielectric constants in the inter-heme network was inferred [65]. A non-uniform distribution of dielectric constants has been inferred previously in photosynthetic reaction center membrane protein complexes from bacteria [122] and cyanobacteria [132]. The difference in amino acid polarity in the two branches of the reaction center complex [122, 123, 125, 132] can explain the preferential use of one monomer of the dimeric complex for primary trans-membrane charge separation. In the present study, the dependence of the inter-heme dielectric constant was analyzed in the trans-membrane cytochrome  $bc_1$  complex of the photosynthetic bacterium, *Rhodobacter capsulatus* (**Figure 3.1**), in which the redox potential difference between the trans-membrane  $b$ -hemes is substantially larger than in the  $b_{6f}$  complex[133].

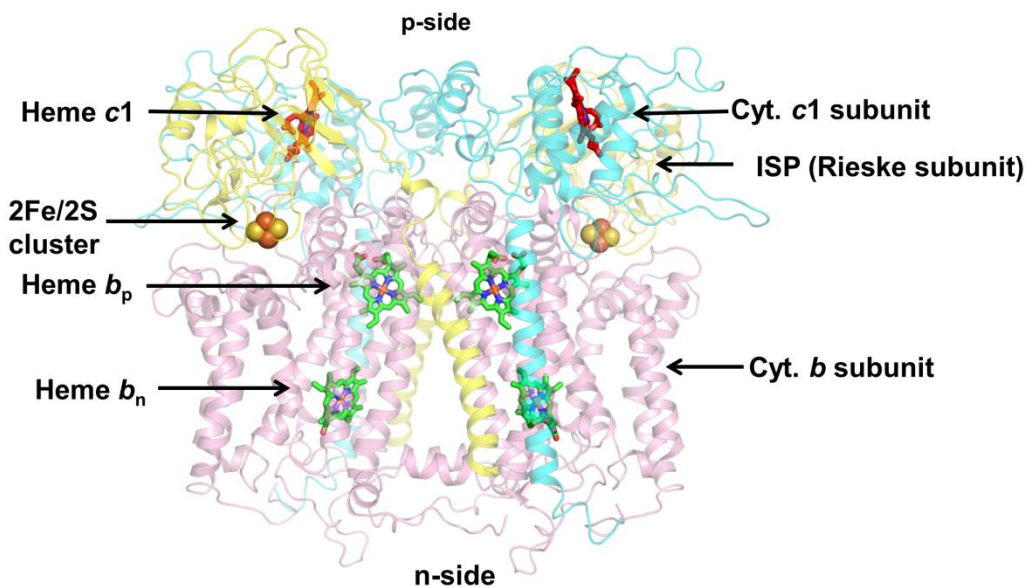


Figure 3.1: Description of crystal structure of the trans-membrane cytochrome  $bc_1$  complex from *Rb. capsulatus* (PDB 1ZRT), showing the protein subunits, redox prosthetic groups, and trans-membrane helices.

The four hemes *b* of a conserved hydrophobic core of a dimer are universally present in all *bc* complexes. In this heme network, in addition to the intra-monomer transfer between heme  $b_p$  and  $b_n$ , an inter-monomer electron transfer between two hemes  $b_p$  has been inferred [134],[135]. The existence of excitonic circular dichroism (CD) spectra associated with *b*-heme interactions in the hetero-oligomeric mitochondrial *bc*<sub>1</sub> complex [136] and *b<sub>6</sub>f* complex [65] describe additional structural aspects that determine the preferential pathways of electron transfer. The structure-function analysis in the present study employs the cytochrome *bc*<sub>1</sub> complex from the purple photosynthetic bacterium, *Rhodobacter capsulatus*, for which there is a difference of approximately 160 mV in redox potentials between the two *b* hemes [133] on the opposite sides of the complex and the membrane. In the present study, it is concluded that the preferential pathway of heme reduction in the bacterial *bc*<sub>1</sub> complex is different from that reached previously for the *b<sub>6</sub>f* complex, and this pathway depends on the dielectric heterogeneity within the complexes [65].

### 3.3 Materials and Methods

#### 3.3.1 Isolation/Purification of Cytochrome *bc*<sub>1</sub> Complex

The complex was isolated from the purple photosynthetic bacterium *Rhodobacter capsulatus* grown in the dark under semi-aerobic conditions [137]. A two-day old culture was collected, and the cells disrupted using a French Press followed by centrifugation. The remaining supernatant containing chromatophores was separated in the ultracentrifuge, and the sediment re-suspended in Tris-HCl, pH 8.0, 20% glycerol. The chromatophores were solubilized with 0.04% n-dodecyl- $\beta$ -D-maltoside (DDM) for 1 h at 0°C followed by ultracentrifugation. The supernatant was applied to a DEAE-BioGel A column and washed with 50 mM Tris buffer, 20% glycerol, 165 mM NaCl, and 0.01 % DDM. The complex was eluted using a 165 mM-450 mM NaCl gradient and concentrated using a micro-concentrator. Purity of the resulting complex was checked by SDS-PAGE electrophoresis [138] (**Figure 3.2A**), and the concentration and activity of the *bc*<sub>1</sub> complex measured as previously described [139], [140]. Purified *bc*<sub>1</sub> complex was analyzed by Clear Native PAGE (CN-PAGE), using a 4-12% gradient gel [141] (Figure 3.2 B).

### 3.3.2 Absorbance Difference Spectra

The absorbance (OD) difference spectra were measured with a Cary 4000 spectrophotometer. Complete oxidization of the  $bc_1$  complex utilized potassium ferricyanide (30  $\mu\text{M}$ ), and selective reduction of *Rb. capsulatus* heme  $c_1$  ( $E_{m7} = +0.32$  V) [138] by sodium ascorbate (0.5 mM). Reduction of the two lower potential  $b$  hemes on the electrochemically positive (p) and negative (n) sides of the membrane, labeled  $b_p$  and  $b_n$ , was achieved by addition of an aliquot of 1 M dithionite, prepared freshly in a degassed solution, in 0.1M Tris-HCl, pH 8.0, with a final concentration of 5 mM.

### 3.3.3 Electron Transport Activity

A specific activity of  $156 \pm 5$   $\mu\text{mol}$  cytochrome  $c$  reduced/  $\mu\text{mol}$  heme  $c_1$  per sec was measured with 10 nM cytochrome  $bc_1$  complex in 50 mM Tris-HCl, pH 8.0, 100 mM NaCl, using 20  $\mu\text{M}$  decyl-benzoquinol (2,3-dimethoxy-5-methyl-6-decyl-1,4- benzohydroquinone), and 20  $\mu\text{M}$  cytochrome  $c$ , respectively, as electron donor and acceptor.

### 3.3.4 Simultaneous Measurement of Absorbance and Circular Dichroism Spectra of Hemes $b_n$ and $b_p$

Circular dichroism and absorbance spectra were measured simultaneously in the 420-440 nm spectral region, employing a spectropolarimeter [“Chirascan” (Applied Photophysics, Ltd., U.K)], half band-width of 1 nm, step size of 0.5 nm, and 0.1 s integration time. Measurements were carried out in a stirred cuvette with a 1 cm path length which was purged with  $\text{N}_2$  during dithionite addition and measurements of spectra. Samples were diluted into deoxygenated buffer containing 30 mM Tris-HCl, pH 7.5, 50 mM NaCl, 0.1mM EDTA, and 0.04% (w/v)  $\beta$ -D-dodecyl-maltoside (DDM). After addition of dithionite, consecutive spectra were taken at 12-14 s intervals.

### 3.3.5 Simulation of CD Spectra: Interaction Between Different Heme Pairs

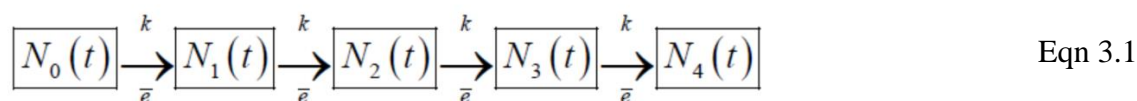
Contributions of different heme pairs in the four-heme complex to the CD spectra were calculated using (1) X-ray structure data obtained at 3.5  $\text{\AA}$  resolution for the  $bc_1$  complex from *Rb. capsulatus* (PDB 1ZRT [130]), and (2) the dependence of the heme-heme dipole-dipole interaction energy,  $V_{12}$ , on (a) the inverse third power of the interheme Fe-Fe distance and (b) the dihedral angle,  $\Theta$ , between the heme planes, defined by the function,  $\sin 2\Theta$ , as described previously [28, 65]. The interaction between two hemes results in a splitting of the excited state energy level into

two levels  $E^+$  and  $E^-$ , separated by the energy,  $2V_{12}$ . The rotational strength of the excitonically separated transitions was derived from determination of heme-heme interactions based on the x-ray crystal structure (PDB 1ZRT). The  $B_x$  and  $B_y$  transitions of the reduced  $b$ -hemes are directed along the orthogonal axes connecting the pyrrole ring nitrogens  $N_A-N_C$  and  $N_B-N_D$ . Fe-Fe and edge-edge distances between the pyrrole rings (**Figure 3.3**) were derived from the crystallographic structure (PDB 1ZRT). The corresponding distances in the cytochrome  $b_6f$  complex are presented for comparison (**Table 3.1**).

The relative amplitude of the interacting X-X, X-Y, and Y-Y transitions in the CD spectra were calculated separately and combined [65]. The absorbance spectrum of each  $b$ -heme was assumed to be a Gaussian function with a half-bandwidth of 10 nm. The program GEOMCALC (CCP4) [142], which approximates heme as a planar structure, was used to determine the inter-planar angle between hemes.

### 3.3.6 Simulation of kinetics of absorbance and circular dichroism changes resulting from addition of reductant (By Prof. Sergei Savikhin, Department of Physics and Astronomy, Purdue University)

Due to lack of knowledge regarding possible rate and other effects associated with efficiency of the protein reduction by the reductant, the proposed kinetic equation defines the simplest model that describes the reduction of the four heme moieties in cytochrome  $bc_1$  complex. Presently, there is no conceptual basis for a more complicated model. Hence, first order linear kinetics has been chosen. It has been shown that the electron transfer in cytochrome-like complexes occurs on ultrafast-to-fast time scales [143, 144]. Hence each reduction state of the protein is in thermodynamic equilibrium. The kinetics of the reduction of the cytochrome  $bc_1$  complex by a one electron donor are represented using the following scheme, where  $N_i$  represents a thermodynamic equilibrium system with  $i$  hemes reduced:



where  $N_i(t)$  corresponds to the population of the protein dimer complexes containing  $i$  electrons ( $i = 1 \dots 4$ ), and  $k$  is the rate of electron transfer from the donor (dithionite) to the protein complex. The kinetics can be described with the system of first order differential equations:

$$\left\{ \begin{array}{l} dN_0(t)/dt = -kN_0(t) \\ dN_1(t)/dt = kN_0(t) - kN_1(t) \\ dN_2(t)/dt = kN_1(t) - kN_2(t) \\ dN_3(t)/dt = kN_2(t) - kN_3(t) \\ dN_4(t)/dt = kN_3(t) \\ N_0(0) = 1, \quad N_1(0) = N_2(0) = N_3(0) = N_4(0) = 0 \end{array} \right. \quad \text{Eqn. 3.2}$$

The analytical solution of the system of equations, as it applies to the  $bc_1$  complex, has been discussed previously [65]

The kinetics of the CD signal for the two models (“ $n$ - $n$ ” and “ $n$ - $p$ ”, Figure 4.6. A, B) are then expressed as:

$$\begin{aligned} CD_{"n-n"}(t) &= d_{n_1-n_1}N_2(t) + (d_{n_1-n_1} + d_{n_1-p_1} + d_{n_1-p_2})N_3(t) + N_4(t) \\ CD_{"n-p"}(t) &= d_{n_1-n_1}N_2(t) + (d_{n_1-n_1} + d_{n_1-p_1} + d_{n_1-p_2})N_3(t) + N_4(t) \end{aligned} \quad \text{Eqn. 3.3}$$

The coefficients “ $d$ ” represents the CD signal intensity originating from different reduced  $b$ -heme pairs within the  $bc_1$  dimer, as denoted by the subscript (**Table 3.1**).

The result of the simulations for  $k = 0.0053 \text{ s}^{-1}$ , the rate constant of the slower component in the experimental data, was fitted with the data in Figure 3C. The CD signal is expected to be significantly delayed with respect to the absorbance signal in the “ $n$ - $n$ ” model, because it takes three electron transfer events to form the first reduced  $b_{n_1}$ - $b_{p_1}$  pair that is the main source of the CD signal (**Figure 3C**). Indeed, the OD reaches  $\sim 65\%$  of its maximum value in 50 s, while the same increase in the CD signal occurs in  $\sim 200$ s. The experimental profiles were fit (**Figure 3.4 C**) with the assumption that there are two pools of the complexes that differ only in the reduction rate.

### 3.3.7 Model for Kinetics of Reductant-Induced Amplitude Changes of Exciton Circular Dichroism and Absorbance.

The CD signal kinetics,  $CD(t)$ , depend on the order in which the hemes are reduced, because reduction of the intra-monomer hemes  $b_n$  and  $b_p$  is required to generate CD signal of the largest amplitude (Figure 3.5). The CD signal kinetics for different models can be calculated according to the population of different pairs of  $b$ -hemes and their relative CD amplitudes (**Table**

**3.1, Figure 3.5).** The spectra for the cytochrome *b<sub>6</sub>f* complex, and a model of the four states resulting from transfer of 1-4 electrons in simulations of the kinetics are described elsewhere in detail [65]. The net absorbance function, at any given time *t*,  $OD(t)$ , reports the total population of the reduced *b*-hemes, i.e.,  $OD(t) = [N_1(t) + 2N_2(t) + 3N_3(t) + 4N_4(t)]$ , where *N* is the number of complexes reduced by 1, 2, 3, or 4 electrons, and does not depend on the order in which the hemes are reduced.

### 3.4 Results

#### 3.4.1 Characterization of Purified Cytochrome *bc<sub>1</sub>* Complex: Heme Difference Spectra

Predominantly dimeric cytochrome *bc<sub>1</sub>* complex was prepared as described in *Materials and Methods*, and the subunit composition defined by SDS-PAGE analysis (**Figure 3.2A**). The native intact dimeric character of the isolated complex was established by (i) clear native gel electrophoresis analysis (**Figure 3.2B**), and (ii) the electron transfer rate, 156 electrons-cyt *c<sub>1</sub>*<sup>-1</sup>s<sup>-1</sup> from the electron donor decyl-benzoquinol to the acceptor, oxidized cytochrome *c*.

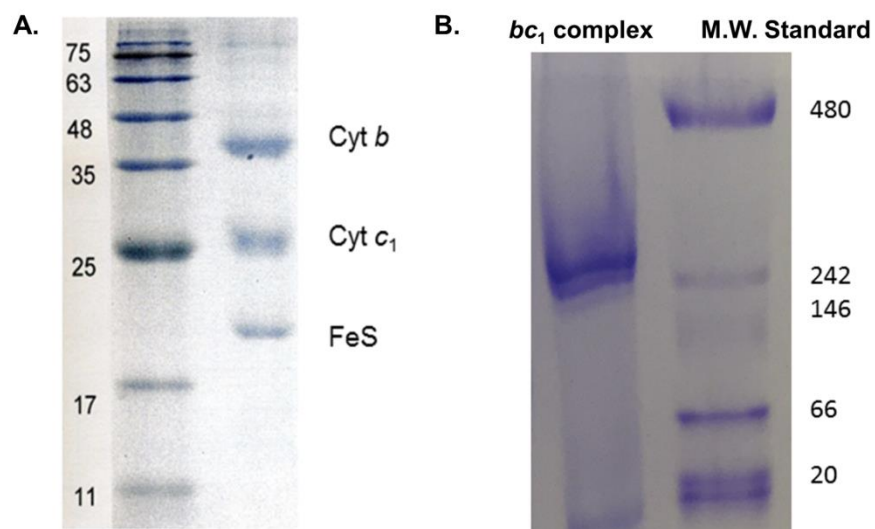


Figure 3.2: Gel analyses of cytochrome *bc<sub>1</sub>* complex purified from *Rhodobacter capsulatus*. (A) SDS PAGE showing the presence of three distinct subunits and (B) clear- native-PAGE showing the presence of the intact dimeric complex.

#### 3.4.2 Chemical Reduction of Hemes in the *bc<sub>1</sub>* Complex

After reduction of cytochrome *c<sub>1</sub>* ( $E_m = + 320$  mV) [138], displaying an absorbance peak at 551 nm (Figure 3.3, spectrum in red), by sodium ascorbate, the two *b*-hemes with an absorbance

maximum at 559-560 nm (spectrum in green) in the dimeric  $bc_1$  complex were completely reduced under anaerobic conditions by dithionite (ca. 2 mM) at room temperature (23°C) and pH 7.5 (**Figure 3.3**). An extinction coefficient of  $2 \times 10^4 \text{ M}^{-1}\text{cm}^{-1}$  for hemes  $c_1$  and  $b$ , determined for the higher potential heme  $b$ , was used to determine the heme stoichiometry [145].

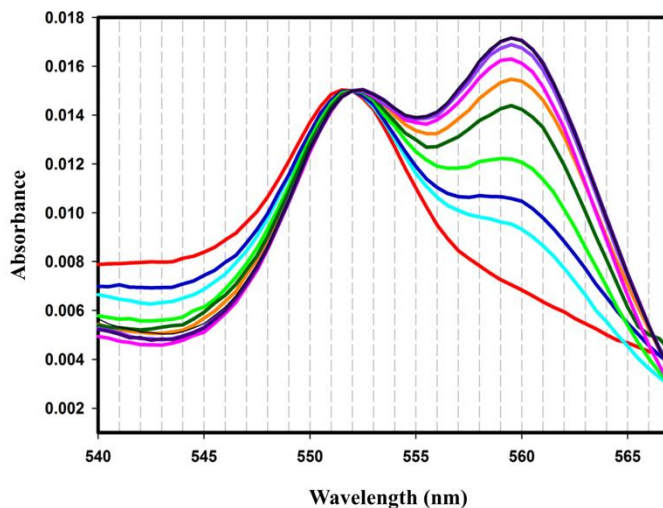


Figure 3.3: Reduced minus oxidized absorbance difference spectra of the *Rb. capsulatus* cytochrome  $bc_1$  complex in 30 mM Tris-HCl, pH 7.5, 50 mM NaCl, 0.1mM EDTA, 0.04% DDM;  $\alpha$ -band absorbance difference spectra, with maxima at 551 nm and 560 nm, respectively, initially oxidized by ferricyanide ( $\text{FeCN}$ , 30  $\mu\text{M}$ ), and subsequently reduced by sodium ascorbate (0.5 mM), yielding an absorbance difference spectrum (in red) with a peak at 551 nm. Subsequently, the sample was reduced with sodium dithionite (ca. 2 mM) yielding an absorbance maximum in the difference spectrum at 559 - 560 nm (green). Concentration of cytochrome complex, 30  $\mu\text{M}$ . The difference spectra were taken at time points 12s (cyan), 48s (dark blue), 96s (light green), 132s (dark green), 168s (orange), 216 s (pink), 276 s (purple), and 324s (black), after addition of dithionite.

### 3.4.3. Heme-heme Excitonic Interactions

Split CD spectra in the Soret band region of cytochrome  $b$  complexes arise from excitonic heme-heme interactions [65, 136]. The magnitude of the excitonic interaction responsible for the split CD spectrum is similar to that previously determined for the  $b_6f$  complex [65], as judged by the 8 nm separation of the peaks of the short wavelength positive and long wavelength negative

peaks at 426 and 434 nm, with the node of the split CD spectrum (

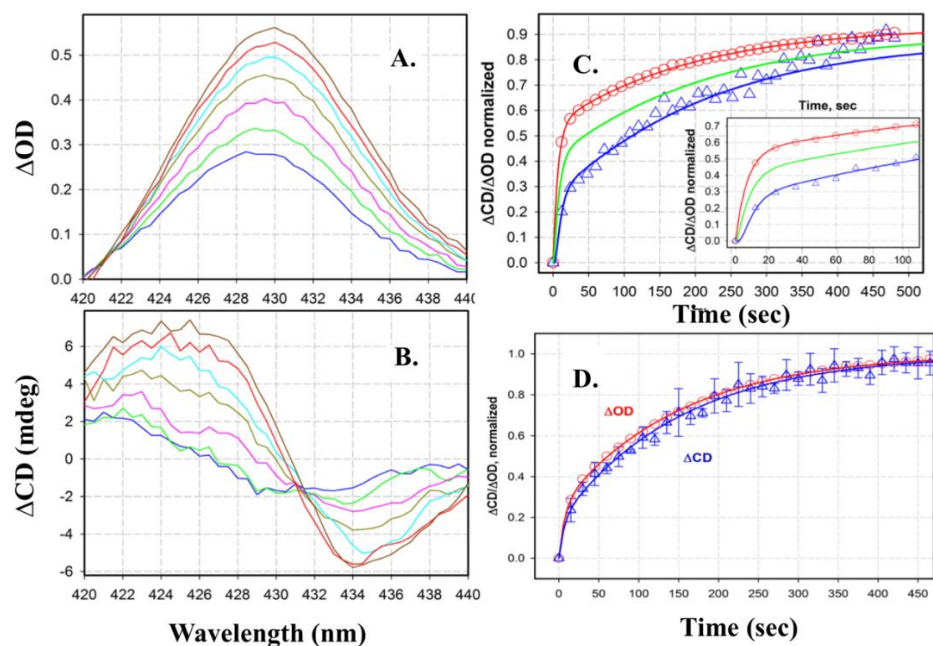


Figure 3.43.4 B) centered at the peak of the absorbance spectrum (Figure 3.4 A). Similar to previous CD studies on the cytochrome *b<sub>6</sub>f* [65] and *b<sub>c</sub>1* [136] complexes, some asymmetry is seen between the positive and negative lobes of the split CD spectra. This asymmetry is more pronounced in the bacterial *b<sub>c</sub>1* complex studied here. It arises from the presence of relatively small amplitude absorbance and CD peaks at 415 – 420 nm in the bacterial *b<sub>c</sub>1* complex, previously observed in the CD spectra of the mitochondrial *b<sub>c</sub>1* complex [136]. As shown in the study on the mitochondrial complex, the contribution of these components to the amplitude of the long wavelength negative lobe of the CD spectrum centered at 434 nm is considered negligible. Hence, in the present work, the change in the area under the negative lobe of the CD spectrum is used to correlate the time course of the change in heme-heme interaction with the reduction of *b*-hemes by dithionite.

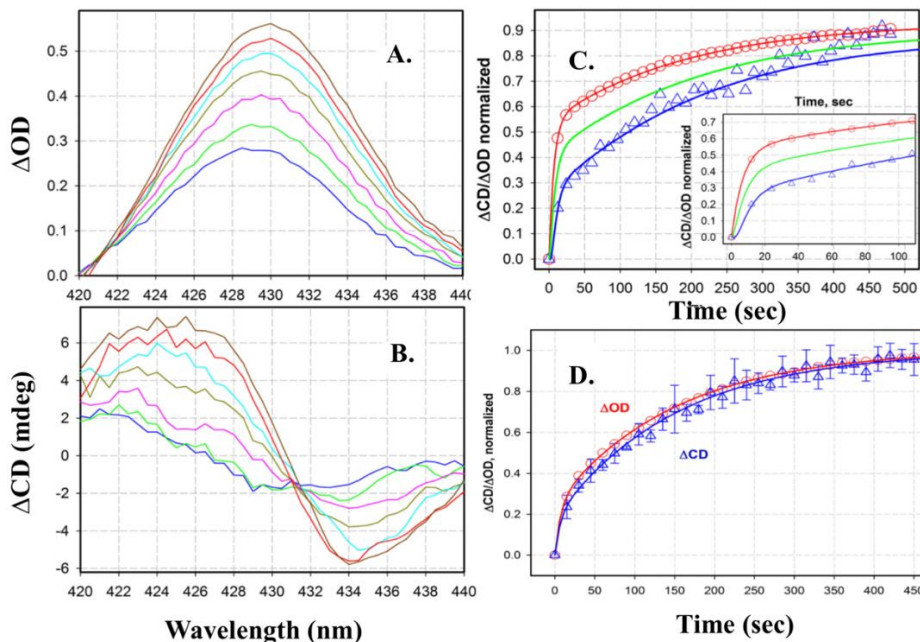


Figure 3.4.: Soret band absorbance and CD spectra; kinetics of absorbance and CD changes. Simultaneous measurement of the kinetics of reduction (dithionite concentration, 5 mM) and formation of the Soret band excitonically split CD spectrum of hemes,  $b_p$  and  $b_n$ , on the electrochemically positive, p, and negative, n, sides of the complex. Difference (Dith-Asc) absorbance (OD) (A) and CD (B) spectra are shown, which were measured 12 s (blue), 48 s (green), 96 s (pink), 168 s (gold), 264 s (cyan), 408 s (red), and 588 s (brown) after the addition of dithionite. (C) Kinetics of increase of OD and split CD (negative lobe) signals associated with dithionite reduction of the  $bcI$  complex; absolute values of areas of absorbance peak in spectral range 424-436 nm (circles) and split CD peaks in range 432-440 nm (triangles) are shown. OD was fit using a double exponential function with the parameters:  $t_1$ ,  $0.13 \pm 0.02 \text{ s}^{-1}$  ( $A_1$ ,  $0.60 \pm 0.02$ ) and  $t_2$ ,  $5.0 \times 10^{-3} \pm 0.4 \times 10^{-3} \text{ s}^{-1}$  ( $A_2$ ,  $0.42 \pm 0.01$ ) for the change in optical density (OD, red line). Prediction of the kinetics of the split CD signal, with given OD signal, change according to “nn” (blue line) and “np” (green line) models is described in Figure 3.6. (D) Kinetics of the increase of OD and split CD signals associated with dithionite reduction of  $b_{cf}$  complex<sup>2</sup> were obtained as described for the  $bcI$  complex (panel C). Data were fit using a double exponential formula:  $t_1$ ,  $0.14 \pm 0.02 \text{ s}^{-1}$  ( $A_1$ ,  $0.25 \pm 0.01$ ) and  $t_2$ ,  $6.6 \times 10^{-3} \pm 0.1 \times 10^{-3} \text{ s}^{-1}$  ( $A_2$ ,  $0.75 \pm 0.01$ ) for OD (red line); the simulation predicting the kinetics profile with give OD kinetics for CD (blue line).

### 3.4.3 Simultaneous Measurement of Circular Dichroism and Heme Absorbance

Using a common measuring beam in the spectrophotometer/polarimeter (*Materials and Methods*), the kinetics of the absorbance change at 430 nm, associated with  $b$ -heme reduction upon addition of dithionite, were measured simultaneously with the change in amplitude of the negative lobe of the Soret band split CD signal (open triangles, in red and blue, respectively (**Figure 3.4.C**)). The relatively slow time course of dithionite reduction of the  $b$ -hemes is a consequence of the

electrostatic barrier presented to dithionite, which is anionic at pH 8, by the hydrophobic interior of the cytochrome complex.

#### 3.4.4 Identity of the Interacting Heme Pair (s) Responsible for the Excitonic Interaction

Using the information available from the crystal structure of the bacterial *bc<sub>1</sub>* complex (PDB 1ZRT for *Rb. capsulatus*): the distance ( $r^{-3}$ ) and dihedral angle ( $\Theta$ ) dependence ( $\sin 2\Theta$ ) of the dipole-dipole interaction between the two hemes (**Table 3.1**) can be determined. The relative intensities of the excitonic CD signals generated by the six interacting heme pairs formed by the four *b*-hemes in the dimeric complex are summarized in **Table 3.1**, **Figure 3.5**. The CD spectra predicted to arise from the interaction between the different heme pairs, based on the arrangement of the *b*-hemes (**Figure 3.5 A**) in the crystal structure, are shown (**Figure 3.5B**). The experimental Soret CD spectrum (**Figure 3.4B**) has distinct positive and negative ellipticity lobes, respectively on the short and long wavelength sides of the absorbance peak. A comparison between the major features of the predicted (**Figure 3.5B**) and experimental CD spectra (**Figure 3.4 B**) shows that the CD spectra arise mainly from interaction between the intra-monomer p- and n-side heme pairs, p1–n1 and p2–n2 in the two monomers of the complex (**Figure 3.5B**). The question of whether the preferred state, after the transfer of a pair of electrons, is the inter-monomer “n–n” pair (**Figure 3.6A**) or the intra-monomer heme “n–p” pair (**Figure 3.6 B**), can be addressed through comparison of the functions describing the kinetics of the change in amplitude of (i) the absorbance change (heme reduction) and (ii) the excitonic CD spectra. If formation of the n–p state is favored, then the time course of heme reduction and development of excitonic heme-heme interactions will track each other closely, as found in the previous study of the *b<sub>6f</sub>* complex [65], and reproduced in a separate, original experiment (**Figure 4.4D**). If, on the other hand, the favored final state for the transfer of the first two electrons is reduction of the two n-side hemes (**Figure 3.6.A**), then the time course of the amplitude increase of both lobes of the CD signal (**Figure 3.4B**) will be delayed relative to the kinetics of the absorbance change because of the smaller strength of the n–n excitonic interaction (**Figure 3.5B**).

Table 3.1: Geometric Relations of Hemes in the *Rb. capsulatus bc1* Complex: (A) Heme center-center (Fe-Fe) distances; (B) interplanar angles between the four *b*-type hemes in *Rb. capsulatus* dimeric cytochrome *bc1* complex (PDB 1ZRT); For comparison, inter interheme geometric parameters of the cytochrome *b<sub>6</sub>f* complex (PDB 4OGQ) are shown in parentheses; (C) individual pair-wise contributions (in percent) to excitonic CD spectrum determined from the crystal structure relative to fully reduced CD amplitudes (100%), assuming contributions from all components in a fully reduced complex.

Heme pair	(A) Center-Center Distance (Å)	(B) Interplanar Angle (deg)	(C) Relative Contribution to CD Spectrum (%)
p1-n1/p2-n2	20.5 (20.6)	46.3 (52.0)	52.9
p1-p2	21 (22)	14.2 (17.2)	-6.0
n1-n2	34.3 (34.9)	30 (18.9)	-9.3
p1-n2/p2-n1	33.5 (33.8)	40.6 (48.4)	4.8

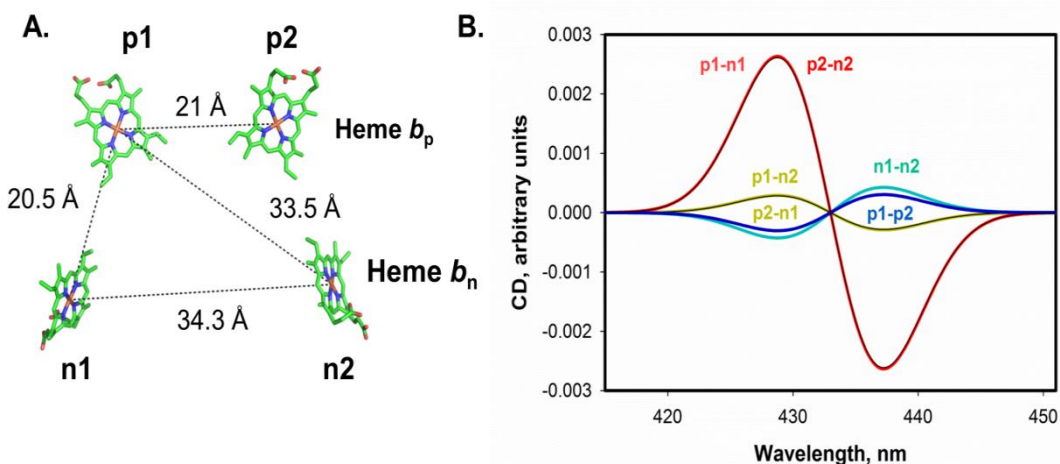


Figure 3.5: (A) Inter-heme (Fe-Fe) distances between the two trans-membrane *b* hemes, *b<sub>p</sub>* and *b<sub>n</sub>*, in the *Rb. capsulatus* cytochrome *bc<sub>1</sub>* complex (PDB 1ZRT). (B) Calculated relative amplitudes for the excitonically split CD spectra, based on heme distances and orientations in the crystal structure (PDB 1ZRT), for all reduced heme pairs: (i) p1-n1/p2-n2 (red), the dominant interaction; (ii) p1-n2 and p2-n1 (black and dark yellow); (iii) p1-p2 (blue), and (iv) n1-n2 (green).

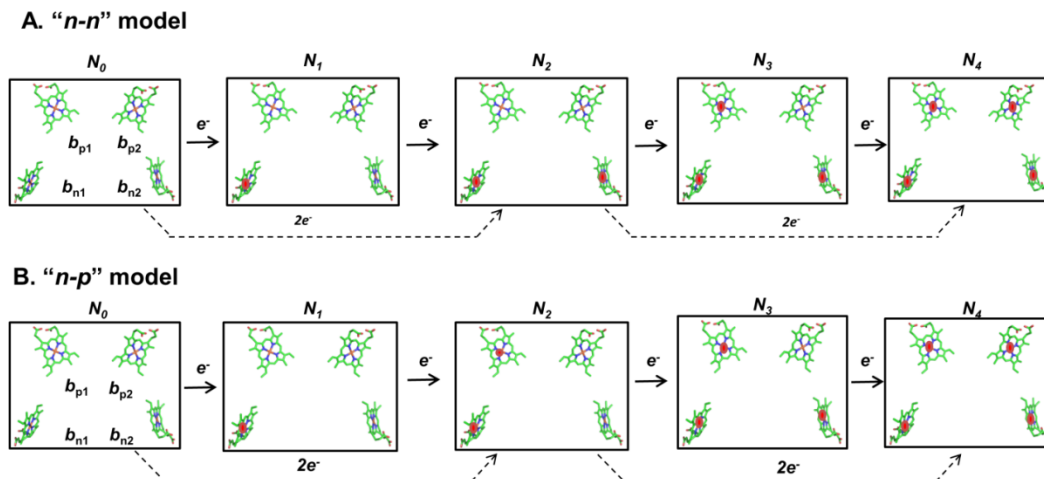


Figure 3.6: Pathways for reduction of b-hemes in cytochrome *bc* complexes. State  $N_0$  in panels A, B describes fully oxidized hemes in the dimeric complex.  $N_i$  represent states of the complex in which subscript "i" represents the number of reduced (red) hemes. (A) n-n model: doubly reduced state of lowest energy of the dimer corresponding to reduction of the two  $b_n$  hemes on different subunits, which would generate a weak negative CD signal (Figure 3.5 B). (B) n-p model: the lowest doubly reduced state of dimer corresponding to reduction of  $b_n$  and  $b_p$  hemes in the same monomer. Sequence of 4 reduction-electron transfer events corresponding to complete reduction of the 4 hemes in the dimeric complex is shown. States  $N_1$ ,  $N_3$  would be bypassed if dithionite would act as a  $2e^-$  donor.

### 3.5 Discussion

#### 3.5.1 Origin of Split Excitonic Circular Dichroism Spectra in Dimeric Heme Complex

Single heme proteins can display a CD signal of significant amplitude due to heme interaction with neighboring aromatic amino acids [146] or heme side chains [147], or inherent chirality [148]. However, there is no example in single heme studies of a Soret band split CD spectrum with the following properties: (i) an amplitude nearly as large (ca.  $10^{-3}$  of the absorbance peak extinction coefficient) and (ii) a node close to the Soret band absorbance maximum, as shown in the present study and previous CD studies of cytochrome *bc* complexes [65] which is not associated with large structural changes such as a significant out of plane displacement of the central metal [149]. Thus, it is inferred that the split CD spectra (Figure 3.4B) arise from excitonic interactions between heme pairs, predominantly the intra-monomer n-p pair (Figure 3.5B). This newly characterized spectroscopic parameter can be utilized to determine the preferred pathway for heme reduction in the bacterial *bc\_1* complex. In the present study, it is employed to contrast the electron equilibration patterns in the cytochrome *b\_6f* and bacterial *bc\_1* complex. Comparison of the

relative kinetics of heme reduction and increase in the excitonic CD signal (**Figure 3.4C**) was used to determine whether the preferred pathway of electron transfer to the *b* hemes results in preferential reduction of the two n-side hemes (**Figure 3.6.A**), as may anticipated from their relative redox potentials[133, 137, 145, 150], or of the intra-monomer heme pair as in the *b<sub>cf</sub>* complex (**Figure 3.6B**). The basis of this method is the different amplitude of the excitonic interactions between the different heme pairs, and particularly the relatively small interaction between the two n-side (n-n) hemes relative to the interaction between the intra-monomer n-p pair (**Figure 3.5B**).

Although single electron donation is the kinetically dominant reduction mechanism,[65] [151] the delay in formation of the CD signal associated with preferential population of the n-side hemes, as shown in the present study, is independent of whether dithionite donates one or two electrons [151]. The predicted relative time course for the transfer of 1- 4 electrons is shown (**Figure 3.7**).

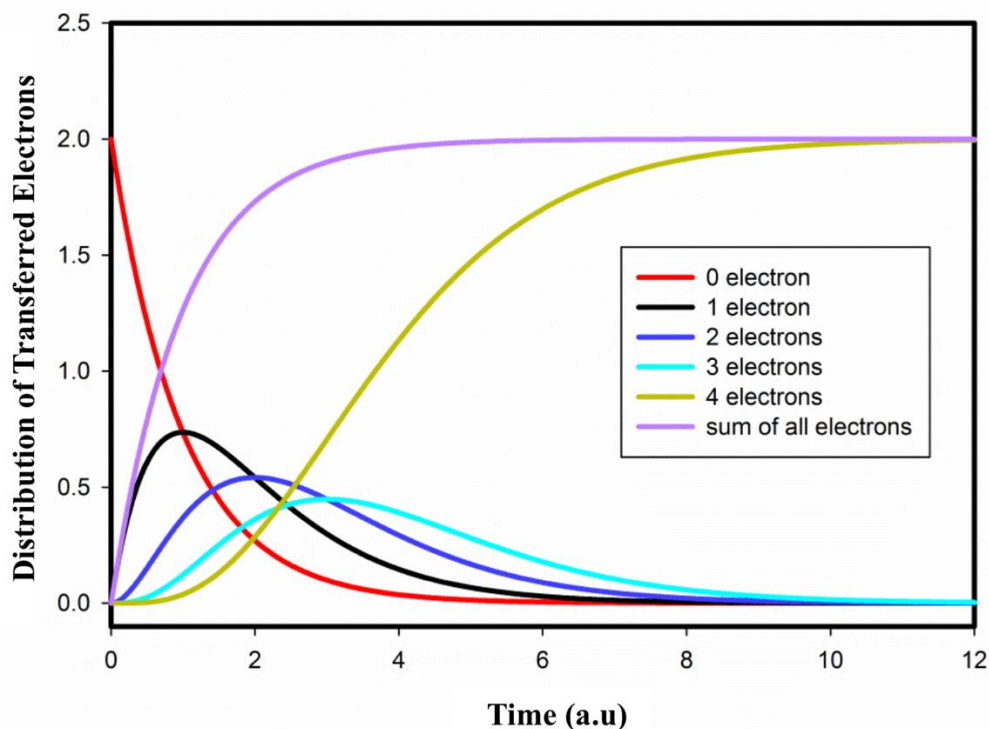


Figure 3.7: Distribution of the populations corresponding to the transfer of 0,1,2,3,4 electrons to each monomer of the dimeric complex and a sum of all 4 states (purple).

### 3.5.2 Comparison of Heme *b* Reduction in Cytochrome *b<sub>6</sub>f* and *bc<sub>1</sub>* Complexes: Inter-Heme Dielectric Constants

For the cytochrome *bc<sub>1</sub>* complex of *Rb. capsulatus*, in which the redox potentials of the *b* hemes on the two sides of the membrane are separated by at least 160 mV [133] chemical reduction of the four hemes in the dimer occurs with a kinetic preference for the higher potential inter-monomer pair of hemes, *b<sub>n</sub>*, on the electro-negative side of the complex. This pattern would be expected from the qualitative thermodynamics and free energy difference for oxidation-reduction of the two hemes in the *bc<sub>1</sub>* complex based on dye-mediated anaerobic titrations, which yielded a difference in mid-point potentials,  $\Delta E_m$ , between the n- and p-side hemes between ranging from 129 to 181 mV [133, 137, 145, 150], with a mean of  $\Delta E_m = 160$  mV [133]. This pattern of heme reduction contrasts, however, with that previously obtained for the preferred sites of the two electron reduced state of the *b*-hemes in the cytochrome *b<sub>6</sub>f* complex in which the intra-monomer n-p heme pair, rather than the n1 – n2 pair, was preferentially reduced by the chemical reductant, dithionite [65]. A significant difference in the properties of the two cytochrome complexes is the substantially smaller redox potential difference between the n- and p-side hemes in the *b<sub>6</sub>f* complex, for which redox titrations of the isolated/purified cytochrome complex have determined a value of the  $\Delta E_m \approx 90 - 100$  mV [36, 152-154]. This difference was found to be even smaller, with a  $\Delta E_m$  not resolvable, in titrations of the complex in membranes [46, 155], although a difference was found in another such study [156]. It should be noted in a discussion of such redox titrations that a general problem, particularly with the isolated complex, is that the  $E_m$  of membrane protein hemes that reside in a hydrophobic environment is sensitive to the local solvent polarity, tending to shift in the negative direction when removed from the membrane and exposed to a more polar environment [157].

The explanation for the difference in pathways of reduction of the *b*-hemes in *bc<sub>1</sub>* and *b<sub>6</sub>f* complexes, based on potentiometric titration with redox mediators, is that the thermodynamics in this problem include not just the magnitude of the redox potential difference,  $\Delta E_m$ , between the trans-membrane hemes, but also the contribution of inter-heme Coulomb interactions. Including the latter component in the total  $\Delta G_p$  of the inter-heme interaction allows a calculation of the inter-heme dielectric constant [65]. For the *b<sub>6</sub>f* complex, assuming a dielectric constant of 2.5 and a  $\Delta E_m = 100$  mV between the two *b<sub>n</sub>* hemes [60], and applying equation 4b described below, a more polarizable intra-monomer inter-heme medium characterized by a

dielectric constant  $\epsilon \geq 10.8$ , implies preferential reduction of the intra-monomer heme pair. The origin of the relatively high dielectric constant may be water bound in the protein structure near the hemes, as documented in the structure (1.9 Å resolution) of the yeast mitochondrial *bc<sub>1</sub>* complex [PDB 3CX5][60].

### 3.5.3 Calculation of Dielectric Heterogeneity for the cytochrome *bc<sub>1</sub>*

The total energy  $E_{ij}$  of a heme pair can be expressed as:

$$E_{ij} = E_i + E_j + V_{ij} \quad (1)$$

where  $E_i$  and  $E_j$  are the energies of non-interacting electrons in sites  $i$  and  $j$ , and are defined by the redox potentials of the respective  $b$  hemes.  $V_{ij}$  is an additional coulombic interaction energy between the added electron on each of the two interacting hemes. The indices  $i$  and  $j$  correspond to the reduction of one of the four  $b$ -hemes:  $i, j = n1, p1, n2, p2$ . The electrostatic interaction energy,  $E_{ij}$ , in a point-charge approximation, described by Coulomb's law, is:

$$V_{ij} = \frac{e^2}{4\pi\epsilon_0\epsilon_{ij}R_{ij}} \quad (2)$$

where  $e$  is the electric charge,  $R_{ij}$  the distance between the two electric charges located on the two reduced hemes,  $\epsilon_0$  the permittivity of free space, and  $\epsilon_{ij}$  is the effective dielectric constant that operates between heme pairs,  $b_i$  and  $b_j$ . Equation 2 can be rewritten as described below, with the units of  $R_{ij}$ , the center-to-center distance between the respective hemes in Å,  $E_{ij}$  in electron-volts (eV), and the dimensions of the numerator in units of Å · eV.

Hence, the energies corresponding to the 2-electron reduction of the different  $b_p$ - $b_n$  pairs are:

$$V_{ij} = \frac{14.4 [\text{Å} \cdot \text{eV}]}{\epsilon_{ij} \cdot R_{ij}} \quad (3)$$

### 3.5.4 Summary of formulae that describe the energy of the different reduced states in the cytochrome *bc<sub>1</sub>* complex

The energies corresponding to reduction of the  $b_p$ - $b_n$  pairs,  $n1$ - $n2$  and  $n1$ - $p1$ ,  $n2$ - $p2$  are:

$$E_{n1,n2} = \frac{14.4 [\text{Å} \cdot \text{eV}]}{\epsilon_{n1,n2} \cdot R_{n1,n2}} \quad (4a)$$

$$E_{n1,p1} = E_{n2,p2} = \Delta E_m + \frac{14.4 [\text{Å} \cdot \text{eV}]}{\epsilon_{n1,p1} \cdot R_{n1,p1}} \quad (4b)$$

The energies for the cross-monomer interactions  $n1/p2$  and  $n2/p1$  are not shown. Energies are measured with respect to the redox potential of heme  $b_n$  (i.e. the energy of singly reduced *bc<sub>1</sub>*

complex is set to zero eV). The additional  $\Delta E_m$  term in equation 4b expresses the contribution to the system energy of the redox potential difference between the intra-monomer hemes.

### 3.5.5 *n-side and inter-heme $\epsilon$ values*

Considering the larger difference in redox potentials,  $\Delta E_m = 160$  mV, in the bacterial *bc<sub>1</sub>* complex between the intra-monomer hemes  $b_n$  and  $b_p$ , it can be anticipated that the intra-monomer dielectric constant would have to be significantly larger to accommodate an energetically favorable reduction of the intra-monomer hemes  $b_n$  and  $b_p$  and thus indicative of a more polar environment. The boundary value for  $\epsilon_{n-p}$  that favors reduction of the n-n heme pair is highly dependent on the value of  $\epsilon_{n-n}$ . Using the same reference dielectric constant of 2.5 for the medium between the two hemes  $b_n$ , that was utilized for analysis of the *b<sub>6</sub>f* complex and which is characteristic of an apolar medium ( $\epsilon=1$ ), in the equations (4a,b), the larger  $\Delta E_m$  leads to an unreasonable intra-monomer inter-heme dielectric constant with a value,  $\epsilon_{n-p} \leq 88$ , extending to the range of the constant for water, making the pathway energetically unfavorable and unreasonable.

Table 3.2: Threshold Inter-Heme Dielectric Constants ( $\epsilon_{np}$ ) in Cytochrome *bc<sub>1</sub>* Complex (assuming  $\epsilon_{n1, n2} = 2.0$ ).

$\Delta E_m(\text{mV})$	$\epsilon_{n1,p1}$
160	$\leq 14.3$
150	$\leq 12.0$
100	$\leq 6.5$
50	$\leq 4.4$

Given the lack of knowledge of the precise value for the reference dielectric constant, the consequences of a value of 2, in the range of values for apolar media ( $\epsilon=1$ ), for the medium between the two hemes  $b_n$  is examined. It leads to a value of 14.3 for the intra-monomer dielectric constant,  $\epsilon$ , which would allow an energetically favored reduction of the intra-monomer n-p heme pair. Because it is the inter-monomer n-n heme pair whose reduction is favored, it is concluded that the intra-monomer inter-heme dielectric constant,  $\epsilon \leq 14.3$  (**Table 3.2**), for a mid-point potential difference  $\Delta E_m = 160$  mV.

### 3.5.6 Structure Differences between *b<sub>6f</sub>* and *bc<sub>1</sub>* Complexes: Inter-Heme Orientation

Similarities of the structure and function of cytochrome *bc<sub>1</sub>* and *b<sub>6f</sub>* complexes have been described [44]. Further comparison of the high resolution structures of the bacterial *bc<sub>1</sub>* (PDB 1ZRT) and cyanobacterial *b<sub>6f</sub>* complex (PDB 4OGQ) indicates that, in the bacterial *bc<sub>1</sub>* complex, the relative orientation of the hemes described by the inter-heme dihedral angles, particularly between the two hemes *b<sub>n</sub>*, and to a lesser degree all other inter-heme angles involving the hemes *b<sub>n</sub>*, are different relative to the *b<sub>6f</sub>* complex (**Table 3.1**). It might be proposed that a structure-based explanation for this difference is the unique presence in *b<sub>6f</sub>* of the unique heme *c<sub>n</sub>* [27, 29, 36, 152, 154], which is linked closely to heme *b<sub>n</sub>* (4 Å between the heme *b<sub>n</sub>* propionate and the Fe atom of *c<sub>n</sub>*), but is not present in the *bc<sub>1</sub>* complex. However, the interaction between these hemes occurs at the n-side edge of heme *b<sub>n</sub>*, whereas the twist of the heme plane responsible for its different orientation occurs mainly at its p-side edge where Gly-115 in the helix B of the cytochrome *b* polypeptide in the *bc<sub>1</sub>* complex is replaced by Val-104 in the *b<sub>6f</sub>* complex (**Figure 3.8**). This substitution of the bulkier residue forces the heme *b<sub>n</sub>* away from the B helix in the *b<sub>6f</sub>* complex. Two other major differences in the structures of the cytochrome complexes, in the vicinity of both hemes, is the presence of a (i) conserved arginine (R-87) residue in the vicinity of heme *b<sub>p</sub>* in the *b<sub>6f</sub>* complex, which is substituted by alanine (A-96) in the *bc<sub>1</sub>* complex and (ii) a conserved arginine (R207) residue in the vicinity of hemes *b<sub>n</sub>* - *c<sub>n</sub>* in the *b<sub>6f</sub>* complex, which is substituted by a histidine residue (H217) in the *bc<sub>1</sub>* complex (**Figure 3.8**).

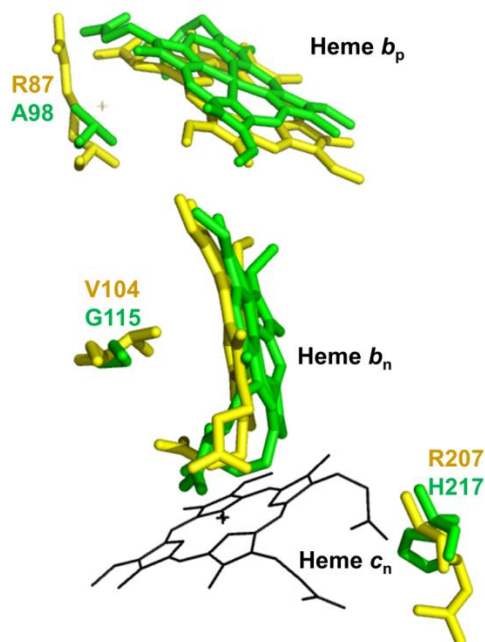


Figure 3.8: Structural alignment of hemes  $b_p$ ,  $b_n$  and  $c_n$  from the cyanobacterial  $b_6f$  complex (yellow; PDB 4OGQ) and bacterial  $bc_1$  (green, PDB 1ZRT). Residues R87 and R207 (yellow) are conserved in the  $b_6f$  complex, whereas they are replaced by A98 and H217 (green) in the  $bc_1$  complex. Glycine residue (G115) in the  $bc_1$  complex is replaced by a bulkier valine residue (V104) in  $b_6f$ .

The intermonomer cavities of both  $bc$  complexes, are lined by an N-terminal surface helix and D helices of each monomer, belonging to the  $b$  or  $b_6$  subunit. Upon a close inspection of the helix geometries and orientations, it can be seen that (i) the D helices of each monomer in the  $b_6f$  complex have been moved towards each other by about 2.5 Å in comparison to  $bc_1$  complex (**Figure 3.9 A**) and (ii) the N-terminal surface helix of cyt.  $b_6f$  has been displaced below that of cyt  $bc_1$  by approximately 5 Å (**Figure 3.9.B**).

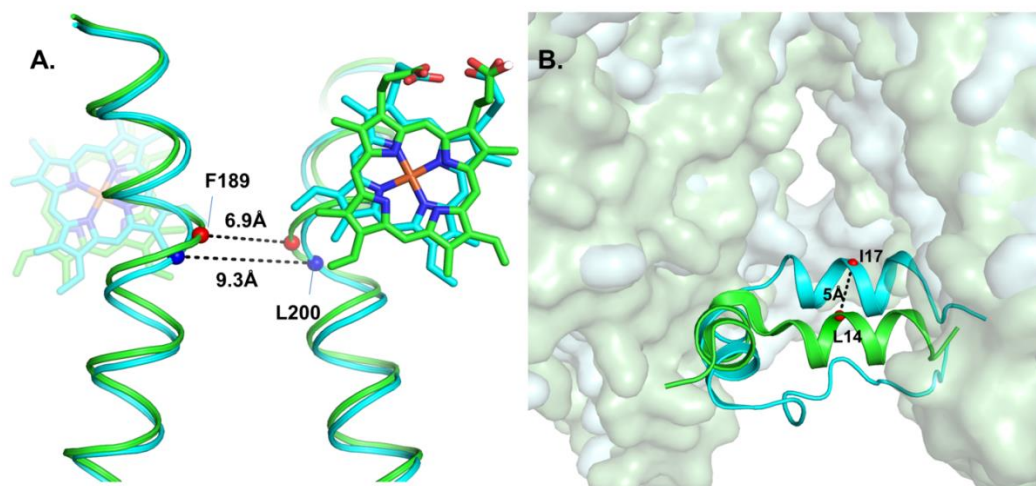


Figure 3.9: (A) Structural alignment of D-helices lining the inter-monomer cavity in *cyt bc<sub>1</sub>* (cyan, PDB 1ZRT) and *b<sub>6</sub>f* complex (green, 4OGQ). The distance between F189 and L200 in the corresponding turn of the D-helix of the *b<sub>6</sub>f* and *bc<sub>1</sub>* complexes respectively, differ by 2.4 Å, which indicates the extent by which the distance between the two monomers is diminished in *b<sub>6</sub>f* compared to *bc<sub>1</sub>*. (B) Cartoon structures show that the N-terminal n-side surface helix of *b<sub>6</sub>f* (green), is displaced further from the n-side surface than the corresponding helix in *bc<sub>1</sub>* (cyan) by a distance of 5 Å, as indicated by the dotted line that bridges the two helices.

An interesting feature of the D-helix of the *b<sub>6</sub>f* complex, which probably has led to it being displaced towards the other monomer, is the presence of an extra threonine residue (T188) [158], which results in a tighter packing of the protein proximal to heme *b<sub>p</sub>* in the *b<sub>6</sub>f* complex than in *bc<sub>1</sub>*.

### 3.6 Conclusion

In the present study, we utilized a novel approach of combining experimentally measured and crystal structure based calculated CD spectra to determine the preferential pathway of heme reduction in the cytochrome *bc<sub>1</sub>* complex from *Rb. capsulatus*. The preferred “n-n” pathway for heme reduction in the bacterial cytochrome *bc<sub>1</sub>* complex contrasts with the “n-p” pathway utilized in the *b<sub>6</sub>f* complex. This is a consequence of the substantially larger midpoint redox potential difference,  $\Delta E_m$ , in the *bc<sub>1</sub>* complex, which cannot be compensated by more favorable intra-monomer inter-heme coulombic interactions across the intervening dielectric medium.

## CHAPTER 4. ISOLATION AND CHARACTERIZATION OF NOVEL PHOTOSYSTEM I- ATP SYNTHASE SUPERCOMPLEX FROM SPINACH

### 4.1 Summary

Several supercomplexes formed by hetero-oligomeric membrane protein complexes in the respiratory and photosynthetic electron transfer chains which facilitate the intra-membrane electron and proton transfer, have been recently characterized. In this study, a novel intra-membrane chloroplast supercomplex, dominated by the ATP synthase, photosystem I (PSI) reaction-center complex, and the ferredoxin-NADP<sup>+</sup> reductase (FNR), has been isolated from spinach chloroplast thylakoid membranes. The composition of the super-complex has been defined by mass spectrometry, Western Blot assay of the presence of PSI, ATPase, and FNR, the latter component confirmed by fluorescence spectroscopy, and negative stain electron microscopy. The dominant presence of ATPase in the super-complex together with the PSI reaction center in the complex is the first documented supercomplex in the non-appressed stromal membrane domain of the chloroplasts. A function of the ATPase-PSI reaction center-FNR super-complex in localized fixation of CO<sub>2</sub> is discussed.

### 4.2 Introduction

Supercomplexes of hetero-oligomeric electron transport membrane protein complexes, formed in the fluid-mosaic membrane environment [159, 160], have been extensively described in mitochondria [161-164] where their formation has been shown to be facilitated by anionic lipids [62-64, 66] and the intactness of the entire respiratory electron transport chain has been documented by cryo-electron microscopy [161, 164-167].

The chloroplast thylakoid membrane contains four large hetero-oligomeric energy-transducing protein complexes (**Figure 4.1**): (i) the photosystem II (PSII) reaction center complex, responsible for the primary photochemistry associated with water splitting [85]; (ii) the 235 kDa cytochrome *b<sub>6</sub>f* complex, which provides the quinol acceptor and electron transfer connection and trans-membrane proton translocation pathway between the PSII and PSI reaction centers [28, 168]; (iii) the 530 kDa plant photosystem I (PSI) complex [79, 86] which is responsible for reduction of

ferredoxin in the above-mentioned pathway of cyclic electron transport, and reduction of NADP<sup>+</sup> utilized for CO<sub>2</sub> fixation; (iv) the 560 kDa ATPase/synthase [82, 169].

The chloroplast thylakoid membrane is arranged with the energy transducing protein complexes arranged in two structurally distinct membrane domains, (i) the appressed grana membranes, and (ii) the non-appressed stroma or stroma-facing membrane compartments [170] (**Figure 4.1**). The membrane location of the PSI, PSII, *b<sub>6</sub>f*, and ATPase protein complexes, has been discussed in the context of long-range redox communication [171], and the locations in grana and stromal compartments of the redox proteins that function in the ‘non-cyclic’ electron transport pathway from water to NADP<sup>+</sup>, and the PSI-linked redox proteins responsible for cyclic electron transport and linked phosphorylation [15].

The description of super-complexes in thylakoid membranes, which mostly concern complexes of the photosystem II reaction center and associated light harvesting pigment proteins [172-178], including a high resolution crystallographic analysis of the electron transport/water-splitting structure [85], has led to a better perspective on the organization of the membrane protein complexes that support the light harvesting, and the electron transport-proton translocation functions central to photosynthetic membrane energy transduction.

Super-complexes isolated thus far from chloroplasts have been derived primarily from the appressed membrane domain (**Figure 4.1**): (i) Such complexes have been obtained with different ratios of LHC: reaction center and a different abundance in plants [172-174] compared to the alga *C. reinhardtii* [175]. (ii) Nano-domains surrounding the PSII reaction center have been described by atomic force microscopy to be populated by the *b<sub>6</sub>f* complex [179], present in appressed and non-appressed membrane domains [180]. (iii) A cytochrome *b<sub>6</sub>f* complex from *C. reinhardtii*, containing light harvesting complexes LHCI and LHCII and ferredoxin-NADP<sup>+</sup> reductase (FNR), was obtained under conditions (‘state 1- state 2 transition’) favoring light energy transfer from the antenna pigment proteins to the PSI reaction center complex [76]. (iv) Binding of the *b<sub>6</sub>f* complex in *Arabidopsis thaliana* was determined relative to the chlorophyll pigment-protein, Lhca1 [77] (v) A super-complex of the PSI reaction center and the cytochrome *b<sub>6</sub>f* complex was isolated from cold-adapted *C. reinhardtii* [181], and (vi) the crystal structure described of the PSI reaction center associated with light-harvesting complex from a plant (pea) source [68]. The presence of PSI and ATPase in the edges of the stacked grana membranes has been noted [182, 183].

The present study concerns a super-complex that combines the two hetero-oligomeric membrane protein complexes, ATPase and the PSI reaction center, from a plant source and FNR. This is the first characterized membrane protein supercomplex in which the ATP synthase has a major presence. This inference has been documented by the use of negative stain electron microscopy (EM), high-resolution Orbitrap mass spectrometry (in collaboration with Prof. J.P.Whitelegge, UCLA) to analyze the contribution of multiple major and minor protein components, immuno-blot analysis to identify protein subunits of the component complexes, and excitation and emission fluorescence spectral analysis to further document the presence of FNR.

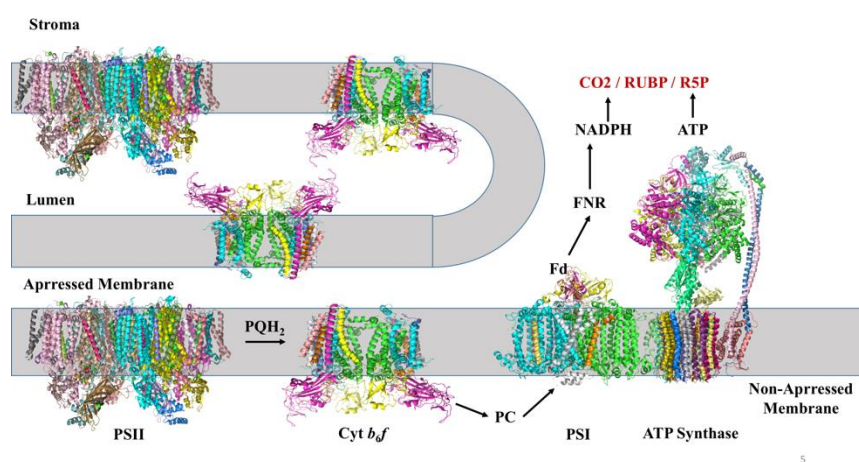


Figure 4.1: Distribution in thylakoid membranes between appressed (grana) and non-appressed (stroma) membranes of the major intra-membrane energy transducing complexes associated with oxygenic photosynthesis: photosystem II (PSII), photosystem I (PSI), cytochrome *b*<sub>6</sub>*f* complex, and ATP synthase, with molecular weights, respectively, of approximately 350, 530, 270 (with FNR), and 560 kDa. The possibility of localized reduction of CO<sub>2</sub>, suggested by the ATPase-PSI-FNR super-complex, is indicated. Light-harvesting chlorophyll complexes are not shown.

### 4.3 Materials and Methods

#### 4.3.1 Purification of Super-Complex.

Spinach leaves macerated in darkness in HEPES-KOH pH 7.5, 150 mM NaCl, 5 mM EDTA at 4 °C and sedimented at 4000g, were re-suspended in HEPES (4-(2-hydroxyethyl)-1-piperazine-ethanesulfonic acid) -KOH pH 7.5, 15 mM NaCl, 5 mM EDTA, centrifuged at 4,000 x g, and re-suspended in the same medium containing 5 mM NaCl. The chlorophyll concentration of thylakoid membranes was adjusted to 1 mg/ml, extracted with 1 % DDM, centrifuged at 15,000

x g, the supernatant loaded on a 4-40% sucrose density gradient, and centrifuged at 200,000 x g. Four independent purification analyses showed results identical to those in **Figure 4.2**.

#### 4.3.2 *Electrophoretic Analysis*

Protein bands from the sucrose gradient were fractionated, run on 4-12 % Clear-Native PAGE, and eight resolved complexes excised for mass spectrometric analysis. The largest band of approximately 1 MDa on the native gel (**Figure 4.2 B**) is discussed at length.

#### 4.3.3 *Western Blotting*

Isolated super-complex was assayed on SDS and Clear-Native PAGE, and transferred to a nitrocellulose membrane, the blot probed with anti-ATP synthase  $\alpha$ -subunit, anti-PsaA subunit for PSI and anti FNR antibodies, raised in *Arabidopsis* (PhytoAB Co.), followed by HRP-conjugated anti-rabbit secondary antibody, with chemi-luminescence detected using an 'Image Quant LAS 4000' (GE Healthcare).

#### 4.3.4 *Mass Spectroscopy (Done in the laboratory of Prof. Julian P. Whitelegge, UCLA)*

Mass spectrometry was performed as described previously using nano-liquid chromatography and a bench top Orbitrap mass spectrometer (QE-Plus, Thermo-Fisher Scientific) operated in positive ion mode (nLC-MSMS). Proteins in native gel-bands were alkylated, digested with trypsin and extracted for nLC-MSMS. The Mascot Search Algorithm (Matrix Science, London, UK) was utilized to identify the significant presence of peptides, using 10 ppm mass tolerance on high-resolution precursor MS1 scans, and 20 milli-mass unit tolerance on high-resolution product MS2 scans, obtaining an overall < 5% peptide false discovery rate based upon a reversed sequence decoy search. A Mascot protein eligibility score of 200 was selected based upon the presence of at least two different high-scoring peptides and used as an arbitrary lower boundary to define the presence of a particular protein if a majority of the remaining subunits in the complex were also present. This approach is adequate for PS1 and ATPase which each have an extensive 'extrinsic' polypeptide sequence that yields many easily recoverable peptides for the proteomic analysis but becomes less clear for the *b<sub>6</sub>f* complex that has less extrinsic peptide mass thus yielding fewer peptides in the MS analysis and lower overall protein scores.

#### 4.3.5 *Assay of ATPase Activity.*

The “ADP-glo” kit (Promega, Wisconsin) was used to measure hydrolysis of ATP to ADP and inorganic phosphate by ATPase. ATP (0.4 mM) was added to the super-complex fraction in the presence of buffer (50 mM Tris-HCl, 5 mM Mg<sup>2+</sup>, and BSA) at room temperature, incubated 15 min, followed by the addition of “ADP-glo reagent” and incubation at room temperature (40 min) to consume unused ATP. The reaction mixture was then incubated with the ‘detection reagent’ to convert ADP to ATP, measured by the reaction of luciferase/luciferin, and the luminescence recorded in a spectral band centered at 560 nm, utilizing a Spectramax Luminometer (Molecular Devices, CA.).

#### 4.3.6 *Negative Stain Electron Microscopy.*

The ATPase-Photosystem I reaction center-FNR super-complex, fractionated on a 10-40 % sucrose density gradient, was applied to glow discharged 400 mesh copper grids and washed with distilled water to remove excess buffer without allowing the grid to dry. Grids were blotted, immediately stained with 1% phospho-tungstic acid, and excess stain removed. All preparations were carried out at 4 °C. Data were acquired on a FEI Tecnai transmission electron microscope operated at 200 keV.

#### 4.3.7 *Fluorescence Spectroscopy.*

Fluorescence measurements were made with a FluoroMax 3 Fluorimeter (Horriba-Yvon Inc.), using a 3 x 3 mm quartz microcell with 0.3 ml volume. FAD containing the super-complex fraction in 10 mM HEPES buffer, pH 7.5, 0.5 mM EDTA, 2 mM DDM, 10 % sucrose, was excited at 460 nm, and emission spectra collected in the 500-580 nm spectral interval, with a wavelength stepping increment of 1 nm and a 0.1 sec integration time. Excitation spectra were measured from 420 to 500 nm using an emission band interval centered at 530 nm. Difference spectra were obtained by measuring the fluorescence in the presence and absence of sodium dithionite, a reductant with a redox potential negative enough to fully reduce the flavin in FNR, thus eliminating most of its characteristic absorbance and fluorescence.

## 4.4 Results

### 4.4.1 A unique super-complex from thylakoid membranes that functions in oxygenic photosynthesis; electrophoretic and immuno-blot analysis.

The super-complex was isolated from spinach by sucrose-gradient centrifugation (**Figure 4.2 A**), and the approximate size determined on a 4–12 % clear-native gel (**Figure 4.1B**, standards on left). The band marked ‘SC’ in Figure 4.2 A is estimated to contain approximately 20 % of the total amount of detergent-extracted protein loaded on the gradient.

The super-complex subunits are more completely visualized in a silver-stained gel (Figure 4.2 C). The presence of ATPase, PS I and FNR were confirmed by Western blots using antibodies raised against *Arabidopsis* ATP synthase  $\alpha$ -subunit (55 kDa) (**Figure 4.2 D**), the 60 kDa PsaA subunit of PSI (**Figure 4.2 E**), and FNR (36 kDa) (**Figure 4.2 F**).

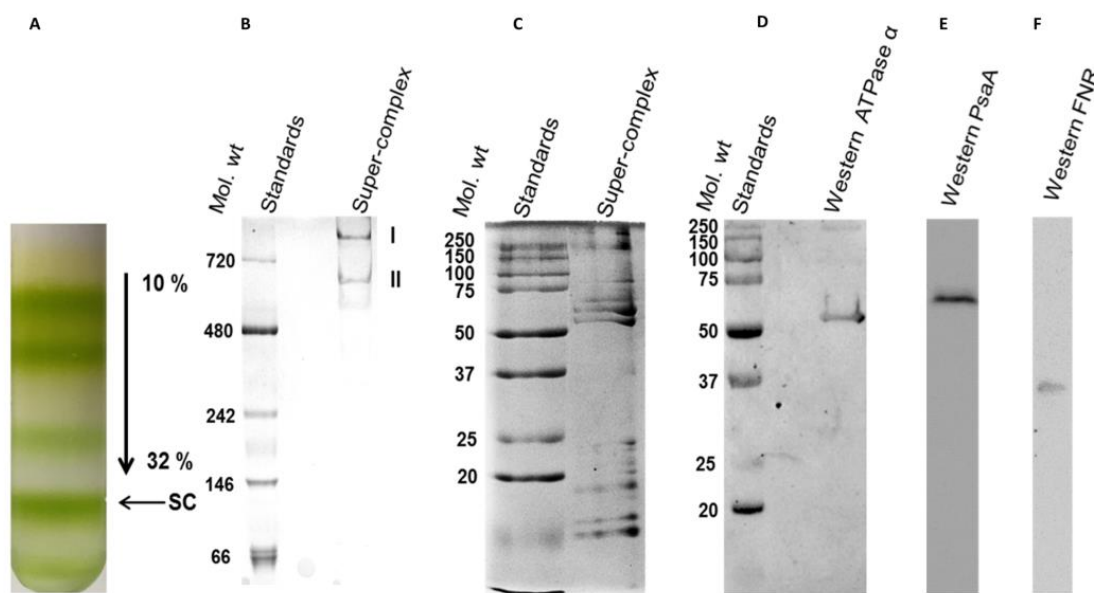


Figure 4.2: Purification and characterization of the PSI-ATPase-FNR super-complex. (A) 4–40 % sucrose density gradient of spinach thylakoid membrane extract. Super-complex (SC), marked by the arrow, is separated for further characterization. (B) 4–12 % Clear Native PAGE of the super-complex fraction isolated from the sucrose gradient and stained with Coomassie Brilliant Blue R-250. Bands marked I and II are the PSI-ATPase-FNR super-complex migrating at approximately 1.0 and 0.7 MDa. (C) Silver stained 2-D gel of the super-complex. (D, E, F) Western blots of super-complex fraction 1 using 12 % SDS-PAGE probed with antibodies raised against (D)  $\alpha$ -subunit (55kDa) of *Arabidopsis* ATP synthase, (E) PsaA subunit (60 kDa) of PSI, and (F) FNR (36 kDa).

#### 4.4.2 Mass Spectrometry.

High-resolution mass spectrometry of the isolated 1 MDa super-complex from spinach chloroplast thylakoid membranes (Table 4.1) revealed the presence of ATP synthase (0.56 MDa), Photosystem I (0.53 MDa) and FNR (35 kDa). Polypeptide components derived from band in **Figure 4.2 B**, were identified after in-gel digestion of the native gel-band and tandem mass spectrometry with data base searching constrained by a specified high statistical confidence threshold, as described in *Methods*, and summarized in **Table 4.1**. Ten of the twelve subunits of the PSI complex from the band (**Figure 4.2 B**) were detected (**Table 4.1**), while two other subunits, psaH and psaK, were just below a conservatively chosen Mascot threshold limit of 200 (see *Materials and Methods*).

Table 4.1: Relative abundance (Mascot Search Algorithm) of polypeptide components identified in the trypsin in-gel digest of the ATPase-PSI-FNR super-complex spinach thylakoids of approximately 1 MDa as shown on clear native PAGE (**Figure 4.2 B**).

Photosystem I	I	ATP Synthase	I
psaA	209	atpA	583
psaB	1124	atpB	1159
psaC	326	atpC	115
psaD	870	atpD	382
psaE	291	atpE	366
psaF	342	atpI	---
psaG	247	atpF	249
psaH	137	atpH	
psaK	151	FNR	354
psaL	762	Cytochrome b <sub>6</sub> f	
lhca4	---	petA	177
lhcb1	---	petC	103
Chl ab binding protein	113	petB	79
		petD	28
CO <sub>2</sub> Fixation Enzymes			
ribulose biphosphate carboxylase, small chain	32		
glyceraldehyde-3- phosphate dehydrogenase	53		
ribulose-1,5- biphosphate carboxylase/oxygenas e, large subunit	19		
ribulose-1,5- biphosphate carboxylase/oxygenas e, large subunit	79		

For ATP synthase, six of the eight major subunits were observed in the 1 MDa band labeled. Among the additional polypeptides present, FNR was well above the Mascot threshold, and thus is regarded as a major component of the putative super-complex, designated ATPase-PSI-FNR. The presence of FNR was confirmed through a Western blot using an anti-FNR antibody probe (**Figure 4.2 F**), and determination of the fluorescence excitation and emission spectra that are characteristic of FAD [184] (**Figure 4.3**). Major subunits of the *b<sub>6</sub>f* complex are detected, but at sub-threshold values, and only the cytochrome *f* subunit is close to the Mascot-defined threshold score.

Other polypeptides purified with the ATPase-PSI-FNR super-complex, with low abundance attributed to their soluble nature, but of implied significance because of their utilization of ATP and FNR, and their requirement for the reductant provided by PSI, are the Calvin cycle enzymes ribulose-1,5-bisphosphate carboxylase/oxygenase, and glyceraldehyde-3-phosphate dehydrogenase, which catalyze the first steps of carbon fixation.

#### 4.4.3 *Presence of FNR in Super-Complex.*

The presence of FNR in the spinach super complex was inferred from fluorescence emission and excitation spectra produced by the isoalloxazine moiety of FAD (**Figure 4.3A, B**). The super-complex, suspended in 10 mM HEPES buffer, pH 7.5, and 0.5 mM EDTA, 2 mM DDM, 10 % sucrose, was exposed to excitation at 460 nm, and emission spectra were acquired over the wavelength range 500-600 nm. The difference emission spectrum, calculated with and without the strong reductant, sodium dithionite, which is expected to eliminate most of the amplitude of the flavin absorbance at 460 nm, showed an emission maximum in the oxidized state at 530 nm, which is characteristic of the presence of flavin. A similar conclusion was reached from the difference excitation spectra measured with and without sodium dithionite over the 400-500 nm range using emission at 530 nm. The excitation spectrum showed a maximum at 460 nm, characteristic of oxidized flavin [184]. Spectra are normalized to unit emission intensity.

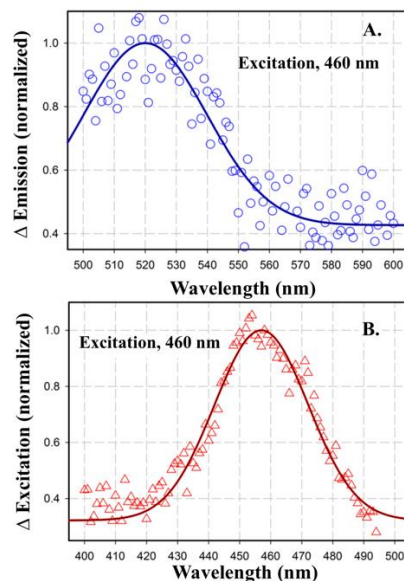


Figure 4.3: Difference fluorescence emission (top) and excitation (bottom) spectra of the ‘super-complex;’ measured with a FluoroMax 3 Fluorimeter (Horiba-Yvon Inc.). **(A)** Emission spectra measured between 500 – 600 nm. Stepping increment, 1 nm; Integration time, 0.1 sec; Excitation, 466 nm; the bandwidth was 5 nm for excitation and emission. **(B)** Excitation spectra measured in 400–500 nm range, measuring the emission at its 530 nm peak. Spectra of undiluted sample were measured in a quartz microcell, 3 x 3 mm, volume, 0.3 ml (Starna Cells) before and after addition of dithionite grains. Difference spectra were obtained by subtraction of spectra, i. e., ‘oxidized–reduced,’ measured before and after addition of dithionite.

#### 4.4.4 ATPase Activity.

The F1-ATPase component in the super-complex demonstrated *in vitro* ATP hydrolysis, as described in *Methods*. The “ADP-glo kit” (Promega) was used to provide a qualitative measure of ATP hydrolysis, which depends on the presence of the PSI-ATPase-FNR super-complex (**Figure 4.4**). ATP hydrolysis was measured by addition of 0.4 mM ATP to the super-complex fraction in the buffer containing 50 mM Tris-HCl, 5 mM Mg<sup>2+</sup>, and 0.1 mg/ml BSA). The luciferase emission signal detected in a band centered at 560 nm in lane 2 demonstrated the ATPase component in the complex to be active.

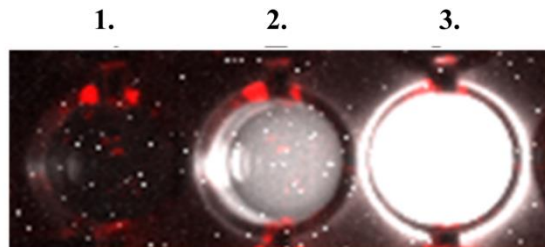


Figure 4.4: ATPase Activity of the Super-Complex. As described in *Methods*, kinase activity was measured qualitatively through luciferase emission when the reaction mix was added: to lane 1 containing buffer and 0.4 mM ATP (negative control); to lane 2 containing purified super-complex and ATP (0.4 mM) in which the ATPase activity of the super-complex is assayed; to lane 3 with buffer and 0.4 mM ADP (positive control). Signal detected in lanes 1, 2, and 3 was  $2.3 \times 10^5$ ,  $1.9 \times 10^6$ , and  $4.7 \times 10^6$  cpm, respectively. Luminescence in lane 2 arises from hydrolysis of ATP to ADP and inorganic phosphate by the F1-ATPase.

#### 4.4.5 Negative Stain Microscopy of the Super-Complex.

The super-complex described by negative stain microscopy, consisting of intact ATPase and the photosystem I reaction center complex, is also inferred from the characteristic dimensions and shapes, documented by the geometric similarity to the crystal structures of PSI (PDB 5L8R) and ATPase (PDB 5DN6) (**Figure 4.5B**). The projection image displays a trans-membrane complex with dimensions of 18 nm x 4.5 nm for photosystem I and 4.7 nm x 8 nm for the Fo, F1 components of the ATPase. The dimensions of the particles seen by negative stain electron microscopy and the molecular weight (1.0 MDa) of the band on the native gel (**Figure 4.5 A**) imply that the stoichiometry of ATPase and PS I reaction center is 1:1. The smaller FNR component, molecular weight, 36 kDa, is not seen at the present level of resolution.

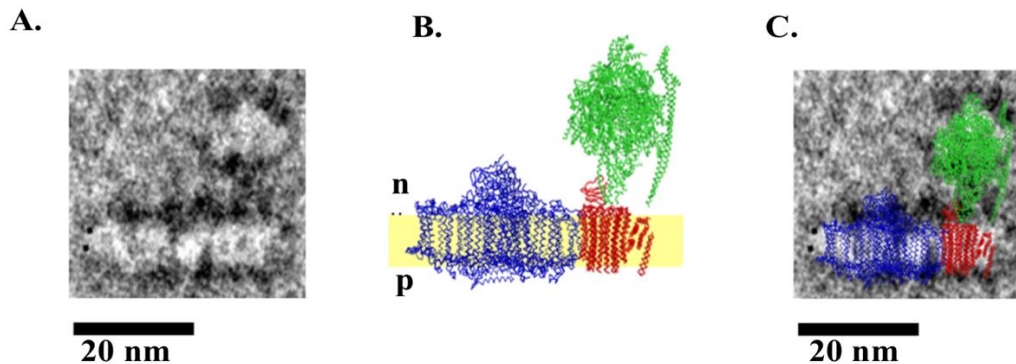


Figure 4.5: Negative stain EM analysis of the PSI-ATPase Super-Complex. (A) Negative stain image of PSI-ATP synthase particle. The EM particle density is shown in white, while the stain and background are in black. (B) Crystal structures of PSI and ATP synthase re- Lipid bilayer drawn in yellow. n, p: electrochemically negative (stroma) and positive (lumen) sides of the membrane. (C) Overlay of crystal structures of PSI (blue, PDB ID 5L8R) and ATP synthase (red-green, PDB ID 5DN6) on the negative stain envelope of the PSI-ATP synthase super-complex particle. 47 trans-membrane helices of PSI, and 14 C- subunits of the Fo ATPase overlay the EM image of the super-complex.

The current EM data are promising, but for a better description and a higher resolution image, further EM studies are being pursued.

#### 4.5 Discussion

A rationale that can be proposed for the function of the super-complex of the mitochondrial ET chain is facilitation of the electron transfer steps involving the soluble or diffusible ET components, i.e., ubiquinone between complex I and II and complex III (the cytochrome  $bc_1$  complex), and cytochrome  $c$  between complex III and IV (cytochrome oxidase). Applying this concept to the photosynthetic electron transport chain, a structure analogy would apply to the PSI- $b_6f$  complex, connected for electron transport on the lumen side by plastocyanin [76, 77, 181]. In contrast, the majority of the super-complexes isolated thus from thylakoid membranes [68, 174-177], function solely or partly to expedite light energy transfer from the light harvesting pigment-protein complexes to the reaction centers, although some super-complexes that include the  $b_6f$  complex and the photosystem I reaction center have been obtained [75-77, 181]. The role of the ATPase and PSI reaction center, located in the stromal or stroma-exposed thylakoid membrane domains, in facilitating electron transport and energy transduction via a super-complex, is less

obvious. One inference is a function in localization and substrate channeling, for reasons of efficiency, of the electron transport reactions necessary to supply the co-factors for CO<sub>2</sub> fixation. The end products of this super-complex are ATP and NADPH, which are the sources of energy and reducing equivalents in the early steps of the carbon fixation pathway in C<sub>3</sub> plants, in which CO<sub>2</sub> is converted to glyceraldehyde-3-phosphate [185]. The presence of soluble CO<sub>2</sub>-fixing enzymes in the ATPase-PSI-FNR super-complex, although at a low level, suggests the possibility of a local domain for carbon fixation. The low abundance of these enzymes in the mass spectrophotometric analysis is attributed to the fact that they are soluble proteins.

*Dynamics in Thylakoid Membranes Underlying Super-Complexes.* The existence of multi-component multifunctional complexes of the photosynthetic apparatus suggests that it is not only the light harvesting complexes that act dynamically in the membrane, as discussed, for example, in [186]. The larger number of 'super-complexes' isolated from the grana membrane, of which the reaction center/light harvesting complexes are a major fraction, can reasonably be attributed to the larger density and crowding of the energy transducing membrane protein complexes in the grana stacks. This is inferred to cause a more restricted motion and larger cross-section for spatial interaction of the individual complexes as they diffuse in the membrane. Thus, the phenomenon of super-complex formation can be described in the context of the fluid-mosaic model [159] which first described the lateral fluid dynamic properties of membrane proteins, and the subsequent broadening of this perspective to include the formation of intra-membrane multi-component protein complexes [160].

#### **4.6 Conclusion**

A novel ~1 MDa supercomplex, dominated by the presence of PSI-ATP-synthase and FNR, has been purified and characterized from higher plant *Spinacea*. The end products of such a supercomplex are ATP and NADPH, which are the principle cofactors required for CO<sub>2</sub> fixation by the Calvin cycle. We hypothesize that the formation of this novel supercomplex serves the purpose of formation of a localized domain for expediting the channeling of the cofactors to the CO<sub>2</sub> fixation cycle. Structural characterization of the complex is being pursued currently.

## REFERENCES

- [1] Alberts B, Johnson A., Lewis, J., et al. (2002). *Molecular Biology of the Cell*. (4th edition. ed.). New York: Garland Science.
- [2] Lopez, F. B., & Barclay, G. F. (2017). Chapter 4 - Plant Anatomy and Physiology. In S. Badal & R. Delgoda (Eds.), *Pharmacognosy* (pp. 45-60). Boston: Academic Press.
- [3] Hasan, S.S., & Cramer, W. A. (2012). On rate limitations of electron transfer in the photosynthetic cytochrome b6f complex. *Physical Chemistry Chemical Physics*, 14(40), 13853-13860.
- [4] Rochaix, J.-D. (2011). Regulation of photosynthetic electron transport. *Biochimica et Biophysica Acta (BBA) - Bioenergetics*, 1807(3), 375-383.
- [5] Tikhonov, A. N. (2014a). The cytochrome b6f complex at the crossroad of photosynthetic electron transport pathways. *Plant Physiology & Biochemistry*, 81, 163-183.
- [6] Hill, R., & Bendall, F. A. Y. (1960). Function of the Two Cytochrome Components in Chloroplasts: A Working Hypothesis. *Nature*, 186 (4719), 136-137.
- [7] Dreyfuss, B. W., & Thornber, J. P. (1994). Assembly of the Light-Harvesting Complexes (LHCs) of Photosystem II (Monomeric LHC IIb Complexes Are Intermediates in the Formation of Oligomeric LHC IIb Complexes). *Plant Physiology*, 106 (3), 829.
- [8] Ishikita, H., Saenger, W., Biesiadka, J., Loll, B., & Knapp, E.-W. (2006). How photosynthetic reaction centers control oxidation power in chlorophyll pairs P680, P700, and P870. *Proceedings of the National Academy of Sciences*, 103 (26), 9855.
- [9] Trebst, A. (1978). Plastoquinones in Photosynthesis. *Philosophical Transactions of the Royal Society of London. Series B, Biological Sciences*, 284(1002), 591-599.
- [10] McEvoy, J. P., & Brudvig, G. W. (2006). Water-Splitting Chemistry of Photosystem II. *Chemical Reviews*, 106 (11), 4455-4483.
- [11] Ananyev, G., Roy-Chowdhury, S., Gates, C., Fromme, P., & Dismukes, G. C. (2019). The Catalytic Cycle of Water Oxidation in Crystallized Photosystem II Complexes: Performance and Requirements for Formation of Intermediates. *ACS Catalysis*, 9 (2), 1396-1407..
- [12] Coe, J., Kupitz, C., Basu, S., Conrad, C. E., Roy-Chowdhury, S., Fromme, R., & Fromme, P. (2015). Chapter Twenty-Two - Crystallization of Photosystem II for Time-Resolved Structural Studies Using an X-ray Free Electron Laser. In A. K. Shukla (Ed.), *Methods in Enzymology* (Vol. 557, pp. 459-482): Academic Press.

- [13] Cramer, W.A. (2019). Structure–function of the cytochrome b6f lipoprotein complex: a scientific odyssey and personal perspective, *Photosynthesis Research* 139(1) 53-65.
- [14] Barbagallo, R. P., Breyton, C., & Finazzi, G. (2000). Kinetic Effects of the Electrochemical Proton Gradient on Plastoquinone Reduction at the Q<sub>i</sub> Site of the Cytochrome b6f Complex. *Journal of Biological Chemistry*, 275(34), 26121-26127.
- [15] Joliot, P. & Johnson, G. N. (2011). Regulation of cyclic and linear electron flow in higher plants. *Proceedings of the National Academy of Sciences of the United States of America*, 108 13317-13322.
- [16] Joliot, P., & Joliot, A. (2006). Cyclic electron flow in C3 plants. *Biochimica et Biophysica Acta (BBA) - Bioenergetics*, 1757(5), 362-368.
- [17] Zhang, H., Whitelegge, J. P., & Cramer, W. A. (2001). Ferredoxin: NADP<sup>+</sup> oxidoreductase is a subunit of the chloroplast cytochrome b6f complex. *Journal of Biological Chemistry*.
- [18] Cramer, W.A. & Whitmarsh, J. (1977) Photosynthetic Cytochromes, *Annual Review of Plant Physiology* 28(1) 133-172.
- [19] Hasan, S. S., Yamashita, E., & Cramer, W. A. (2013). Transmembrane signaling and assembly of the cytochrome b6f-lipidic charge transfer complex. *Biochimica et Biophysica Acta (BBA) - Bioenergetics*, 1827(11), 1295-1308.
- [20] Cramer, W. A., Zhang, H., Yan, J., Kurisu, G., & Smith, J. L. (2006). Transmembrane Traffic in the Cytochrome b6f Complex. *Annual Review of Biochemistry*, 75(1), 769-790.
- [21] Berry, E. A., Guergova-Kuras, M., Huang, L.-s., & Crofts, A. R. (2000). Structure and Function of Cytochrome bc Complexes. *Annual Review of Biochemistry*, 69(1), 1005-1075.
- [22] Cape, J.L., Bowman, M.K. & Kramer, D.M. (2006) Understanding the cytochrome bc complexes by what they don't do. The Q-cycle at 30, *Trends in Plant Science* 11(1) 46-55.
- [23] Kallas, T. (1994). *The Cytochrome b6f Complex.*: Springer.
- [24] Bolla, J.R., Sauer, J.B., Wu,D., Mehmood, S., Allison, T.M. & Robinson CV. (2018). Direct observation of the influence of cardiolipin and antibiotics on lipid II binding to MurJ. *Nat Chem*, 10(3), 363-371.
- [25] Miliara, X., Tatsuta, T., Berry, J.L., Rouse, S.L., Solak, K., Chorev, D.S., Wu, D., Robinson, C.V., Matthews, S. & Langer T. (2019). Structural determinants of lipid specificity within Ups/PRELI lipid transfer proteins. *Nat Commun.*, 10(1130), 1-15.
- [26] Baniulis, D., Zhang, H., Zakharova, T., Hasan, S. S., & Cramer, W. A. (2011). Purification and Crystallization of the Cyanobacterial Cytochrome b6f Complex. In R. Carpentier (Ed.), *Photosynthesis Research Protocols* (pp. 65-77). Totowa, NJ: Humana Press.

- [27] Kurisu, G., Zhang, H., Smith, J. L., & Cramer, W. A. (2003). Structure of the cytochrome *b<sub>6</sub>f* complex of oxygenic photosynthesis: tuning the cavity. *Science*, 302, 1009-1014.
- [28] Hasan, S.S. & Cramer, W.A. Internal lipid architecture of the hetero-oligomeric cytochrome *b<sub>6</sub>f* complex, *Structure* 22 (2014) 1008-1015.
- [29] Stroebel, D., Choquet, Y., Popot, J.-L., & Picot, D. (2003). An atypical heme in the cytochrome *b<sub>6</sub>f* complex. *Nature*, 426, 413-418.
- [30] Yamashita, E., Zhang, H. & Cramer, W.A. (2007) Structure of the Cytochrome *b<sub>6</sub>f* Complex: Quinone Analogue Inhibitors as Ligands of Heme *c<sub>n</sub>*, *Journal of Molecular Biology* 370 (1) 39-52.
- [31] Kobayashi, K. (2016) Role of membrane glycerolipids in photosynthesis, thylakoid biogenesis and chloroplast development, *J Plant Res.* 129(4) 565–580.
- [32] Darrouzet, E., Cooley, J.W. & Daldal, F. (2004) The Cytochrome *bc<sub>1</sub>* Complex and its Homologue the *b<sub>6</sub>f* Complex: Similarities and Differences, *Photosynthesis Research* 79(1) 25-44.
- [33] Martinez, S.E., Huang, D., Szczepaniak, A., Cramer, W.A. & Smith, J.L. (1994) Crystal structure of chloroplast cytochrome *b<sub>6</sub>f* reveals a novel cytochrome fold and unexpected heme ligation, *Structure* 2(2) 95-105.
- [34] Yan, J., & Cramer, W. A. (2003). Functional Insensitivity of the Cytochrome *b<sub>6</sub>f* Complex to Structure Changes in the Hinge Region of the Rieske Iron-Sulfur Protein. *Journal of Biological Chemistry*, 278(23), 20925-20933.
- [35] Carrell, C.J., Zhang, H., Cramer, W.A. & Smith, J.L. (1997) Biological identity and diversity in photosynthesis and respiration: structure of the lumen-side domain of the chloroplast Rieske protein, *Structure* 5(12) 1613-1625.
- [36] Twigg, A.I., Baniulis, D., Cramer, W.A. & Hendrich, M.P. (2009) EPR detection of an O<sub>2</sub> surrogate bound to heme *c<sub>n</sub>* of the cytochrome *b<sub>6</sub>f* complex, *J. Am. Chem. Soc.* 131(35) 12536-12537.
- [37] Zhang, H., Huang, D. & Cramer, W.A. (1999) Stoichiometrically Bound  $\beta$ -Carotene in the Cytochrome *b<sub>6</sub>f* Complex of Oxygenic Photosynthesis Protects against Oxygen Damage, *Journal of Biological Chemistry* 274(3) 1581-1587.
- [38] Dashdorj, N., Zhang, H., Kim, H., Yan, J., Cramer, W.A. & Savikhin, S. (2005) The Single Chlorophyll *a* Molecule in the Cytochrome *b<sub>6</sub>f* Complex: Unusual Optical Properties Protect the Complex against Singlet Oxygen, *Biophysical Journal* 88(6) 4178-4187.
- [39] Kim, H., Dashdorj, N., Zhang, H., Yan, J., Cramer, W.A. & Savikhin, S. (2005) An Anomalous Distance Dependence of Intraprotein Chlorophyll-Carotenoid Triplet Energy Transfer, *Biophysical Journal* 89(4) L28-L30.

- [40] Crofts, A. R. (2004). The Cytochrome bc<sub>1</sub> Complex: Function in the Context of Structure. *Annual Review of Physiology*, 66(1), 689-733.
- [41] Hurt, E. C., Gabellini, N., Shahak, Y., Lockau, W., & Hauska, G. (1983). Extra proton translocation and membrane potential generation—Universal properties of cytochrome bc<sub>1</sub>b<sub>6</sub>f complexes reconstituted into liposomes. *Archives of Biochemistry and Biophysics*, 225(2), 879-885.
- [42] Zhang, Z., Huang, L., Shulmeister, V. M., Chi, Y.-I., Kim, K. K., Hung, L.-W., . . . Kim, S.-H. (1998). Electron transfer by domain movement in cytochrome bc<sub>1</sub>. *Nature*, 392(6677), 677-684.
- [43] Cramer, W. A. and S. Saif Hasan (2016) The Cytochrome b<sub>6</sub>f Lipoprotein Complex; pp. 177-207 in “Cytochrome Complexes: Evolution, Structures, Energy Transduction, and Signaling,” Eds. Govindjee and T. Sharkey (Springer, Dordrecht), volume 41 in the Series "Adv. in Photosynthesis and Respiration,” eds. Govindjee and T. Sharkey" (Springer, Dordrecht)
- [44] Cramer, W. A., Hasan, S. S., & Yamashita, E. (2011). The Q cycle of cytochrome bc complexes: a structure perspective. *Biochim Biophys Acta*, 1807(7), 788-802.
- [45] Girvin, M.E. & Cramer, W.A. (1984) A redox study of the electron transport pathway responsible for generation of the slow electrochromic phase in chloroplasts, *Biochimica et Biophysica Acta (BBA) - Bioenergetics* 767(1) 29-38.
- [46] Furbacher, P. N., Girvin, M. E., & Cramer, W. A. (1989). On the question of interheme electron transfer in the chloroplast cytochrome b<sub>6</sub> *in situ*. *Biochemistry*, 28, 8990-8998.
- [47] Contreras, F.-X., Ernst, A. M., Wieland, F., & Brügger, B. (2011). Specificity of Intramembrane Protein–Lipid Interactions. *Cold Spring Harbor Perspectives in Biology*, 3(6)
- [48] Hunte, C. & Richers, S. (2008) Lipids and membrane protein structures, *Current opinion in structural biology* 18(4), 406-411
- [49] Sedlak, E., Varha, R., Musatov, A., & Robinson, N.C. (2014). The Kinetic Stability of Cytochrome c Oxidase: Effect of Bound Phospholipid and Dimerization. *Biophysical Journal*, 107, 2941-2949.
- [50] Adamian, L., Naveed, H., & Liang, J. (2011). Lipid-binding surfaces of membrane proteins: Evidence from evolutionary and structural analysis. *Biochimica et Biophysica Acta (BBA) - Biomembranes*, 1808(4), 1092-1102.
- [51] Zhang, H., Kurisu, G., Smith, J.L. & Cramer, W.A. (2003) A defined protein–detergent–lipid complex for crystallization of integral membrane proteins: The cytochrome b<sub>6</sub>f complex of oxygenic photosynthesis, *Proceedings of the National Academy of Sciences* 100(9) 5160.

- [52] Nussberger, S., Dörr, K., Wang, D. N., & Kühlbrandt, W. (1993). Lipid-protein Interactions in Crystals of Plant Light-harvesting Complex. *Journal of Molecular Biology*, 234(2), 347-356.
- [53] Cartailier, J.-P., & Luecke, H. (2003). X-Ray Crystallographic Analysis of Lipid-Protein Interactions in the Bacteriorhodopsin Purple Membrane. *Annual Review of Biophysics and Biomolecular Structure*, 32(1), 285-310.
- [54] Escribá, P. V., Wedegaertner, P. B., Goñi, F. M., & Vögler, O. (2007). Lipid-protein interactions in GPCR-associated signaling. *Biochimica et Biophysica Acta (BBA) - Biomembranes*, 1768(4), 836-852.
- [55] Hite, R. K., Li, Z., & Walz, T. (2010). Principles of membrane protein interactions with annular lipids deduced from aquaporin-0 2D crystals. *The EMBO journal*, 29(10), 1652-1658.
- [56] Matthies, D., Bae, C., Toombes, G. E. S., Fox, T., Bartesaghi, A., Subramaniam, S., & Swartz, K. J. (2018). Single-particle cryo-EM structure of a voltage-activated potassium channel in lipid nanodiscs. *eLife*, 7, e37558. Retrieved from <https://doi.org/10.7554/eLife.37558>. doi:10.7554/eLife.37558
- [57] Gupta K, D. J., Hopper J.T.S., Uzdaviny, P., Landreh, M., Struwe, W.B., Drew, D., Baldwin, A.J., Stansfeld, P.J. & Robinson CV. (2017). The role of interfacial lipids in stabilizing membrane protein oligomers. *Nature*, 541(7637), 421-424.
- [58] Laganowsky, A., Reading, E., Allison, T. M., Ulmschneider, M. B., Degiacomi, M. T., Baldwin, A. J., & Robinson, C. V. (2014). Membrane proteins bind lipids selectively to modulate their structure and function. *Nature*, 510 (7503), 172-175.
- [59] Bolla, J. R., Agasid, M. T., Mehmood, S., & Robinson, C. V. (2019). Membrane Protein-Lipid Interactions Probed Using Mass Spectrometry. *Annual Review of Biochemistry*.
- [60] Hunte, C., Koepke, J., Lange, C., Rossmann, T., & Michel, H. (2000). Structure at 2.3 Å resolution of the cytochrome *bc*<sub>1</sub> complex from the yeast *Saccharomyces cerevisiae* with an antibody Fv fragment. *Struct. Fold Des.*, 8, 669-684.
- [61] Hasan, S. S., Yamashita, E., Ryan, C. M., Whitelegge, J. P., & Cramer, W. A. (2011). Conservation of lipid functions in cytochrome *bc* complexes. *Journal of Molecular Biology*, 414(1), 145-162.
- [62] Pfeiffer, K., Gohil, V., Stuart, R. A., Hunte, C., Brandt, U., Greenberg, M. L., & Schagger, H. (2003). Cardiolipin Stabilizes Respiratory Chain Supercomplexes. *Journal of Biological Chemistry*, 278(52), 52873-52880.
- [63] Mileykovskaya, E., & Dowhan, W. (2014). Cardiolipin-dependent formation of mitochondrial respiratory supercomplexes. *Chemistry and Physics of Lipids*, 179, 42-48.

- [64] Zhang, M., Mileykovskaya, E., & Dowhan, W. (2002). Gluing the respiratory chain together: Cardiolipin is required for supercomplex formation in the inner mitochondrial membrane. *Journal of Biological Chemistry*, 277(46), 43553-43556.
- [65] Hasan, S. S., Zakharov, S. D., Chauvet, A., Stadnytskyi, V., Savikhin, S., & Cramer, W. A. (2014). A map of dielectric heterogeneity in a membrane protein: the hetero-oligomeric cytochrome b6/f complex. *The journal of physical chemistry. B*, 118(24), 6614-6625.
- [66] Wenz, T., Heilscher, R., Hellwig, P., Schagger, H., Richers, S., & Hunte, C. (2009). Role of phospholipids in respiratory cytochrome bc1 complex catalysis and supercomplex formation. *Biochim. Biophys. Acta*, 1787, 609-616.
- [67] Allen, J. F. (1992). Protein phosphorylation in regulation of photosynthesis. *Biochimica et Biophysica Acta (BBA) - Bioenergetics*, 1098(3), 275-335.
- [68] Mazor, Y., Borovikova, A., Caspy, I., & Nelson, N. (2017). Structure of the plant photosystem I supercomplex at 2.6 Å resolution. *Nature Plants*, 3, 17014.
- [69] Qin, X., Suga, M., Kuang, T., & Shen, J.-R. (2015). Structural basis for energy transfer pathways in the plant PSI-LHCI supercomplex. *Science*, 348(6238), 989.
- [70] Albanese, P., Melero, R., Engel, B. D., Grinzato, A., Berto, P., Manfredi, M., & Pagliano, C. (2017). Pea PSII-LHCII supercomplexes form pairs by making connections across the stromal gap. *Scientific Reports*, 7(1), 10067.
- [71] Wei, X., Shen, X., Cao, P., Liu, X., Chang, W., Li, M., Zhang, X., & Z. Liu. (2016). Structure of spinach photosystem II-LHCII supercomplex at 3.2 Å resolution. *Nature*, 534, 69-74.
- [72] Pan, X., Ma, J., Su, X., Cao, P., Chang, W., Liu, Z., . . . Li, M. (2018). Structure of the maize photosystem I supercomplex with light-harvesting complexes I and II. *Science*, 360(6393), 1109.
- [73] Semchonok, D. A., Sathish Yadav, K. N., Xu, P., Drop, B., Croce, R., & Boekema, E. J. (2017). Interaction between the photoprotective protein LHCSR3 and C2S2 Photosystem II supercomplex in *Chlamydomonas reinhardtii*. *Biochimica et Biophysica Acta (BBA) - Bioenergetics*, 1858(5), 379-385.
- [74] Tokutsu, R., & Minagawa, J. (2013). Energy-dissipative supercomplex of photosystem II associated with LHCSR3 in *Chlamydomonas reinhardtii*. *Proceedings of the National Academy of Sciences*, 110(24), 10016.
- [75] Steinbeck, J., Ross, I. L., Rothnagel, R., Gäbelein, P., Schulze, S., Giles, N., . . . Hankamer, B. (2018). Structure of a PSI-LHCI-cyt b6/f supercomplex in *Chlamydomonas reinhardtii*; promoting cyclic electron flow under anaerobic conditions. *Proceedings of the National Academy of Sciences*, 115(41), 10517.

- [76] Iwai, M., Takizawa, K., Tokutsu, R., Okamuro, A., Takahashi, Y. & Minagawa, J. (2010). Isolation of the supercomplex that drives cyclic electron flow in photosynthesis *Nature*, *464*, 1210-1213.
- [77] Yadav, K.N., Semchonok, D. A., Nosek, L., Kouril, R., Fucile, G., Boekema, E.J. & Eichacker, L.A. (2017). Supercomplexes of plant photosystem I with cytochrome b6f, light-harvesting complex II and NDH. *Biochim Biophys Acta*, *1858* 12-20
- [78] Gao, F., Zhao, J., Chen, L., Battchikova, N., Ran, Z., Aro, E.-M., . . . Ma, W. (2016). The NDH-1L-PSI Supercomplex Is Important for Efficient Cyclic Electron Transport in Cyanobacteria. *Plant physiology*, *172*(3), 1451-1464.
- [79] Amunts, A., Drory, O. & Nelson, N. (2007). The structure of a plant photosystem I supercomplex at 3.4 Å resolution. *Nature*, *447*, 58-63.
- [80] Nelson, N., & Yocum, C. F. (2006). Structure And Function Of Photosystems I And II. *Annual Review of Plant Biology*, *57*(1), 521-565.
- [81] Junge, W., & Nelson, N. (2015). ATP Synthase. *Annual Review of Biochemistry*, *84*(1), 631-657.
- [82] Hahn, A., Vonck, J., Mills, D. J., Meier, T., & Kühlbrandt, W. (2018). Structure, mechanism, and regulation of the chloroplast ATP synthase. *Science*, *360*(6389), eaat4318.
- [83] Siegenthaler, P. A. & Murata, N. (1998). *Lipids in Photosynthesis: Structure, Function, and Genetics*. London, UK Kluwer Academic Publishers.
- [84] Sakurai, I., Shen, J.R., Leng, J., Ohashi, S., Kobayashi, M. and Wada, H. (2006). Lipids in oxygen-evolving photosystem II complexes of cyanobacteria and higher plants. *J. Biochem.*, *140* (2), 201-209.
- [85] Umena, Y., Kawakami, K., Shen, J.R. & Kamiya, N. (2011). Crystal structure of oxygen-evolving photosystem II at a resolution of 1.9 Å. *Nature*, *473* 55-60.
- [86] Jordan, P., Fromme, P., Witt, H.T., Klukas, O., Saenger, W. & Krauss, N. (2001). Three-dimensional structure of cyanobacterial photosystem I at 2.5 Å resolution. *Nature*, *411* 909-917.
- [87] Guskov, A., Kern, J., Gabdulkhakov, A., Broser, M., Zouni, A. & Saenger, W. (2009). Cyanobacterial photosystem II at 2.9 Å resolution and the role of quinones, lipids, channels and chloride. *Nat. Struct. Mol. Biol.*, *16*, 334-342.
- [88] Aronsson H., Schottler, M. A., Kelly, A.A., Sundqvist, C., Dörmann, P. Karim. S & Jarvis, P. (2008). Monogalactosyldiacylglycerol deficiency in Arabidopsis affects pigment composition in the prolamellar body and impairs thylakoid membrane energization and photoprotection in leaves. *Plant Physiol.*, *148*(1), 580-592.

- [89] Hölzl, G, Witt, S., Gaude, N., Melzer, M., Schöttler, M.A. & Dörmann P. (2009). The role of diglycosyl lipids in photosynthesis and membrane lipid homeostasis in Arabidopsis.. *Plant Physiol.*, 150(3), 1147-1159.
- [90] Droppa, M., Horvath, G., Hideg, E & Farkas, T. (1995). The role of phospholipids in regulating photosynthetic electron transport activities: Treatment of thylakoids with phospholipase C. *Photosynth Res.*, 46(1-2), 287-293.
- [91] Jordan, B.R., Chow, W. & Baker AJ.(1983). The role of phospholipids in the molecular organisation of pea chloroplast membranes; Effect of phospholipid depletion on photosynthetic activities. *Biochim Biophys Acta.*, 725, 77–86.
- [92] Minoda, A., Sato, N., Nozaki, H., Okada, K., Takahashi, H., Sonoike, K. & Tsuzuki M. (2002). Role of sulfoquinovosyl diacylglycerol for the maintenance of photosystem II in *Chlamydomonas reinhardtii*. *Eur J Biochem.*, 269(9), 2353-2358.
- [93] Aoki, M., Sato,N., Meguro, A. & Tsuzuki M (2004). Differing involvement of sulfoquinovosyl diacylglycerol in photosystem II in two species of unicellular cyanobacteria. . *Eur J Biochem.*, 271, 685–693.
- [94] Hasan, S. S., Stofleth, J. T., Yamashita, E., & Cramer, W. A. (2013). Lipid-Induced Conformational Changes within the Cytochrome b6f Complex of Oxygenic Photosynthesis. *Biochemistry*, 52(15), 2649-2654.
- [95] Palsdottir, H. & Hunte, C. (2004). Lipids in membrane protein structures. *BBA-Biomembranes*, 1666(1-2), 2-18.
- [96] Lee, A. G. (2004). How lipids affect the activities of integral membrane proteins. *BBA-Biomembranes*, 1666, 62-87.
- [97] van Eerdena, F. J., de Jong,D.H., deVriesa, A.H.,Wassenaarc,T.A. & Marrink,S.J. (2015). Characterization of thylakoid lipid membranes from cyanobacteria andhigher plants by molecular dynamics simulations. *BBA-Biomembranes*, 1848, 1390-1330
- [98] Zhang, H., & Cramer, W. A. (2004). Purification and Crystallization of the Cytochrome b6f Complex in Oxygenic Photosynthesis. In R. Carpentier (Ed.), *Photosynthesis Research Protocols* (pp. 67-78). Totowa, NJ: Humana Press.
- [99] Schneider, C. A., Rasband, W.S. & Eliceiri, K.W.(2012). NIH Image to ImageJ: 25 years of image analysis. *Nature Methods*, 9, 671-675.
- [100] Abramoff, M. D., Magalhaes, P.J. & Ram, S.J. (2004). Image Processing with ImageJ. *Biophotonics International.*, 11(7), 36-42.
- [101] Dominik, P K., Borowska, M.T., Dalmas, O., Kim, Sangwoo S., Perozo, E., Keenan, R.J., & Kossiakoff, Anthony A. (2016). Conformational Chaperones for Structural Studies of Membrane Proteins Using Antibody Phage Display with Nanodiscs. *Structure*, 24(2), 300-309.

- [102] Baniulis, D., Hasan, S. S., Stofleth, J.T. & Cramer, W. A. (2013 ). Mechanism of enhanced superoxide production in the cytochrome b(6)f complex of oxygenic photosynthesis. *Biochemistry*, 52(50), 8975-8983.
- [103] Dębski,D., Smulik,R., Zielonka,J., Michałowski,B.,Jakubowska,M., Dębowska,K., Adamus,J., Marcinek,A., Kalyanaraman,B. & Sikora,A., Mechanism of oxidative conversion of Amplex® Red to resorufin: pulse radiolysis and enzymatic studies, *Free Radic Biol Med* 95 (2016) 323-332.
- [104] Holzwarth, G. & Doty, P. (1965) The ultraviolet circular dichroism of polypeptides., *J Am Chem Soc.* 87, 218-228.
- [105] Greenfield, N. J., & Fasman, G. D. (1969). Computed circular dichroism spectra for the evaluation of protein conformation. *Biochemistry*, 8(10), 4108-4116.
- [106] Grinkova, Y. V., Denisov, I.G & Sligar S.G. (2010). Engineering extended membrane scaffold proteins for self-assembly of soluble nanoscale lipid bilayers. *Protein Eng Des Sel.*, 23(11), 843-848.
- [107] Denisov, I. G., Grinkova, Y.V., Lazarides, A. A. & Sligar, S.G. (2004). Directed Self-Assembly of Monodisperse Phospholipid Bilayer Nanodiscs with Controlled Size. *J. Am. Chem. Soc.*, 126(11), 3477–3487.
- [108] C.F. McKibbin, N.A.; Jeans,C.; Reeves,P.J.; Khorana,H.G.; Wallace,B.A.; Edwards,P.C.; Villa,C.; Booth,P.J., Opsin stability and folding: modulation by phospholipid bicelles., *J Mol Biol* 374(5) (2007) 1319-32.
- [109] Chang, Y-C. & Bowie, J.U. (2014). Measuring membrane protein stability under native conditions. *Proc.Natl.Acad.Sci.USA*, 111(1), 219-224.
- [110] Morrison, E. A. & Henzler-Weissman, K.A. (2012). Reconstitution of integral membrane proteins into isotropic bicelles with improved sample stability and expanded lipid composition profile. *BBA-Biomembranes*, 1818(2), 814-820.
- [111] de Vitry, C. Ouyang, Y., Finazzi,G., Wollman,F.A. & Kallas,T. (2004). The chloroplast Rieske iron-sulfur protein. At the crossroad of electron transport and signal transduction. *J Biol Chem*, 271(43), 44621-44627.
- [112] Agarwal, R., Hasan, S.S., Jones, L.M., Stofleth, J.T., Ryan, C.M., Whitelegge, J.P., Kehoe, D.M. & Cramer,W.A. (2015). Role of Domain Swapping in the Hetero-Oligomeric Cytochrome b6f Lipoprotein Complex. *Biochemistry*, 54(20), 3151-3163.
- [113] Hagio, M., Gombos, Z., Várkonyi, Z., Masamoto,K., Sato,N., Tsuzuki,M. & Wada, H. (2000). Direct Evidence for Requirement of Phosphatidylglycerol in Photosystem II of Photosynthesis. *Plant Physiol.*, 124(2).

- [114] Sato, N. H., M.; Wada, H. and Tsuzuki, M. (2000). Requirement of phosphatidylglycerol for photosynthetic function in thylakoid membranes. *Proc. Natl. Acad. Sci. USA*, 97(19), 10655-10660.
- [115] Kobayashi, K., Endo, K., Wada, H. (2016). Multiple Impacts of Loss of Plastidic Phosphatidylglycerol Biosynthesis on Photosynthesis during Seedling Growth of Arabidopsis. *Front Plant Sci*, 7, 336.
- [116] Gomez, B., Jr. & Robinson, N.C. (1999). Phospholipase digestion of bound cardiolipin reversibly inactivates bovine cytochrome bc1. *Biochemistry*, 38(28), 9031-9038.
- [117] Sakurai, I. H., M.; Gombos, Z.; Tyystjarvi, T.; Paakkarinen, V.; Aro, E.M. and Wada, H. (2003). Requirement of phosphatidylglycerol for maintenance of photosynthetic machinery. *Plant Physiol.*, 133(3), 1376-1384.
- [118] Xia, D., Yu, C.-A., Kim, H., Xia, J.-Z., Kachurin, A. M., Zhang, L., . . . Deisenhofer, J. (1997). Crystal Structure of the Cytochrome bc1 Complex from Bovine Heart Mitochondria. *Science*, 277(5322), 60-66.
- [119] Yang, Y., Ying, S., Yu, L. & Yu, C.A. (2010). Reaction Mechanism of Superoxide Generation during Ubiquinol Oxidation by the Cytochrome bc1 Complex. *J Biol Chem*, 285(22), 17038-17045.
- [120] Bhaduri, S., Stadnytskyi, V., Zakharov, S.D., Hasan, S.S., Bujnowicz, L., Sarewicz, M., Savikhin, S., Osyczka, A. and Cramer W.A. (2017). Pathways of Transmembrane Electron Transfer in Cytochrome bc Complexes: Dielectric Heterogeneity and Interheme Coulombic Interactions. *Journal of Physical Chemistry B*, 121(5), 975-983.
- [121] Warshel, A., & Aqvist, J. (1991). Electrostatic energy and macromolecular function. *Annual review of biophysics and biophysical chemistry*, 20, 267-298.
- [122] Chamorovsky, S. K., Cherepanov, D. A., Chamorovsky, C. S., & Semenov, A. Y. (2007). Correlation of electron transfer rate in photosynthetic reaction centers with intraprotein dielectric properties. *Biochimica Et Biophysica Acta*, 1767(6), 441-448.
- [123] Steffen, M. A., Lao, K., & Boxer, S. G. (1994). Dielectric asymmetry in the photosynthetic reaction center. *Science*, 264(5160), 810-816.
- [124] Pushenko, V. V., Cherepanov, D.A., and Krishtalik, L.I. (2015). Electrostatics of the photosynthetic bacterial reaction center. Protonation of Glu L 212 and Asp L 213 — A new method of calculation. *Biochim. Biophys. Acta*, 1767, 441-448.
- [125] Krishtalik, L. I. (1999). Role of the protein's low dielectric constant in the functioning of the photosynthetic reaction center. *Photosyn. Res.*, 60, 241-246.
- [126] Garczarek, F., Brown, L. S., Lanyi, J. K., & Gerwert, K. (2005). Proton binding within a membrane protein by a protonated water cluster. *Proc Natl Acad Sci U S A*, 102(10), 3633-3638.

- [127] Iwata, T., Paddock, M. L., Okamura, M. Y., & Kandori, H. (2009). Identification of FTIR bands due to internal water molecules around the quinone binding sites in the reaction center from *Rhodobacter sphaeroides*. *Biochemistry*, *48*(6), 1220-1229.
- [128] Guan, L., Mirza, O., Verner, G., Iwata, S., & Kaback, H. R. (2007). Structural determination of wild-type lactose permease. *Proc Natl Acad Sci U S A*, *104*(39), 15294-15298.
- [129] Esser, L., Elberry, M., Zhou, F., Yu, C. A., Yu, L., & Xia, D. (2008). Inhibitor-complexed structures of the cytochrome *bc<sub>1</sub>* from the photosynthetic bacterium *Rhodobacter sphaeroides*. *J. Biol. Chem.*, *283*(5), 2846-2857.
- [130] Esser, L., Quinn, B., Li, Y. F., Zhang, M., Elberry, M., Yu, L., . . . Xia, D. (2004). Crystallographic studies of quinol oxidation site inhibitors: a modified classification of inhibitors for the cytochrome *bc<sub>1</sub>* complex. *J. Mol. Biol.*, *341*(1), 281-302.
- [131] Kao, W. C., & Hunte, C. (2014). The molecular evolution of the Qo motif. *Genome Biol Evol*, *6*(7), 1894-1910.
- [132] Dashdorj, N., Xu, W., Martinsson, P., Chitnis, P. R., & Savikhin, S. (2004). Electrochromic shift of chlorophyll absorption in photosystem I from *Synechocystis* sp. PCC 6803: a probe of optical and dielectric properties around the secondary electron acceptor. *Biophys J*, *86*(5), 3121-3130.
- [133] Pintscher, S., Kuleta, P., Cieluch, E., Borek, A., Sarewicz, M. & Osyczka, A. (2016). Tuning of hemes b equilibrium redox potential is not required for cross-membrane electron transfer. *Journal of Biological Chemistry*, *291*(13), 6872-6881.
- [134] Swierczek, M., Cieluch, E., Sarewicz, M., Borek, A., Moser, C. C., Dutton, P. L., & Osyczka, A. (2010). An electronic bus bar lies in the core of cytochrome *bc<sub>1</sub>*. *Science*, *329*(5990), 451-454.
- [135] Lanciano, P., Lee, D.W., Yang, H., Darrouzet, E., Daldal, F. (2011). Intermonomer electron transfer between the low-potential b hemes of cytochrome *bc<sub>1</sub>*. *Biochemistry*, *50*(10), 1651-1663.
- [136] Palmer, G., & Degli Esposti, M. (1994). Application of exciton coupling theory to the structure of mitochondrial cytochrome *b*. *Biochemistry*, *33*(1), 176-185.
- [137] Valkova-Valchanova, M. B., Saribas, A. S., Gibney, B. R., Dutton, P. L., & Daldal, F. (1998). Isolation and characterization of a two-subunit cytochrome *b-c<sub>1</sub>* subcomplex from *Rhodobacter capsulatus* and reconstitution of its ubihydroquinone oxidation (Qo) site with purified Fe-S protein subunit. *Biochemistry*, *37*(46), 16242-16251.
- [138] Osyczka, A., Dutton, P. L., Moser, C. C., Darrouzet, E., & Daldal, F. (2001). Controlling the functionality of cytochrome *c(1)* redox potentials in the *Rhodobacter capsulatus* *bc(1)* complex through disulfide anchoring of a loop and a beta-branched amino acid near the heme-ligating methionine. *Biochemistry*, *40*(48), 14547-14556.

- [139] Sarewicz, M., Borek, A., Daldal, F., Froncisz, W., & Osyczka, A. (2008). Demonstration of short-lived complexes of cytochrome c with cytochrome bc1 by EPR spectroscopy: implications for the mechanism of interprotein electron transfer. *J Biol Chem*, 283(36), 24826-24836.
- [140] Sarewicz, M., Borek, A., Cieluch, E., Swierczek, M., & Osyczka, A. (2010). Discrimination between two possible reaction sequences that create potential risk of generation of deleterious radicals by cytochrome bc(1). Implications for the mechanism of superoxide production. *Biochimica Et Biophysica Acta*, 1797(11), 1820-1827.
- [141] Wittig, I., Karas, M., & Schagger, H. (2007). High resolution clear native electrophoresis for in-gel functional assays and fluorescence studies of membrane protein complexes. *Molecular & cellular proteomics : MCP*, 6(7), 1215-1225.
- [142] Winn, M. D., Ballard, C. C., Cowtan, K. D., Dodson, E. J., Emsley, P., Evans, P. R., . . . Wilson, K. S. (2011). Overview of the CCP4 suite and current developments. *Acta crystallographica. Section D, Biological crystallography*, 67(Pt 4), 235-242.
- [143] Gray, H. B. & Winkler, J.R. (1996). Electron transfer in proteins. *Annual review of biophysics and biophysical chemistry*, 65, 537-562.
- [144] Chauvet, A. A. P., Haddad, A.A., Kao, W.C., Mourik, F.V., Hunte, C. & Chergui, M. (2015). Photo-induced dynamics of the heme centers in cytochrome bc1. *Phys. Chem. Chem.Phys*, 17, 2143-2151.
- [145] Baymann, F., Robertson, D. E., Dutton, P. L., & Mantele, W. (1999). Electrochemical and spectroscopic investigations of the cytochrome bc1 complex from *Rhodobacter capsulatus*. *Biochemistry*, 38(40), 13188-13199.
- [146] Hsu, M. C., & Woody, R. W. (1971). The origin of the heme Cotton effects in myoglobin and hemoglobin. *J Am Chem Soc*, 93(14), 3515-3525.
- [147] Nagai, M., Kobayashi, C., Nagai, Y., Imai, K., Mizusawa, N., Sakurai, H., . . . Nagatomo, S. (2015). Involvement of propionate side chains of the heme in circular dichroism of myoglobin: experimental and theoretical analyses. *The journal of physical chemistry. B*, 119(4), 1275-1287.
- [148] Blauer, G., Sreerama, N., Woody, R.W. (1993). Optical activity of hemoproteins in the Soret region. Circular dichroism of the heme undecapeptide of cytochrome c in aqueous solution. *Biochemistry*, 32(26), 6674-6679.
- [149] Huang, X., Nakanishi, K., & Berova, N. (2000). Porphyrins and metalloporphyrins: versatile circular dichroic reporter groups for structural studies. *Chirality*, 12(4), 237-255.
- [150] Robertson, D. E., Ding, H., Chelminski, P. R., Slaughter, C., Hsu, J., Moomaw, C., . . . Dutton, P. L. (1993). Hydroquinone-cytochrome c<sub>2</sub> oxidoreductase from *Rhodobacter capsulatus*: definition of a minimal, functional isolated preparation. *Biochemistry*, 32(5), 1310-1317.

- [151] Lambeth, D. O. & Palmer, G. (1973). The Kinetics and Mechanism of Reduction of Electron Transfer Proteins and Other Compounds of Biological Interest by Dithionite. *Journal of Biological Chemistry*, 248(17), 6095-6103.
- [152] Alric, J., Pierre, Y., Picot, D., Lavergne, J., & Rappaport, F. (2005). Spectral and redox characterization of the heme  $c_i$  of the cytochrome  $b_6f$  complex. *Proc. Nat. Acad. Sci. USA*, 102(44), 15860-15865.
- [153] Nelson, M. E., Finazzi, G., Wang, Q. J., Middleton-Zarka, K. A., Whitmarsh, J., & Kallas, T. (2005). Cytochrome  $b_6$  arginine 214 of *Synechococcus sp.* PCC 7002, a key residue for quinone-reductase site function and turnover of the cytochrome  $bf$  complex. *J. Biol. Chem.*, 280(11), 10395-10402.
- [154] Zatsman, A. I., Zhang, H., Gunderson, W. A., Cramer, W. A., & Hendrich, M. P. (2006). Heme-heme interactions in the cytochrome  $b_6f$  complex: EPR spectroscopy and correlation with structure. *J. Amer. Chem. Soc.*, 128, 14246-14247.
- [155] Rich, P. R., Madgwick, S. A., & Moss, D. A. (1991). The interactions of duroquinol, DBMIB, and NQNO with the chloroplast cytochrome  $bf$  complex. *Biochim. Biophys. Acta*, 1058, 312-328.
- [156] Kramer, D. M., & Crofts, A. R. (1994). Re-examination of the properties and function of the  $b$  cytochromes of the thylakoid cytochrome  $bf$  complex. *Biochim. Biophys. Acta*, 1184, 193-201.
- [157] Kassner, R. J. (1972). Effects of nonpolar environments on the redox potentials of heme complexes. *Proc Natl Acad Sci U S A*. 1972;69(8):2263-2267.
- [158] Widger, W. R., Cramer, W.A., Herrmann, R.G. & Trebst, A. (1984). Sequence homology and structural similarity between cytochrome  $b$  of mitochondrial complex III and the chloroplast  $b_6-f$  complex: position of the cytochrome  $b$  hemes in the membrane. *Proc Natl Acad Sci U S A*, 81(3), 674-678.
- [159] Singer, S.J. & Nicholson, G. L. (1972). The fluid mosaic model of the structure of cell membranes. *Science*, 175 720-731.
- [160] Engelman, D. M. (2005). Membranes are more mosaic than fluid. *Nature*, 438, 578-580.
- [161] Althoff, T., Mills, D. J., Popot, J. L., & Kühlbrandt, W. (2011). Arrangement of electron transport chain components in bovine mitochondrial supercomplex I1III2IV1. *The EMBO Journal*, 30(22), 4652.
- [162] Genova, M. L., & Lenaz, G. (2014). Functional role of mitochondrial respiratory supercomplexes. *Biochimica et Biophysica Acta (BBA) - Bioenergetics*, 1837(4), 427-443.
- [163] Schäfer, E., Seelert, H., Reifschneider, N. H., Krause, F., Dencher, N. A., & Vonck, J. (2006). Architecture of Active Mammalian Respiratory Chain Supercomplexes. *Journal of Biological Chemistry*, 281(22), 15370-15375.

- [164] Gu, J., Wu, M., Guo, R., Yan, K., Lei, J., Gao, N., & Yang, M. (2016). The architecture of the mammalian respirasome. *Nature*, *537*, 639.
- [165] Kuhlbrandt, W. (2015). Structure and function of mitochondrial membrane protein complexes. *BMC Biol*, *13*, 89.
- [166] Letts, J.A., Fiedorczuk, K. & Sazanov, L. A. (2016). The architecture of respiratory supercomplexes. *Nature*, *537*, 644-648.
- [167] Wu, M., Jinke, G., Guo, R., Huang, Y. & Yang, V. (2016). Structure of Mammalian Respiratory Supercomplex I1III2IV1. *Cell*, *167*, 1598-1609.
- [168] Hasan, S. S., Yamashita, E., Baniulis, D., & Cramer, W. A. (2013). Quinone-dependent proton transfer pathways in the photosynthetic cytochrome b6f complex. *Proc. Natl. Acad. Sci., U. S. A.*, *110*, 4297-4302.
- [169] Groth, G. & Pohl, E. (2001). The structure of the chloroplast F1-ATPase at 3.2 Å resolution. *The Journal of biological chemistry*, *276*, 1345-1352.
- [170] Simpson, D.J. & Von Wettstein, D. The structure and function of the thylakoid membrane, *Carlsberg Research Communications* 54(2) (1989) 55.
- [171] Anderson, J. M. (2012). Lateral heterogeneity of plant thylakoid protein complexes: early reminiscences. *Philos Trans R Soc Lond B Biol Sci*, *367* 3384-3388.
- [171] Dekker, J.P. & Boekema, E. J.(2005). Supramolecular organization of thylakoid membrane proteins in green plants. *Biochim Biophys Acta*, *1706* 12-39.
- [173] Jansson, S. (1999). A guide to the Lhc genes and their relatives in Arabidopsis. *Trends Plant Sci*, *4* 236-240.
- [174] Kouril, R., Dekker, J. P. & Boekema, E.J. (2012). Supramolecular organization of photosystem II in green plants. *Biochim Biophys Acta*, *1817*, 2-12.
- [175] Minagawa, J. & Takahashi, Y. (2004). Structure, function and assembly of Photosystem II and its light-harvesting proteins. *Photosynthesis research*, *82* 241-263.
- [176]A. Crepin, Santabarbara, S. & Caffarri, S. (2016). Biochemical and Spectroscopic Characterization of Highly Stable Photosystem II Supercomplexes from Arabidopsis. *The Journal of biological chemistry*, *291*, 19157-19171.
- [177] van Bezouwen, L. S., Caffarri, S., Kale, R. S., Kouril, R., Thunnissen, A.W.H., Oostergetel, G. T. & Boekema, E. J. (2017). Subunit and chlorophyll organization in the plant photosystem II supercomplex. *Nature Plants*, *3* 17080.
- [178] Wei, X., Shen, X., Cao, P., Liu, X., Chang, W., Li, M. Zhang, X. & Z. Liu. (2016). Structure of spinach photosystem II-LHCII supercomplex at 3.2 Å resolution. *Nature*, *534*, 69-74.

- [179] Johnson, M.P. Vasilev, C. , Olsen, J.D. & Hunter, C.N. (2014). Nanodomains of cytochrome b6f and photosystem II complexes in spinach grana thylakoid membranes. *Plant Cell*, 26 3051-3061.
- [180] Kirchhoff, H., Lee, M. & Puthiyaveetil, S. (2017). Sublocalization of Cytochrome b6f Complexes in Photosynthetic Membranes. *Trends Plant Sci.*, 22 (7), 574-582
- [181] Szyszka-Mroz,B., Pittock, P., Ivanov,A.G., Lajoie, G. & Huner, N.P. (2015). The Antarctic Psychrophile *Chlamydomonas* sp. UWO 241 Preferentially Phosphorylates a Photosystem I-Cytochrome b6/f Supercomplex. *Plant physiology*, 169, 717-736.
- [182] Kaftan, D., Brumfeld, V., Nevo, R., Scherz, A. & Reich, Z. (2002). From chloroplasts to photosystems: in situ scanning force microscopy on intact thylakoid membranes. *The EMBO journal*, 21, 6146-6153.
- [183] Puthiyaveetil, S., Tsabari, O., Lowry, T., Lenhert, S., Lewis, R.R., Reich, Z. & Kirchhoff, H. (2014). Compartmentalization of the protein repair machinery in photosynthetic membranes. *Proceedings of the National Academy of Sciences of the United States of America*, 111, 15839-15844.
- [184] Lakowicz, J. R. (2006). Principles of Fluorescence Spectroscopy. *Springer, New York, third ed.*
- [185] Calvin, M., Bassham, J. A. & Benson, A.A. (1950). Chemical transformations of carbon in photosynthesis. *Fed Proc*, 9 524-534.
- [186] Minagawa, J. & Takahashi, Y. (2013). Dynamic reorganization of photosynthetic supercomplexes during environmental acclimation of photosynthesis. *Front Plant Sci*, 4, 513

## VITA

Satarupa Bhaduri was born in the city of Kolkata in West Bengal, India. She received her B.S in Microbiology from St. Xavier's College, Kolkata in 2010 and M.S. in Biochemistry from the University of Calcutta, Kolkata, India. She joined the Department of Biological Sciences at Purdue University in August, 2013.

## PUBLICATIONS

- **Bhaduri, S.**; Zhang; H., Erramilli, S.; and Cramer, W.A. (2019) Structure-Function Studies of Cytochrome *b<sub>6</sub>f* Complex; Lipid Dependence. (submitted)
- Singh S.K.\*; **Bhaduri, S\***; Hasan, S.S.; Whitelegge, J.P. and Cramer, W.A (2019) Characterization of a Novel Chloroplast ATPase-Photosystem I Reaction Center Super-Complex (manuscript in preparation)
- **Bhaduri, S\***; Stadnytsky, V\*; Zakharov, S.D; Hasan, S. S.\*; Bujnowicz, L; Sarewicz, M; Osyczka, A and Cramer, W.A. (2017) Pathways of Transmembrane Electron Transfer in Cytochrome *bc* Complexes: Dielectric Heterogeneity and Interheme Coulombic Interactions. *The Journal of Physical Chemistry B*, 121, pp 975–983.

## CONFERENCES

### Oral Presentation:

- Interaction of Lipids with the Photosynthetic Membrane Lipoprotein: Cytochrome *b<sub>6</sub>f* Complex, *5<sup>th</sup> Midwest Membrane Trafficking and Signaling Symposium*, Purdue University, April 26<sup>th</sup>, 2019.
- Heterogeneity of the dielectric constant of the cytochrome *bc<sub>1</sub>* complex from *Rhodobacter capsulatus*, *41<sup>st</sup> Midwest / Southeast Photosynthesis Conference*, Turkey Run State Park, Indiana, Oct 23-25<sup>th</sup>, 2015.

### Poster Presentation:

- Characterization of a Novel ATPase-Photosystem I Reaction Center Complex in the Chloroplast Thylakoid Membrane. *62<sup>nd</sup> Annual Biophysical Society Meeting*, San Francisco, 17-21<sup>st</sup> February 2018.
- Characterization of a Novel Chloroplast ATPase-Photosystem I Reaction Center Super-Complex. *43<sup>rd</sup> Midwest/Southeast Photosynthesis Conference*, Turkey Run State Park, Indiana, Oct, 27-29, 2017.
- Determinants of the pathway of trans-membrane electron transfer in the bacterial cytochrome *bc<sub>1</sub>* complex: trans-membrane redox potential gradient and intra-protein dielectric heterogeneity *42<sup>nd</sup> Midwest/Southeast Photosynthesis Conference*, Turkey Run State Park, Indiana, Nov, 4-6<sup>th</sup>, 2016.

- Heterogeneity of the Hydrophobic Core of a Membrane Protein Complex, *60<sup>th</sup> Annual Biophysical Society Meeting*, Los Angeles Convention Center, Feb 21-25,2016.
- On the Lipid Dependence of the Stability of the Cytochrome *b<sub>6</sub>f* Complex, *The Hitchhiker's Guide to the Protein Galaxy*, Purdue University, May 13-14<sup>th</sup>, 2015.
- Lipid and Redox dependence of the Stability of the Hetero-Oligomeric Cytochrome *b<sub>6</sub>f* Complex”, *Membrane Proteins Structures Meeting*, Argonne National Laboratory, Illinois, 9-12<sup>th</sup> April,2015.

### AWARDS AND ACHIEVEMENTS

- Recipient of **Bilsland Dissertation Fellowship** offered by the Purdue College of Science for Fall, 2018.
- Recipient of the **Fall 2017 Travel Grant**, offered by Women in Science Program, College of Science, Purdue University.
- Recipient of the **Purdue Research Foundation fellowship** for the academic year 2017-18.
- Recipient of the **Best Oral Presentation Award** for the talk on “Heterogeneity of the dielectric constant of the cytochrome bc<sub>1</sub> complex from *Rhodobacter capsulatus*” at the *41<sup>st</sup> Midwest/Southeast Photosynthesis Conference*, Turkey Run State Park, Indiana, Oct 23-25<sup>th</sup>,2015.
- Recipient of the **IAS Summer Fellowship** given by the Indian Association of Science for May-July 2011.